Equivalent source methods for threedimensional acoustic imaging in complex environments

Joannès Chambon

N°d'ordre NNT : 2023ISAL0019

THÈSE de DOCTORAT DE L'INSA LYON, membre de l'Université de Lyon

École Doctorale N° 162
Mécanique, Énergétique, Génie civil, Acoustique

Spécialité/ discipline de doctorat :
Acoustique

Soutenue publiquement le 22/03/2023, par :
Joannès Chambon

Equivalent source methods for three-dimensional acoustic imaging in complex environments

---

Devant le jury composé de :

Valeau, Vincent	Professeur, Université de Poitiers	Président du jury
Snellen, Mirjam	Professeur, Delft University of Technology	Rapporteure
Thomas, Jean-Hugh	Professeur, Le Mans Université	Rapporteur
Chiariotti, Paolo	Professeur associé, Polytechnic of Milan	Examinateur
Antoni, Jérôme	Professeur, INSA Lyon	Directeur de thèse
Bouley, Simon	Docteur, MicrodB	Encadrant industriel

Printed on July 6, 2023.

Département FEDORA – INSA Lyon - Ecoles Doctorales

SIGLE	ECOLE DOCTORALE	NOM ET COORDONNEES DU RESPONSABLE
CHIMIE	**CHIMIE DE LYON** **https://www.edchimie-lyon.fr** Sec. : Renée EL MELHEM Bât. Blaise PASCAL, 3e étage secretariat@edchimie-lyon.fr	**M. Stéphane DANIELE** C2P2-CPE LYON-UMR 5265 Bâtiment F308, BP 2077 43 Boulevard du 11 novembre 1918 69616 Villeurbanne **directeur@edchimie-lyon.fr**
E.E.A.	**ÉLECTRONIQUE, ÉLECTROTECHNIQUE, AUTOMATIQUE** **https://edeea.universite-lyon.fr** Sec. : Stéphanie CAUVIN Bâtiment Direction INSA Lyon Tél : 04.72.43.71.70 secretariat.edeea@insa-lyon.fr	**M. Philippe DELACHARTRE** INSA LYON Laboratoire CREATIS Bâtiment Blaise Pascal, 7 avenue Jean Capelle 69621 Villeurbanne CEDEX Tél : 04.72.43.88.63 **philippe.delachartre@insa-lyon.fr**
E2M2	**ÉVOLUTION, ÉCOSYSTÈME, MICROBIOLOGIE, MODÉLISATION** **http://e2m2.universite-lyon.fr** Sec. : Bénédicte LANZA Bât. Atrium, UCB Lyon 1 Tél : 04.72.44.83.62 secretariat.e2m2@univ-lyon1.fr	**Mme Sandrine CHARLES** Université Claude Bernard Lyon 1 UFR Biosciences Bâtiment Mendel 43, boulevard du 11 Novembre 1918 69622 Villeurbanne CEDEX **sandrine.charles@univ-lyon1.fr**
EDISS	**INTERDISCIPLINAIRE SCIENCES-SANTÉ** **http://ediss.universite-lyon.fr** Sec. : Bénédicte LANZA Bât. Atrium, UCB Lyon 1 Tél : 04.72.44.83.62 secretariat.ediss@univ-lyon1.fr	**Mme Sylvie RICARD-BLUM** Institut de Chimie et Biochimie Moléculaires et Supramoléculaires (ICBMS) - UMR 5246 CNRS - Université Lyon 1 Bâtiment Raulin - 2ème étage Nord 43 Boulevard du 11 novembre 1918 69622 Villeurbanne Cedex Tél : +33(0)4 72 44 82 32 **sylvie.ricard-blum@univ-lyon1.fr**
INFOMATHS	**INFORMATIQUE ET MATHÉMATIQUES** **http://edinfomaths.universite-lyon.fr** Sec. : Renée EL MELHEM Bât. Blaise PASCAL, 3e étage Tél : 04.72.43.80.46 infomaths@univ-lyon1.fr	**M. Hamamache KHEDDOUCI** Université Claude Bernard Lyon 1 Bât. Nautibus 43, Boulevard du 11 novembre 1918 69 622 Villeurbanne Cedex France Tél : 04.72.44.83.69 **hamamache.kheddouci@univ-lyon1.fr**
Matériaux	**MATÉRIAUX DE LYON** **http://ed34.universite-lyon.fr** Sec. : Yann DE ORDENANA Tél : 04.72.18.62.44 yann.de-ordenana@ec-lyon.fr	**M. Stéphane BENAYOUN** Ecole Centrale de Lyon Laboratoire LTDS 36 avenue Guy de Collongue 69134 Ecully CEDEX Tél : 04.72.18.64.37 **stephane.benayoun@ec-lyon.fr**
MEGA	**MÉCANIQUE, ÉNERGÉTIQUE, GÉNIE CIVIL, ACOUSTIQUE** **http://edmega.universite-lyon.fr** Sec. : Stéphanie CAUVIN Tél : 04.72.43.71.70 Bâtiment Direction INSA Lyon mega@insa-lyon.fr	**M. Jocelyn BONJOUR** INSA Lyon Laboratoire CETHIL Bâtiment Sadi-Carnot 9, rue de la Physique 69621 Villeurbanne CEDEX **jocelyn.bonjour@insa-lyon.fr**
ScSo	**ScSo*** **https://edsciencessociales.universite-lyon.fr** Sec. : Mélina FAVETON INSA : J.Y. TOUSSAINT Tél : 04.78.69.77.79 melina.faveton@univ-lyon2.fr	**M. Bruno MILLY** Université Lumière Lyon 2 86 Rue Pasteur 69365 Lyon CEDEX 07 **bruno.milly@univ-lyon2.fr**

*ScSo : Histoire, Géographie, Aménagement, Urbanisme, Archéologie, Science politique, Sociologie, Anthropologie

REMERCIEMENTS

Ce manuscrit cristallise trois années de travail sur les sources équivalentes , soit 1096 jours environ entre 2020 et 2023 tous plus ou moins riches en rebondissements. Si mon nom y fait figure de signature, il est important pour moi de mentionner la multitude de ses contributrices et contributeurs. Je profite donc des lignes qui suivent pour les remercier.

Pour commencer, merci à Mirjam Snellen et Jean-Hugh Thomas d'avoir d'avoir questionné et étayé la teneur scientifique de ce rapport à travers leur rôle de rapporteur. Je remercie également Vincent Valeau et Paolo Chiarioti d'avoir accepté de prendre part à mon jury, apportant avec eux leur expertise en imagerie acoustique à l'évaluation de mes travaux.

Je souhaiterais ensuite remercier mon directeur, Jérôme Antoni, pour ses conseils tant sur le fond que sur la forme, si particulière et propre au monde de la publication scientifique. Maintenir le navire thèse à flot au gré des confinements succesifs n'aura pas été une mince affaire, mais il semblerait que j'y sois parvenu et ses indications sur les subtilités des sources équivalentes auront été de précieuses orientations pour garder le cap.

Il me tient à cœur de remercier maintenant toutes les parties prenantes de mon environnement de travail à MicrodB à commencer par mes encadrants Simon et Thibaut; en tandem depuis leurs TP à l'ENSIM jusqu'à l'encadrement de doctorants. Parmi bien d'autres choses, je leur dois notamment une formation de haute volée à la recherche en acoustique ainsi que de fondamentales découvertes musicales de *Peach Pit* à *Son Lux* (et ce malgré l'irréconciliable antagonisme de leurs goûts musicaux).

Un grand merci à Olivier pour son soutien, toute l'expérience transmise et tout le temps qu'il continue de consacrer à plancher avec moi sur la métaphysique des fonctions de transfert; merci à Sébastien pour ses avis toujours éclairants; merci à Lucille pour sa confiance; merci à Bruno, Fabien, Loïc (longue vie à la patine de l'analogique), Virgile, Gérald et Katja qui jouent pour beaucoup dans l'ambiance inestimable de MicrodB. Merci bien sûr aux anciens combattants Thibaud & Allan (qui je l'espère reviendront un jour pour la création d'une section CNT à Vibratec), à Christophe pour son infatiguable allant scientifique, et à Valentin pour avoir partagé avec moi son expérience de doctorant CIFRE. Merci enfin aux nouveaux arrivants Sagar, Enzo, Mathis, Marion, Antoine, Julie, Anthony et Lucas qui renouvellent brillament MicrodB par leurs qualités et leurs participations aux commandes Thomann.

Merci bien sûr à tous les collègues de Vibratec, et en particulier à Christine et Muriel pour les débats de la pause déjeuner.

Je remercie également tous les membres du LVA pendant que j'ai pu rencontrer au cours de ces trois années. Parvenir à participer aussi activement à la vie du laboratoire qu'à celle de l'entreprise n'a rien d'évident en CIFRE, mais je conseilleirai sans hésitation le LVA à tout aspirant thésard tant l'équipe des doctorants/post-doc y est soudée et vivante.

Il me faut également faire la part belle à tous mes compagnons de cordées pour leur participation inconsciente au bon déroulement de cette thèse. Merci donc à Sohrenn, Paul Mo, Romain, Matthias, Raph, Esther, Baptiste et Manon pour leur soutien aussi bien aux pieds des voies que pendant les heures sombres de la Jojo-mobile. Merci bien sûr à Marine, Geoffrey et Mathilde pour toutes les escapades salutaires loin des mes codes Pythons, que ça soit en rando, falaise, grande voie ou joëlette, ainsi qu'à tous les camarades de jeu croisés sur les tapis d'Hold Up. Ils sont trop nombreux pour être tous cités ici, bien que ça ne soit pas l'envie qui manque.

Évidemment merci à mes parents et mes deux frères pour leur soutien inconditionnel au cours de ces trois années, ainsi qu'à ma grand-mère qui je l'espère sera fière de ces travaux malgré l'opacité du sujet combinée à mes piètres qualités de vulgarisateur.

Merci enfin à Juliette, je sais que comme moi elle n'apprécie pas tellement de se retrouver au centre de l'attention mais c'est bien à elle et son soutien de tous les jours que je dois le plus, tant pour cette thèse que pour tout le chemin parcouru ensemble depuis un bout de caillou planté sur les contreforts du Puy de Sancy.

Abstract

With the growing interest for acoustic source identification in three dimensions, a set of new issues with respect to two-dimensional acoustic imaging with microphone arrays are to be tackled. One is the model chosen to describe the acoustic propagation in the environment where the measurements are performed. This may feature first order phenomena such as scattering effects, convection or inherent directivity patterns related to the physical origin of the sources. In practical, this model takes the form of a transfer function between sources and microphones, discretized into a matrix then featured to an inversion algorithm. In this thesis, the equivalent source method is surveyed as a simple and flexible simulation tool to build physically accurate transfer functions able to account for the above-cited phenomena. In-depth approaches to tune equivalent sources for acoustic imaging purposes are proposed and assessed with respect to various test cases including both analytical models, actual wind tunnel measurements and simulations. Finally, a more prospective algorithm is designed with a view to fully involve equivalent sources in the imaging process and bypass formalism of transfer functions computed independently from measurements: equivalent sources are tailored to concomitantly match with microphone pressures and a given boundary condition, then propagated toward regions of interest to seize the directivity of the emitted sound field. Performance of this method is benchmarked side by side with wide-spread acoustic imaging algorithms on a mock-up fitted with flush-mounted sources.

Résumé

L'identification de sources en trois dimensions par antennerie relève de problématiques nouvelles en imagerie acoustique. L'une d'entre elle concerne le modèle retenu pour retranscrire la propagation acoustique dans l'environnement de mesure. Ce dernier doit potentiellement être en mesure de prendre en compte des phénomènes de premier ordre : diffraction, convection ou directivités liées à la nature physique de sources. En pratique, le choix du modèle de propagation se résume à la construction d'une matrice de transfert entre une grille de sources potentielles et une antenne de microphone qu'il convient d'inverser pour revenir aux sources prépondérantes. Dans cette thèse, la méthode des sources équivalentes est testée en tant qu'outil simple et modulable pour la simulation de fonctions de transfert permettant une description plus précise de la scène acoustique. Des méthodes détaillées de paramétrage des sources équivalentes sont proposées et évaluées sur divers cas d'étude obtenus analytiquement, par mesure en soufflerie ou simulation dynamique des fluides. Pour finir, une approche plus prospective est mise au point dans l'objectif d'inclure les sources équivalentes dans le processus d'antennerie de manière plus cohérente que lors du calcul direct de matrices de transfert. Les sources sont ajustées en fonction des pressions microphoniques et d'une condition aux limites, puis repropagées pour représenter l'ensemble du champ rayonné. L'intérêt de cet algorithme est évalué comparativement à des techniques d'imagerie classique sur des mesures de sources corrélées montées sur une maquette de moteur.

RÉSUMÉ ÉTENDU EN FRANÇAIS

Introduction

L'extension des méthodes actuelles d'identification de sources acoustiques à des grilles de calcul en trois dimensions constitue l'un des principaux axes de progression en antennerie acoustique, tant dans les études académiques qu'industrielles. Financée conjointement par l'Agence Nationale de le Recherche et de la Technologie et l'entreprise MicrodB, cette thèse relève de ce domaine de recherche et s'inscrit dans une continuité de travaux visant à fournir des cartographies de sources acoustiques en trois dimensions de plus en plus précises sur la base de mesures microphoniques.

Des enjeux propres à l'imagerie acoustique en trois dimensions sont mis en évidence dans la littérature. En premier lieu, il convient de rappeler qu'en pratique les mesures sont généralement effectuées au moyen d'antennes planes qui ne recouvrent que rarement le support des sources acoustiques. Ainsi, les phénomènes de masquage et de diffraction sont significatifs à haute fréquence et peuvent amener à des erreurs de localisation, et le passage vers des géométries d'antenne plus adaptées est rarement envisagé étant donnée le coût des voies de mesure.

S'ajoutent à ceci des facteurs d'environnement liés à la scène acoustique. Dans le contexte de mesures en soufflerie automobile, la réflexion des ondes acoustiques sur le sol ainsi que leur réfraction par la couche de cisaillement entre la zone d'écoulement et le milieu au repos sont deux autres facteurs déterminants pour une détection précise des sources. Là encore, il s'agit de caractéristiques propres aux trajets acoustiques entre les grilles de calcul et les antennes à prendre en compte dans le processus d'imagerie.

Enfin, dans l'objectif d'identifier des sources résultant de l'interaction d'un écoulement avec un objet rigide, il est également important d'intégrer la potentielle directivité des sources à la lumière des analogies aéroacoustiques et de leur interprétation physique.

Sur la base de ces observations, le principal angle d'attaque retenue pour cette thèse porte sur l'amélioration des modèles de propagation acoustique utilisés pour retranscrire le rayonnement des sources vers des positions de microphones

prédéfinies. La méthode des sources équivalentes (ESM, pour *Equivalent Sources Method*) est évaluée dans cette optique, pour des raisons évoquées ci-après.

Objectifs de la thèse

Les enjeux de la thèse portent globalement sur l'évaluation des approches de sources équivalentes pour l'amélioration des performances d'antennerie en environnements réalistes. Étant donnée la pluralité des facteurs rentrant en ligne de compte, les questions du design d'antenne en trois dimensions et du développement de nouveaux algorithmes de méthodes inverses sont écartées afin d'axer la thèse sur les modèles de transfert. Les objectifs en terme de validation sont orientés par les besoins industriels de MicrodB et concernent principalement le domaine de l'automobile, et en particulier la détection de sources en soufflerie. Pour ces mêmes raisons, les applications envisagées sont volontairement restreintes au cas de sources stationnaires.

Plan du manuscrit

Cette thèse est organisée en quatre chapitres selon le cheminement suivant : Le premier chapitre constitue une revue bibliographique où est établit le problème inverse d'imagerie acoustique, comportant une description approfondie des différentes approches de détermination de fonctions de transfert (FRF, pour *Frequency Response Function*) en trois dimensions. Le chapitre 2 s'attarde sur la description de la méthode ESM dans ce contexte et propose pour le cas sphérique des résultats d'études paramétriques. En découle la mise au point d'une nouvelle méthode de Galerkin ESM repartant de la version historique de l'ESM pour l'adapter à la synthèse de champs à partir de mesures microphoniques. Vient enfin le dernier chapitre dédié à l'évaluation de toutes les méthodes à l'étude sur des cas de validation provenant d'affaires ou de projets de recherche industriels.

Chapitre 1 : État de l'art des modèles de propagation pour l'imagerie acoustique en trois dimensions

Ce chapitre pose le cadre du problème d'identification de sources par mesure d'antennerie en trois dimensions, en mettant l'emphase sur les modèles de propagation. En premier lieu, un bref état de l'art des méthodes inverses est établi, per-

mettant d'introduire la technique de *beamforming* et ses déclinaisons ainsi que la focalisation bayésienne itérative. Ces approches seront ensuites utilisées pour les études comparatives des fonctions de transfert calculées par les méthodes ESM. Il ressort de cette première étape de la revue bibliographique que les algorithmes d'imagerie disponibles dans la littérature couvrent déjà un large panel de configurations, allant des sources parcimonieuses décorrélées identifiables par déconvolution à des sources plus étendues reconstruites par méthode inverse.

On s'intéresse dans un second temps à la possibilité de prendre en compte les modifications de la propagation acoustique entre la grille des sources potentielles et l'antenne dues à la scène acoustique. L'hypothèse la plus répandue dans la littérature est de simplifier ces aspects et de considérer par défaut des sources monopolaires se propageant en champ libre, conduisant dans certains cas à des erreurs significatives. La considération analytique de la diffraction et du masquage par des géométries simples a fait l'objet de plusieurs publications. Étant largement utilisé, le cas d'un monopole diffracté par une sphère rigide est explicité dans ce chapitre et permet de mettre en évidence l'intérêt de prendre en compte ce phénomène. Pour des conditions aux limites plus complexes sur des géométries réalistes, les seules options possibles sont la mesure expérimentale des FRFs souvent laborieuse en pratique ou leur simulation numérique. Les références citées pour cette dernière option sont les méthodes d'éléments frontières, mais leur implémentation relève d'une certaine complexité et les temps de calculs associés sont importants.

En ayant à l'esprit des applications en soufflerie à faible nombre de Mach, se pose également la question de la directivité des sources recherchées. Au regard des analogies aéroacoustiques, il est important de pouvoir intégrer le caractère dipolaire des sources dites *de chargement* résultant de la force de réaction d'une surface rigide immergées dans un écoulement.

Dès lors, la méthode des sources équivalentes apparaît comme une alternative pertinentes pour le calcul rapide et flexible de FRF pour l'imagerie acoustique.

Chapitre 2 : Sources équivalentes pour la simulation de fonctions de transfert

Ce chapitre débute par une nuance apportée à la littérature quant à la terminologie ESM. L'objectif est de faire clairement la distinction entre d'une part la version historique de l'ESM en tant que méthode de simulation permettant la

prise en compte d'une condition aux limites donnée, et d'autre part un pan entier d'algorithmes d'imagerie acoustique faisant intervenir des monopoles dont les amplitudes et phases sont déterminées par méthode inverse pour correspondre à une mesure d'antennerie (sans condition aux limites particulière).

L'ESM est ensuite introduite sur la base de sa formulation historique dans l'article de Koopmann *et al.* (1989). Considérant la modélisation numérique d'une surface diffractante fermée par un maillage, l'ESM permet de simuler le champ acoustique au voisinage de cette dernière par le biais d'un ensemble de monopoles placés à l'intérieur de la surface et calibrés pour satisfaire la condition aux limites sur le maillage. Après une explication du formalisme de l'ESM, le processus appliqué au calcul de FRF est rendu possible grâce au principe de réciprocité qui permet d'échanger les rôles des sources et de l'antenne. Ainsi, l'idée générale est de considérer une source unitaire sur chaque position de microphone, d'en déduire un champ de vitesse incident sur le maillage avant de compenser ce dernier par le champ rayonné par le nuage de sources équivalentes. Cette approche est validée analytiquement par comparaison avec le modèle sphérique exacte présenté au chapitre précédent.

Par la suite, une recherche du paramétrage optimal du nombre et des positions des sources équivalentes est conduite, sur la base de critères de conditionnement numérique. Des ajouts modulaires de l'ESM sont enfin discutés, permettant la prise en compte de sources incidentes dipolaires, de la réflexion par le sol ainsi que d'un modèle simple de réfraction par une couche de cisaillement dans la FRF utilisée pour l'imagerie.

Au final, le calcul de FRFs pour l'imagerie en trois dimensions sur une géométrie arbitraire est rendue possible par la méthode ESM et permet l'inclusion de facteurs d'environnement de premier ordre dans le modèle de transfert.

Chapitre 3 : Inclusion des sources équivalentes dans le problème inverse par la méthode Galerkin ESM

À ce stade, le calcul des FRFs est effectué en amont et indépendamment des mesures. Une méthode ESM plus prospective est mise au point dans ce chapitre, avec pour idée directrice d'inclure directement les sources équivalentes dans le problème inverse d'imagerie acoustique sans pour autant mettre de côté leur rôle pour la condition aux limites. Le concept de cette nouvelle approche consiste en la résolution d'un système linéaire reliant les pressions mesurées aux sources équiv-

alentes, en ayant pris soin au préalable de projeter les solutions potentielles sur un sous-espace vectoriel où la condition aux limites de diffraction est nécessairement respectée.

La matrice de projection associée est calculée à partir de la décomposition QR de la matrice de propagation des sources équivalentes vers le maillage de l'objet diffractant. Il est ensuite possible d'agencer ce projecteur de manière à maximiser la puissance acoustique rayonnée par les sources équivalentes, une telle opération permettant de ne considérer que les distributions de sources les plus efficaces selon le critère de rayonnement et donc de réduire la dimension du problème inverse finale.

Appelée Galerkin ESM (GESM, en référence aux méthodes de Galerkin des éléments finis qui font également intervenir un projecteur orthogonale sur un sous-espace lié à une condition aux limites), cette méthode est finalement comparées aux approches de formation de voie et de focalisation bayésienne sur le cas de la sphère rigide. Cette étape montre que la GESM est efficace pour le calcul de sources corrélées ou non, diffractées par la sphère, et largement préférable aux FRFs de simple champ libre.

Chapitre 4 : Validation et applications sur cas industriels

Le quatrième et dernier chapitre conclut la thèse par l'évaluation des méthodes ESM mises en exergue dans les deux précédents chapitres sur trois cas industriels distincts.

On s'intéresse tout d'abord à la localisation expérimentale d'une source omnidirectionnelle placée sur le rétroviseur gauche d'une voiture en soufflerie, au moyen de trois antennes planes (360 microphones au global). Ce premier cas test a pour avantage d'avoir une position et une directivité de source connues, il permet donc de tester la prise en compte des effets de vent, de sol et de diffraction indépendamment de tous les autres facteurs de performances. Il ressort de cette étude que les FRFs ESM monopolaires utilisées avec le *beamforming* standard en trois dimensions permettent des gains substantiels en résolution sur les cartographies de sources.

On s'intéresse ensuite à la caractérisation d'une distribution de sources d'origine purement aéroacoustique avec un modèle de rétroviseur simplifié placé au sein d'un écoulement. Les signaux temporels sur une antenne sphérique de 400 mi-

crophones virtuels recouvrant intégralement le rétroviseur sont cette fois-ci issus d'une simulation CFD. Les objectifs de ce deuxième cas d'étude sont très différents : la propagation acoustique ne subit cette fois aucune modification liée aux conditions de mesure mais ni la nature exacte des sources ni leur distribution spatiale ne sont connues en amont. Il est donc possible d'évaluer conjointement les quatre modèles de sources disponibles à l'issue du second chapitre : monopoles ou dipoles, se propageant en champ libre ou en prenant en compte la géométrie du rétroviseur. L'analyse des résultats d'imagerie permet de conclure que les approches monopolaires et dipolaires amènent à des interprétations complémentaires des sources identifiées : les monopoles identifiés donnent une bonne vision d'ensemble de la pression de surface sur l'objet, là où les dipoles sont plus à même de mettre en évidence les aspérités géométriques à l'origine de bruit. Comme pour le cas précédent, l'apport de l'ESM est significatif pour les monopoles mais plus nuancé pour l'identification des sources dipolaires. Cette distinction est probablement due au fait que la directivité intrinsèque des dipoles même en champ libre est déjà relativement efficace pour l'effet de masquage.

Un dernier cas plus orienté vers les applications banc moteur est exhibé en dernière instance pour tester la méthode GESM. Issue du projet ECOBEX, le champ de pression rayonné par trois sources partiellement corrélées montées sur une maquette de moteur est mesuré par une antenne plane de 36 voies de mesure analogiques. Le champ repropagé est ainsi obtenu par Galerkin ESM sur une surface d'observation pour différentes fréquences, et l'on constate qu'il s'agit de la méthode la plus performante pour la synthèse réaliste du champ de pression.

Conclusion

À travers ce travail de thèse, différentes approches de sources équivalentes sont mises à profit pour le perfectionnement de l'identification de sources en trois dimensions. Pour le calcul des FRFs, l'ESM se trouve être une option robuste et relativement simple à implémenter permettant l'inclusion modulaire d'un certain nombre de corrections d'environnement. Le formalisme des fonctions de transfert étant relativement peu adapté à la reconstruction du champ acoustique, la méthode GESM constitue une évolution logique de l'ESM standard dans ce sens et permet une observation réaliste de champs rayonnés tout en contournant l'étape de simulation des FRFs.

Perspectives

De nombreuses pistes peuvent être envisagées pour faire suite à ce travail de thèse.

Il serait par exemple intéressant de mettre en place une description mathématique des sources équivalentes en tant que base de représentation, notamment dans le but de dégager des consigne de paramétrage moins dépendantes de la géométrie à l'étude. Pour ce faire, le formalisme des bases de Riesz semble pouvoir fournir des indicateurs pertinents pour juger de la qualité intrinsèque d'une distribution de sources équivalentes.

De plus, une accélération algorithmique de l'ESM et de la GESM pourrait très certainement être obtenue en couplant ces méthodes avec la méthode multipolaire rapide de Coifman *et al.* (1993). Il s'agirait de grouper les sources équivalentes proches par rapport à la longueur d'onde et qui peuvent donc être considérées confondues. Les potentiel gain serait alors une optimisation des produits matrices vecteurs pour accélérer l'étape de SVD et de décomposition QR, en améliorant au passage les éventuels problèmes de conditionnement à basses fréquences.

Pour finir, l'étude du rétroviseur simplifié dans le dernier chapitre laisse penser que la mise en place d'un modèle de propagation répartissant l'énergie captée par les microphones sur des ensembles de sources monopolaires et dipolaires serait pertinent pour l'imagerie aéroacoustique. La discrimination claire des bruits d'épaisseur et de chargement à partir de mesures d'antennerie serait une avancée conséquente dans ce domaine.

CONTENTS

Remerciements **v**

Abstract **viii**

Résumé étendu en français **x**

Nomenclature **xx**

Introduction **1**

1 Literature survey of acoustic models for 3D imaging **5**

1.1 Statement of the inverse problem 5

1.1.1 Physical hypotheses 6

1.1.2 Algebraic formulation 6

1.2 Practical inversion 10

1.2.1 Beamforming 10

1.2.2 Inverse methods 13

1.2.2.1 Bayesian framework 14

1.3 State of the art on acoustic transfer functions 16

1.3.1 Elementary sources 16

1.3.2 Spherical transfer model 20

1.3.3 FRF construction for 3D arbitrarily shaped geometries 22

1.3.3.1 Measured transfer functions 22

1.3.3.2 Simulated transfer function 23

1.4 Aeroacoustic models for wind tunnel applications 25

1.4.1 Aeroacoustic analogies 25

1.4.2 CFD and acoustic imaging 28
1.5 Conclusion 30

2 Equivalent sources for transfer function simulation 31
2.1 The use of ESM terminology for acoustic imaging 31
2.2 ESM process 33
2.2.1 Principle and theoretical statement 33
2.2.1.1 Implementation 34
2.2.1.2 ESM in the Boundary Element Method framework . . 36
2.2.2 Validation for FRF simulation 38
2.2.2.1 Reciprocity principle 38
2.2.2.2 SRTF comparison 39
2.2.3 Parametric study 40
2.2.3.1 Positions of the equivalent sources 41
2.2.3.2 Number of the equivalent sources 45
2.3 Dipolar ESM 45
2.3.1 ESM steps update 46
2.3.2 SVD truncation with Picard plots 47
2.4 Refinements for wind tunnel applications 48
2.4.1 Ground effects 48
2.4.2 Shear layer refraction 49
2.5 Conclusion 50

3 Equivalent sources and inverse problem unification: Galerkin ESM 53
3.1 Motivations 53
3.2 Galerkin ESM 55
3.2.1 Overall methodology 55
3.2.2 Null space of the boundary condition matrix 57
3.2.3 Practical inversion 58
3.3 Kernel layout through principal surfaces 59
3.4 Numerical Validation 61
3.4.1 Presentation of the benchmark protocol 63
3.4.2 Monopolar sources on sphere 65
3.4.2.1 Uncorrelated monopoles 65
3.4.2.2 Correlated monopolar sources 67
3.4.3 Principal Surfaces 71
3.4.4 Computational efficiency 73

3.5 Conclusion 74

4 Industrial validation & results **77**

4.1 Car mirror in a wind tunnel 77

4.1.1 ESM parametrization for industrial testing 79

4.1.2 Imaging outputs 81

4.1.2.1 Q-source identification from no wind measurements . 82

4.1.2.2 Q-source identification from Mach 0.11 measurements 84

4.2 Source identification from CFD data 86

4.2.1 Idealised Side Mirror 87

4.2.1.1 CFD data overview 88

4.2.1.2 Imaging results 91

4.3 Ecobex test bench 96

4.3.1 Source identification 98

4.3.2 Directivity reconstruction 101

4.4 Conclusion 104

Conclusion **107**

Proceedings and Publications **111**

Appendix A - Design of a source generation routine **112**

References **117**

List of figures **126**

NOMENCLATURE

Variables

a	Sphere radius for SRTF	N	Number of grid points
$\boldsymbol{B}$	$(N_s \times K)$ GESM projection matrix	$\boldsymbol{n}$	Normal vector at a grid point
c_0	Sound speed in the air	N_s	Number of equivalent sources
$\boldsymbol{c}$	$(M \times 1)$ Measurement noise	η	$\frac{N_s}{N}$ ratio
D	Free-field dipole function	Ω	Radiating body volume
$\boldsymbol{d}$	$(K \times 1)$ GESM sources	$\boldsymbol{p}$	$(M \times 1)$ measured pressures
f	Frequency	$\boldsymbol{q}$	$(N \times 1)$ grid source distribution
f_s	Sampling frequency	$\tilde{\boldsymbol{q}}$	$(N_s \times 1)$ equivalent sources distribution
G	Free-field Green function	$\boldsymbol{r}$	(3×1) positions
$\boldsymbol{G}$	Volume flow to pressure propagation matrices	ρ	Air density
Γ	Radiating body skin	$\boldsymbol{S}_{pp}$	$(M \times M)$ array CSM
$\boldsymbol{H}$	$(M \times N)$ transfer matrix	$\boldsymbol{S}_{qq}$	$(N \times N)$ grid sources CSM
$h_n(\cdot)$	Spherical Hankel Function of order n	σ	Singular values
k	Acoustic wave number	$\boldsymbol{T}$	Volume flow to normal velocities propagation matrices
κ	Conditioning number	$\boldsymbol{v}_n$	$(N \times 1)$ normal velocity on the grid
M	Number of microphones	ξ_d	Equivalent sources retreat distance
$\boldsymbol{M}_0$	Mach number	$\boldsymbol{Z}$	Impedance matrices

Indices

$\cdot_i$	i^{th} microphone	$\cdot_l$	l^{th} equivalent source
$\cdot_j$	j^{th} grid point		

Operators

$\mathbb{E}[X]$	Expected value	$\mathrm{Tr}(\boldsymbol{X})$	Matrix trace
$\mathrm{Im}\boldsymbol{X}$	Matrix image	$\|\boldsymbol{x}\|$	L^2 norm (Frobenius for matrices)
$\ker\boldsymbol{X}$	Matrix kernel	$\|\boldsymbol{x}\|_p$	L^p norm
$\mathrm{Rg}(\boldsymbol{X})$	Matrix rank	$\boldsymbol{x}\cdot\boldsymbol{y}$	Scalar product

Acronyms

CBF	Conventional Beamforming
CFD	Computational Fluid Dynamics
CSM	Cross Spectral Matrix
(G)ESM	(Galerkin) Equivalent Sources Method
F/BEM	Finite/Boundary Element Method
FRF	Frequency Response Function
FW-H	Ffowcs Williams & Hawkings
ISM	Idealised Side Mirror
(i)BF	(iterative) Bayesian Focusing
MBF	Multiplicative Beamforming
PSF	Point Spread Function
SRTF	Sphere Related Transfer Function
SVD	Singular Value Decomposition

Conventions

Arrays and matrices are indicated in bold type.

The $\boldsymbol{M}^{\mathsf{H}}$ superscript denotes the Hermitian conjugate of a matrix, while a $\boldsymbol{M}^{\top}$ superscript refers the conventional transposition in $\mathbb{R}$. As for vector, the $\boldsymbol{M}^{*}$ superscript denotes the conjugate transpose. The $\boldsymbol{M}^{+}$ superscript indicates the Penrose (1955) pseudo-inverse.

The convention for phase sign in this report is $e^{+\mathrm{i}kr-\mathrm{i}\omega t}$. Every pressure level in decibel is given with a reference pressure $p_{\mathrm{ref}} = 2 \times 10^{-5}$ Pa. Every acoustic power in decibel is given with a reference power $W_{\mathrm{ref}} = 10^{-12}$ W.

The notion of *dynamic range* used in all the acoustic maps displayed in this document is defined as a threshold under which sources or pressure levels are removed of the plot for the sake of clarity.

INTRODUCTION

Overall context

In the context of an ever growing demand for noise control at the design step of industrial processes, acoustic imaging based on phased microphone arrays emerged as one of the most prized solution. For both aeroacoustic and vibroacoustic monitoring, the concept of crossing the information measured by wisely placed microphones before a repropagation on the radiating structure proved out to combine accurate performances and technological practicability. Prior developments in microphone array processing techniques exhibited robust and strongly assessed algorithms for acoustic source characterization on two-dimensional plane regularly discretized. Based on this, a current research lead lies in the extension of these approaches to three-dimensional source identification. As a company specialized in the conception and operation of microphone arrays for industrial purposes, MicrodB is willing to keep up with the state-of-the-art tools in this field and use them for noise control in the automotive and aeronautic sectors where standards are becoming more stringent. The proposed thesis work is thus motivated by the continual improvement pursued at MicrodB in terms of three-dimensional acoustic imaging. The company funded this PhD thesis, with the support of the *"Association Nationale de la Recherche et de la Technologie (ANRT)"*.

The identification of acoustic sources on a three dimension support has propelled to the forefront in investigations, and with it emerged new stakes already well studied in the literature. In the automotive industry, mastering the acoustic field produced by an operating engine often relies on acoustic imaging through near-field array measurements. Given the complex geometries of engines, conclusions drawn on the basis of acoustic imaging maps are likely to be flawed because of the masking effects and the diffraction operated by all the mechanical components. Solutions to avoid it mainly consist in setting multiple arrays to fully cover the mesh, but such a strategy significantly increases the hardware costs and the practical difficulties of the measurement sessions.

Research campaigns conducted in wind tunnel is a field where three-dimensional imaging is expected to refine the analysis of aeroacoustic profiling. Here again, prior research substantiates the shortfall of keeping up with the simplifying assumptions commonly made for two dimension measurements. Wind-tunnel are usually equipped with two or three large planar arrays on the top and the side of the room. The latter were not specifically shaped for source localization along their normal axis and thus suffer from poor normal resolutions when using classical imaging techniques. When it comes to sound generation mechanism, the academic community thoroughly investigated the best source models to describe the acoustic radiation resulting from a flow impinging an object and how it could be related to specific directivities. This point has to be addressed for proper source localization as the relevancy of a microphone may be pondered by its relative position regarding the sources.

Several lines of attack can be considered to solution the aforementioned issues. This thesis work focuses on the enhancement of the numerical models accounting for the transfer between sources and arrays, considering that the currently used free-field ones may be overly simplified in many practical cases. To this end, a well established approach named the Equivalent Source Method (ESM) was adopted as an promising tool at the origin of this PhD.

Main objectives

In order to frame the thesis subject, only enhancements of transfer models are sought independently from questions related to the array geometry or the inverse algorithm. In addition to that, the emphasis is put on acoustic imaging in the frequency domain considering stationary data. Given these working assumptions, the goals of this thesis are twofold : the first one is to conduct an in-depth analysis of equivalent sources techniques and derive them to properly fit with the acoustic imaging frameworks. The second is to take stock of the benefits and limits arising from the upgrade of acoustic transfer models based on equivalent sources.

Bearing in mind the industrial needs of MicrodB, most of the investigations are carried out for applications in the car industry since the automotive wind tunnels account for a significant part of the company activity. However, the proposed developments strive to remain generic enough to be extended to other cases.

Contributions

The primary scientific outputs of the work exposed in the thesis are listed in the present section:

- New insights concerning the parametrization of the ESM are suggested. Indicators on the quality of its output are designed for large-size industrial models and tested. This point represents a straight continuation of previous researches on the optimal process to handle equivalent sources, mostly made of empirical statements.
- The benefits stemming from the use of realistic transfer functions integrating the acoustic scene perturbations is underlined through a diversified panel of test cases. All the efforts put on the simulation of more accurate transfer models yield to more reliable source maps with greater resolution and accuracy. It notably mitigates side-lobes when using beamforming, and drastically changes the interpretations of imaging maps at high frequencies when scattering effects are significant.
- The draft of a novel inverse method for sound field reconstruction is conceived, with a view to align concepts sampled from both equivalent sources techniques and acoustic imaging: a cloud of equivalent sources is considered as the unknown of an inverse problem governed by the microphone pressures, and constrained by physical hypothesis from the acoustic scene such as boundary conditions on a diffracting body.

Organization of the document

The report is structured with four chapters. Chapter 1 surveys the formalism of the acoustic imaging inverse problem in three dimensions, starting with general considerations on all its components then bearing down on the specific role played by the transfer functions. It aims at covering the options discussed in prior researches to simulate acoustic transfers between grid sources and microphone arrays. The subsidiary function of this first part is also to lay the groundwork for the validation steps of the thesis in terms of imaging algorithms.

It arises from the literature review that the ESM is worth being assessed as an algorithm to simulate transfer functions a microphone and a surface assumed perfectly rigid. This is the point adressed in Chapter 2, where the method is outlined from both the theoretical and practical views and refined regarding issues

commonly faced when performing acoustic imaging. This includes discussions on the reciprocity principle, validation with analytical models and numerical investigations on the effective configurations of the sources.

Once the primary use of ESM properly explored, a declension of it thought for array imaging is elaborated in Chapter 3. By means of a preconditioned matrix inversion and a repropagation of the equivalent sources, the new approach named Galerkin ESM aims at the direct synthesis of the pressure field around a diffracting body by making the most of an array measurement. This method is compared with two other well established imaging algorithms at the end of this second to last chapter.

Finally in Chapter 4, industrial usages of both standard ESM and Galerkin ESM are proposed. A punctual source carried by the rear view mirror of a car in a wind tunnel serves as the first test case to check the relevancy of simulating the acoustic propagation of an omnidirectional source scattered by a side-mirror instead of keeping up with straightforward free-field monopole models. Then the focus switches to the CFD simulation of an idealised side mirror, mainly to appraise the nuance brought by dipolar ESM transfer functions for purely aeroacoustic sound sources. The chapter and the thesis then ends with a more engine bench -oriented data from the former MicrodB ECOBEX project to probe the assets of Galerkin ESM for sound field reconstruction.

CHAPTER 1

LITERATURE SURVEY OF ACOUSTIC MODELS FOR 3D IMAGING

Multi-channel microphone acquisition constitutes a common ground for a wide range of source identification processes. The latter feature an extended literature of signal processing techniques and inverse methods to get most information of the measurements. With the recent emphasis put on three-dimensional imaging also emerged new issues related to environment and scattering effects. The following chapter surveys the state-of-the-art methods used in three-dimensional source identification, with a specific focus on refined source models.

1.1 Statement of the inverse problem

When it comes to source identification, a generic set-up can be defined from which an extensive collection of methods and algorithms were derived in the literature. Section 1.1 outlines this framework, from the starting physical hypothesis to the mathematical statement of the acoustic imaging inverse problem at the heart of this thesis work.

1.1.1 Physical hypotheses

The scope of this document is doubly restricted in terms of acoustic quantities. First, small deviations of pressures and densities with respect to their mean values are assumed and the linear version of acoustic equations governs the physical model.

In addition to that, pressure fields and sources are considered statistically ergodic, hence acoustic variables investigated in the frequency domain. For the notations, this dependency is implicit and for instance every $\boldsymbol{p}$ below actually implies $\boldsymbol{p}(\omega)$.

1.1.2 Algebraic formulation

Considering a pressure field originating from a given physical support, the aim of acoustic imaging is to recover a proper depiction of the sources by the mean of a finite set of microphone measurements. A simple mathematical statement of this purpose reads as

$$\text{Find} \quad \boldsymbol{q} \in \mathbb{C}^N \quad \text{satisfying} \quad \boldsymbol{p} = \boldsymbol{H}\boldsymbol{q}, \tag{1.1.1}$$

with $\boldsymbol{p} \in \mathbb{C}^M$ and $\boldsymbol{H} \in \mathbb{C}^{M \times N}$.

The definition of each components in Eq.(1.1.1) is described in this subsection, in light of the diagram displayed on Fig-1.1 below.

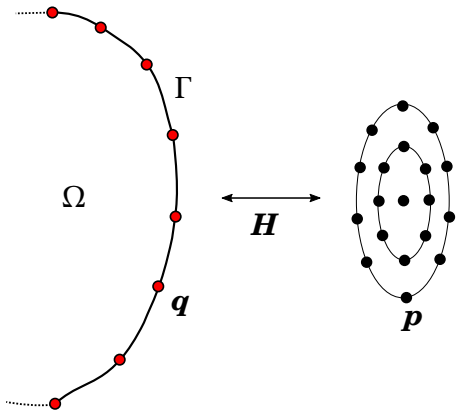

FIGURE 1.1 - *Acoustic imaging schematic set-up. A set of acoustic sources $\boldsymbol{q}$ supported by a discretized three-dimensional surface Γ is identified from the microphone pressures $\boldsymbol{p}$, featuring the inversion of a propagation model $\boldsymbol{H}$.*

Microphonic pressures

$\boldsymbol{p} \in \mathbb{C}^M$ denotes in this manuscript the acoustic pressures measured by an array of M microphones. It is an essential input data to any acoustic imaging technique and the relevant informations concerning microphone pressures are shortly discussed here. Pressures may be treated via their cross correlation matrices defined as

$$\boldsymbol{S}_{pp} = \mathbb{E}\left[\boldsymbol{p}\boldsymbol{p}^{\mathsf{H}}\right] \tag{1.1.2}$$

where $\cdot^{\mathsf{H}}$ denotes the transpose conjugate and $\mathbb{E}[\cdot]$ the statistical expectation. Since stationary signals of finite duration are under scrutiny, the latter is estimated in practical as a mean on N_b overlapping time blocks as

$$\boldsymbol{S}_{pp} = \frac{1}{N_b}\sum_{n=1}^{N_b} \boldsymbol{p}_n \boldsymbol{p}_n^{\mathsf{H}}. \tag{1.1.3}$$

Consequently, the inverse problem in practical is often tackled in its quadratic formulation

$$\boldsymbol{S}_{pp} = \boldsymbol{H}\boldsymbol{S}_{qq}\boldsymbol{H}^{\mathsf{H}} \tag{1.1.4}$$

where $\boldsymbol{S}_{qq}$ is the source cross spectral matrix containing their squared amplitudes in its diagonal and their phase relations in its upper and lower triangular coefficients.

Two major issues related to array pressures have major impacts on the quality of source reconstruction. First has to be mentioned the noise added during the measurement process. In practical, the accurate inverse problem definition turns out to be

$$\boldsymbol{p} = \boldsymbol{H}\boldsymbol{q} + \boldsymbol{c} \tag{1.1.5}$$

where $\boldsymbol{c} \in \mathbb{C}^M$ is a noise vector. The probabilistic description of noise strongly relies on its physical cause and a large variety of models and signal processing algorithms were described in the denoising literature. For an exhaustive overview of state-of-the-art techniques, the reader might refer to Dinsenmeyer *et al.* (2020) when dealing with turbulent boundary layer noise in closed wind tunnel and to Hald (2019) for denoising in general. A proper denoising step proved out to lead to significant improvements of source identification, but often at the cost of additional computation time and algorithmic developments. For the latter motives, only the diagonal removal approach from Sijtsma (2004) is used for the aeroacoustical test cases later in chapter 4. It consists in setting $\mathrm{diag}\left(\boldsymbol{S}_{pp}\right)$ to zero to

straightforwardly remove uncorrelated noise. Since the CSM diagonal does not carry any phase information, Dougherty (2002) showed that beamforming does not suffer from this loss of information. However, it not the case for other refined imaging algorithms and diagonal removal must be avoided when using inverse methods evoked later in the current chapter.

The second critical aspect linked to the input pressure in Eq.(1.1.1) lies in the geometrical disposition of the microphones. The coverage area as well as the microphones disposition plays an important role in the source mapping performances, and large levels of accuracy must be reached regarding the relative source to microphone distance measurements.

FIGURE 1.2 - *MicrodB Sound Camera (117 MEMS microphones).*

A substantial number of authors proposed solutions for array design and positioning: Haubrich (1968) introduced co-arrays for a morphologic optimization, Nordborg *et al.* (2000); Schulze *et al.* (2004) benchmarked classic geometries and Chiariotti *et al.* (2019) reviewed their influence on beamforming (see section 1.2.1) accuracy. More recently, Gilquin *et al.* (2019) drew insightful conclusions on optimal array positioning from a statistical point of view.

Potential sources

Unknowns of the inverse problems, the sources $\boldsymbol{q} \in \mathbb{C}^N$ is a delicate notion in acoustic imaging and especially since the advent of three-dimensional source mapping. The correct understanding relies on the analytical origin of Eq.(1.1.1), proposed by Schenck (1968), depicting the pressure p stemming from a volumic set of sources q bounded by the close surface Γ:

$$p(\boldsymbol{r}) = \mathrm{i}\omega\rho \int_{\Omega} q(\boldsymbol{r}_0) G(\boldsymbol{r}, \boldsymbol{r}_0) \mathrm{d}\Omega(\boldsymbol{r}_0) \tag{1.1.6}$$

where $\boldsymbol{r}$ denotes any observer position outside the volumic source region Ω in Fig-1.1 and $G(\cdot,\cdot)$ stands for the free field Green function of the wave equation. Eq.(1.1.6) is equivalent to the Kirchhoff-Helmholtz integral and is further discussed later in section 2.2. In the two-dimensional case, the sources geometrical support is usually defined by planar grids : by necessity, what is sought is a distribution of sources on a plane that reflects as closely as possible the ground truth $q(\boldsymbol{r}_0)$ in Eq.(1.1.6). Depending on the case under scrutiny, such an assumption is seldom relevant and three-dimensional source description is more likely to fit with reality.

From that perspective, two leads emerged from the recent literature. The most direct approach is to rule out every *a priori* assumption on the source position and to process volumetric source mapping. However, such meshing engages extremely high dimensions and prohibitive computational resources (see Battista (2019, section 5.1)). Battista *et al.* (2021) implemented this brute force solution on an automotive test case and highlighted this concern. A reasonable option is to switch from Eq.(1.1.1) to an optimization problem where the sources positions are complete unknowns:

$$\text{Find} \quad N \in \mathbb{N} \text{ and } \left(q_j \in \mathbb{C},\, \boldsymbol{r}_j \in \mathbb{R}^3\right)_{j \leq N} \quad \text{that ensure} \quad \boldsymbol{p} = \boldsymbol{H}(\boldsymbol{r}_1, \ldots, \boldsymbol{r}_N)\boldsymbol{q}. \tag{1.1.7}$$

These techniques, called *gridless* methods, recently became of interest for the acoustic community. Sarradj (2022) used for example the singular value decomposition (SVD) of $\boldsymbol{S}_{pp}$ to infer the source positions. Chardon and Boureau (2021) proposed a mathematical assessment of a gridless beamforming showing good results on academical test cases. Gridless imaging is an upstream line of attack for volumic three-dimensional source identification that remains at an early stage of development in the acoustic community.

A more practical idea, wide spread in most 3D imaging articles, is to initialize the inverse problem with an important hypothesis on the source location by setting a pre-defined surface source grid for potential sources. By doing that, the issue of numerical efficiency is partly tackled and 2D inspired algorithms may be used. However, new stakes related to three-dimensional acoustic paths remain with the definition of the transfer model $\boldsymbol{H}$. This specific set-up is illustrated on Fig-1.3.

Transfer model

The $\boldsymbol{H}$ matrix represents here the acoustic propagation model between the potential sources and the microphones. Its parametrization is a cornerstone of the

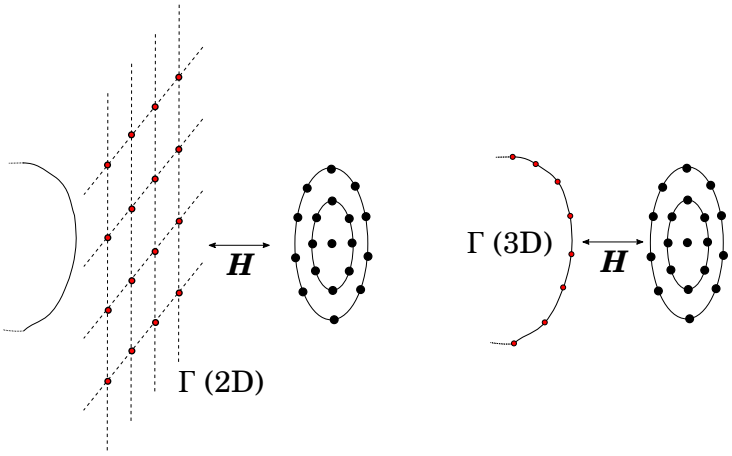

FIGURE 1.3 - *Paradigm shift between 2D (left) and 3D (right) sources support* Γ. *The stake arising with surfacic three-dimensional imaging lies in the changes in the transfer model for grid points on* Γ *that are no longer directly facing the planar array.*

inverse problem as it accounts for the physical model as well as it impacts the numerical stability. This is a main perspective of this PhD work and the literature on transfer functions and their interlinks with the inverse problem resolution exposed in section 1.3.

1.2 Practical inversion

Before getting at the heart of the problem of transfer models, it appears relevant to present the different classes of algorithms available in the literature to solve Eq.(1.1.1). For readers particulary interested in this aspect, Merino-Martínez *et al.* (2019) covered a comprehensive panel of imaging methods in his review article. In this section are listed all the methods used in the next chapters to test propagation models and benchmark their suitability with inversion processes commonly used by the acoustic imaging community.

1.2.1 Beamforming

The widespread use of beamforming relies on its robustness and the simplicity of its implementation. The basic idea is to deal with each potential sources $\left(q_j\right)_{j\leq N}$ independently from one another according to the same steps:

1. Compensate the phase shift and the amplitude attenuation from each microphone pressure $(p_i)_{i\leq M}$ due to its distance to the source.

2. Sum the delayed microphone signals and assume that the sound genuinely coming from the source will be summed coherently

Returning to Eq.(1.1.1), the mathematical description of beamforming is well known and reduces the linear system inversion to N scalar minimization problems. The underlying hypothesis is that all the sources to be identified are uncorrelated and well separated in space, so that each q_j could be processed separetely by minimizing the error to the measured pressures:

$$\hat{q}_j = \underset{q\in\mathbb{C}}{\arg\min} \left\| \boldsymbol{p} - \boldsymbol{H}_j q \right\|^2, \tag{1.2.1}$$

$\boldsymbol{H}_j$ being the j^{th} column of $\boldsymbol{H}$. Assuming that $\boldsymbol{H}$ is non-zero, an analytical solution arises from the derivation Eq.(1.2.1) and reads in its quadratic form as

$$\forall j \leq N, \quad \left|q_j\right|^2 = \frac{\boldsymbol{H}_j \boldsymbol{S}_{pp} \boldsymbol{H}_j^{\mathsf{H}}}{\left\|\boldsymbol{H}_j\right\|^4}. \tag{1.2.2}$$

This formulation, named Conventional Beamforming (CBF), is known to be fast and robust. CBF is theoretically justified for the identification of a single monopolar radiating source in a free field toward the array (see Chiariotti *et al.*, 2019, for a complete review of this method). Even if its relevance may be questioned when dealing with complex source distributions, it remains a reference in industrial applications and a comparison with CBF output is a necessary step for the evaluation of new acoustic imaging methods. Various declensions of Eq.(1.2.2) were designed in the literature (see Sarradj, 2012, for a review). Notably, a *coherence* version where the $\frac{1}{\|\boldsymbol{H}_j\|^4}$ is traded for a $\frac{1}{\|\boldsymbol{H}_j\|^2}$ normalization to avoid diverging values for q_j when $\left\|\boldsymbol{H}_j\right\|$ is critically small. From the mathematical standpoint, it no longer corresponds to the result of minimization process but a direct normalized scalar product between $\boldsymbol{p}$ and $\boldsymbol{H}_j$ stated as

$$\left|q_j\right|^2 = \frac{\boldsymbol{H}_j \boldsymbol{S}_{pp} \boldsymbol{H}_j^{\mathsf{H}}}{\left\|\boldsymbol{H}_j\right\|^2 \mathrm{Tr}\left(\boldsymbol{S}_{pp}\right)}, \quad \left|q_j\right| \in [0,1]. \tag{1.2.3}$$

Proposed by Leclère *et al.* (2020), it can be seen as an unquantified indicator that allows to seize the correlation between the simulated pressures on the array and the potential source on the j^{th} point of the grid.

For the sake of clarity, it should finally be mentioned that the combination of a transfer function $\boldsymbol{H}_j$ with a normalization weight (norm, squared norm, trace,

etc.) is referred to as *steering vector* in the beamforming literature.

3D beamforming with planar arrays

Given the historical development of acoustic imaging with two-dimensional source grids, industrial microphone arrays mostly follow planar geometries and especially in wind tunnels. A statement should therefore be made about the recent beamforming literature dedicated to 3D source mapping based on such hardware. When several planar arrays are used simultaneously for wind tunnel measurements, Porteous *et al.* (2015) and Sijtsma (2008) showed that the blocks of the CSM corresponding to the coherence between the arrays was likely to be damaged because of the aeroacoustic shear layer: its turbulences randomly delay or speed up the acoustics, leading to each microphone not sampling the pressure data coherently with its neighbours. To tackle this issue, it is often considered preferable to combine source maps of each array instead of performing CBF on the complete $\boldsymbol{S}_{pp}$ as

$$|q_j| = \left| \prod_{k \leq N_a} q_j^k \right|^{\frac{1}{N_a}}, \tag{1.2.4}$$

N_a denoting here the number of planar arrays. The idea with this geometric mean is to have the sidelobes related to each planar array being *leveled down* by the neighbour array responds, leading to a smoother source map (see Fig-1.4 (c)). This approach, named Multiplicative Beamforming (MBF), was recently reviewed by Lima Pereira *et al.* (2021) as well as other combination ideas.

Beamforming techniques suffer from extensively studied drawbacks. It is by design theoretically valid for uncorrelated and well separated sources only and does not provide any information on the source phase relations. Furthermore, its efficiency strongly depends upon the array geometry as spatial aliasing artefacts occur when microphones are regularly spaced. This phenomena is termed *side lobes* in the literature and paved the way for post processing algorithm for beamforming.

Deconvolution approaches

Proposed notably by Ehrenfried and Koop (2007) and Sijtsma (2007), deconvolution is a commonly used extension of beamforming. The main idea is to post-process the beamforming map by picking its maximum source, back-propagating it toward the array and subtracting its contribution from the CSM. Such a technique does not extend beamforming beyond the uncorrelated sources hypothesis,

but it allows to *clean* source map from sidelobes, hence the CLEAN-SC denomination. By doing so, the resolution of the source maps gets drastically increased and the sources a reduced to set of isolated points on the grid.

Simply put, its implementation is an iterative subtraction of the beamforming maxima contributions: once CBF is computed, the maximum index $j_{\max} = \arg\max_j |q_j|$ is selected and back propagated toward the microphone position as

$$\boldsymbol{S}_{pp}^{j_{\max}} = \boldsymbol{H}_{j_{\max}} q_{j_{\max}} \boldsymbol{H}_{j_{\max}}^{\mathsf{H}}. \tag{1.2.5}$$

Then $\boldsymbol{S}_{pp}^{j_{\max}}$ is removed to obtain a *clean* CSM :

$$\boldsymbol{S}_{pp}^{c} = \boldsymbol{S}_{pp} - \boldsymbol{S}_{pp}^{j_{\max}} \tag{1.2.6}$$

and $\boldsymbol{S}_{pp}^{c}$ is provided to CBF for next iteration. A CLEAN-SC map example obtained on a basic case is given on Fig-1.4 (d).

1.2.2 Inverse methods

Lastly remains the generic possibility to mathematically invert the matrix $\boldsymbol{H}$. Inverse methods pertain to an entirely different strategy, as sources are now considered as a whole and their phase relations are sought alongside their amplitudes.

Given that the usual number of grid points exceeds by far the number of microphones, Eq.(1.1.1) boils down to an undertermined linear systems solvable with optimization algorithms:

$$\hat{\boldsymbol{q}} = \arg\min_{\boldsymbol{q}\in\mathbb{C}^N} \|\boldsymbol{p} - \boldsymbol{H}\boldsymbol{q}\|^2 + \mu^2 \|\boldsymbol{q}\|_p, \tag{1.2.7}$$

or in its quadratic form

$$\hat{\boldsymbol{S}}_{qq} = \arg\min_{\boldsymbol{S}_{qq}\in\mathbb{C}^{N\times N}} \left\| \boldsymbol{S}_{pp} - \boldsymbol{H}\boldsymbol{S}_{qq}\boldsymbol{H}^{\mathsf{H}} \right\|^2 + \mu^2 \left\| \boldsymbol{S}_{qq} \right\|_p \tag{1.2.8}$$

$\|\cdot\|$ for matrices being here the Frobenius norm, and $\|\cdot\|_p$ for matrices being defined by $\|\boldsymbol{A}\|_p = \sup_{\boldsymbol{x}} \dfrac{\|\boldsymbol{A}\boldsymbol{x}\|_p}{\|\boldsymbol{x}\|_p}$.

This kind of formalism comes with fundamental differences to the beamforming techniques listed so far:

- As the full $\boldsymbol{S}_{qq}$ matrix is calculated at one go, sources are investigated as interdependent one to another which means that inverse methods enable the

identification of correlated sources. Comparatively to beamforming, this constitutes a major improvement for cases where interferences between sources are critical.

- The inverse problem is almost always underdetermined as the number of grid points is usually far greater than the number of microphones and $M << N$. It thus requires a selection among all the source distribution satisfying Eq.(1.1.1). This is achieved with the introduction of a regularization parameter μ, used to filter the only solution minimizing the L^p norm of $\boldsymbol{q}$. The choice of p then relies on physical hypothesis made by the user on the source distribution.

- Solving Eq.(1.2.7) pertains to the use of $\boldsymbol{H}$ pseudo inverse. This accentuates the imaging process dependency to the conditioning number

$$\kappa(\boldsymbol{H}) = \|\boldsymbol{H}\| \left\|\boldsymbol{H}^{+}\right\|, \tag{1.2.9}$$

  and makes it sensitive to numerical and measurement noise. Here again, regularization must be added to tackle this issue.

The settings of the aforementioned regularization, i.e. the choice of the p-norm and the tuning of μ, is a widely studied problem with multiple answers. This was a brief depiction of the inverse method framework for acoustic imaging, the reader may refer to Leclère *et al.* (2017) for deeper insights.

1.2.2.1 Bayesian framework

A current state-of the-art algorithm to solve Eq.(1.2.7) is Bayesian Focusing (BF), initially proposed by Antoni (2012). The underlying principle of BF is briefly resumed in this section. The starting point is to consider the unknown $\boldsymbol{q}$ of the inverse problem as a random variable and determine its Probability Density Function (PDF) based on the information provided by the array measures, noted as $[\boldsymbol{q}|\boldsymbol{p}]$. Various statistical outputs of this PDF can be considered as the actual source set corresponding to the measured pressures, but a commonly used one is the maximum a posteriori

$$\hat{\boldsymbol{q}} = \arg\max_{\boldsymbol{q}} [\boldsymbol{q}|\boldsymbol{p}]. \tag{1.2.10}$$

The latter should be interpreted as the likeliest source distribution regarding

the measurements. The key part is to use the Bayes rule stating

$$[\boldsymbol{q}|\boldsymbol{p}] = \frac{[\boldsymbol{p}|\boldsymbol{q}][\boldsymbol{q}]}{[\boldsymbol{p}]}. \tag{1.2.11}$$

Many probability laws are relevant candidates to model $[\boldsymbol{p}|\boldsymbol{q}]$, the prior on sources $[\boldsymbol{q}]$ and potential noise (see for example Xenaki *et al.* (2016)) assuming various hypothesis. With concern to remain in a general framework, the choice was made here to stick to Gaussian distributions.

$$[\boldsymbol{p}|\boldsymbol{q}] \sim \mathcal{N}\left(\boldsymbol{H}\boldsymbol{q}, \beta^2 \boldsymbol{I}_M\right) \qquad \text{and} \qquad [\boldsymbol{q}] \sim \mathcal{N}\left(0, \alpha^2 \boldsymbol{\Omega}_{\boldsymbol{q}}\right) \tag{1.2.12}$$

where $\beta^2 \boldsymbol{I}_M$ (identity matrix) stands for the energy of uncorrelated measurement noise, α^2 the a priori overall energy of the sources and $\boldsymbol{\Omega}_{\boldsymbol{q}} \in \mathbb{R}^{N\times N}$ their a priori coherence structure. Then according to Antoni *et al.* (2019, section 2.3), the combination of (1.2.10) and (1.2.11) leads to

$$\hat{\boldsymbol{q}} = \arg\min_{\boldsymbol{q}}(-\ln([\boldsymbol{p}|\boldsymbol{q}][\boldsymbol{q}])) = \arg\min_{\boldsymbol{q}}\left(\|\boldsymbol{p}-\boldsymbol{H}\boldsymbol{q}\|_2^2 + \frac{\beta^2}{\alpha^2}\left\|\boldsymbol{\Omega}_{\boldsymbol{q}}^{-1}\boldsymbol{q}\right\|_2^2\right). \tag{1.2.13}$$

and

$$\boldsymbol{q} = \boldsymbol{\Omega}_{\boldsymbol{q}}^{1/2}\boldsymbol{H}^{\mathsf{H}}\boldsymbol{S}^{-1}\boldsymbol{U}\boldsymbol{H}\frac{\boldsymbol{S}}{\boldsymbol{S}^2 + \frac{\beta^2}{\alpha^2}}\boldsymbol{U}^{\mathsf{H}}\boldsymbol{p} \tag{1.2.14}$$

where $\boldsymbol{S}$ and $\boldsymbol{U}$ arise from the singular value decomposition (SVD).

$$\boldsymbol{H}\boldsymbol{\Omega}_{\boldsymbol{q}}^{1/2} = \boldsymbol{U}\boldsymbol{S}\boldsymbol{V}^{\mathsf{H}} \tag{1.2.15}$$

with the $\frac{\beta^2}{\alpha^2}$ ratio corresponding to a regularization parameter tuned in accordance with the algorithm proposed by Pereira *et al.* (2015). This is was shown (Antoni, 2012) to be equivalent to the solution obtained by Tikhonov (1963). It should be noticed that this regularization parameter also happens to be the ratio between the noise and the sources energies, which gives a insightful mathematical meaning the signal-to-noise ratio. Finally, the whole process can be iterated (iterative Bayesian Focusing (iBF), Antoni *et al.*, 2019) to enforce a spatial energy concentration using the obtained source strengths at step $n-1$ as an updated prior for step n:

$$\boldsymbol{\Omega}_{\boldsymbol{q}}^{(n)} = \left(\mathrm{diag}\left(\boldsymbol{q}^{\mathsf{H}}\boldsymbol{q}\right)^{(n-1)}\right)^{1-\frac{p}{2}}. \tag{1.2.16}$$

$p \in [1,2]$ in Eq.(1.2.16) is a user defined norm parameter that will favor either a spatial sparsity (L^1 norm) an energy concentration (L^2 norm) of the sources.

This probabilistic strategy can be deemed as a unified approach of solving the inverse problem of acoustic imaging (Le Magueresse, 2016, chapter 4), as it encompasses various norm choices and regularization techniques under the same formalism. The adaptability of iBF, relevant for sources correlated or not, sparse or not, comes evidently at the cost of a more complex implementation and a larger computational cost (one SVD of a $M \times N$ matrix is performed at each iteration).

By way of illustration, every algorithm presented so far was used for the identification of a single monopole on a sphere using three planar arrays. The resulting source maps on Fig-1.4 shows how their relative assets gets reflected in practical.

1.3 State of the art on acoustic transfer functions

An wide panel of techniques for the construction of *ad hoc* Frequency Response Functions (FRF) for acoustic imaging already exists. The purpose of the section below is to overview comprehensively this panel and thus justify the positioning of the current document.

Still in the context of section 1.1, FRFs for acoustic imaging are formally defined for each frequency as

$$\boldsymbol{H} \in \mathbb{C}^{M\times N} \quad \text{such as} \quad \boldsymbol{H}_{i,j} = \frac{p_i}{q_j} \quad \forall i \leq M, j \leq N. \tag{1.3.1}$$

It ideally translates every physical feature likely to affect the sound propagation : Sommerfeld condition, Helmholtz equations, diffraction around the object, reflections on the ground, aeroacoustic contributions, etc.

1.3.1 Elementary sources

The historical choice to fill $\boldsymbol{H}$ is to consider every potential source as an acoustic monopole radiating in a free field medium, i.e.

$$\boldsymbol{H}_{i,j} = -\mathrm{i}\omega\rho G\left(\boldsymbol{r}_i, \boldsymbol{r}_j\right) = -\mathrm{i}\omega\rho \frac{e^{\mathrm{i}kr_{ij}}}{4\pi r_{ij}}, \quad \text{where} \quad r_{ij} = \left\|\boldsymbol{r}_i - \boldsymbol{r}_j\right\|, \tag{1.3.2}$$

where $\boldsymbol{r}_i, \boldsymbol{r}_j$ stand for the respective positions of the grid points and the microphones. It was introduced at the early stages of acoustic beamforming, extensively studied over the last decades. Nelson and Elliott (1992) demonstrated the analytical formulation of $\boldsymbol{H}$, and its behaviour regarding the conditioning number can be summarized as follows (see Nelson and Yoon, 2000, for the detailed explanations):

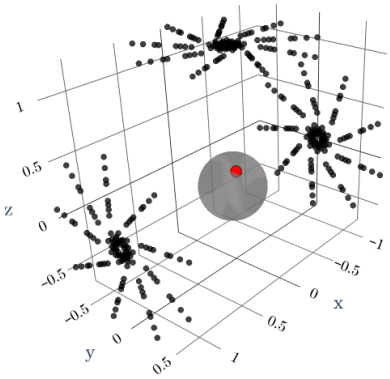

(a) *Ground truth source location (red dot).*

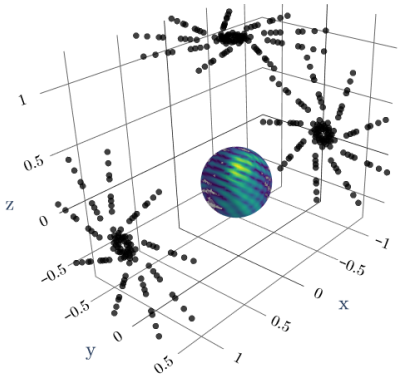

(b) *CBF*

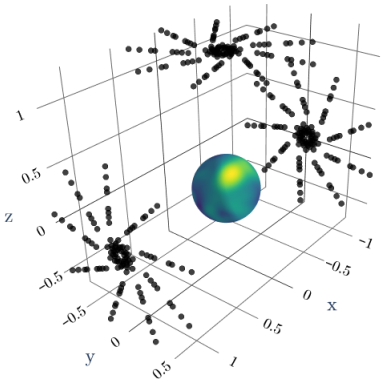

(c) *MBF*

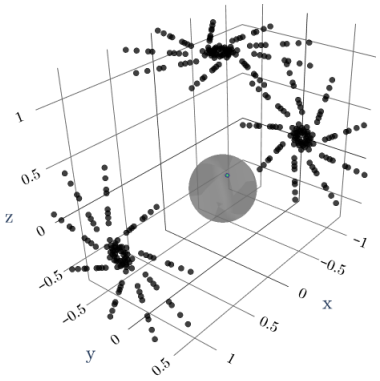

(d) *CLEAN-SC*

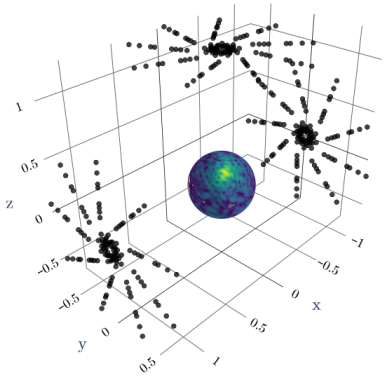

(e) *BF*

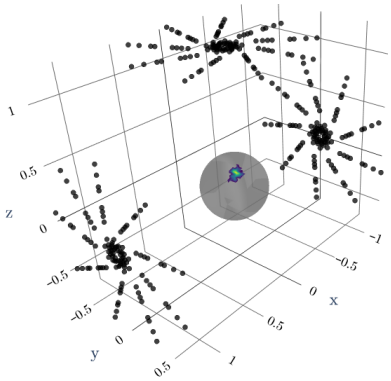

(f) *iBF*

FIGURE 1.4 - *Identification of a monopole on a rigid sphere at* $ka = 19$ *using free field transfer functions and various imaging algorithms. Levels are relative to the source strength and plotted within a 20 dB dynamic range.*

- Overall, monopolar transfer functions tend to become numerically unstable at low frequencies.
- Same goes for arrays that feature small distances between microphones with respect to the wavelength under scrutiny, as they do not allow to properly capture the patterns of the pressure field on a significant amount of time periods.
- Finally, κ becomes large when the ratio of the array-grid distance to the distance between grid points is of a large order of magnitude.

When used with beamforming, the characteristics of monopolar FRFs are deeply benchmarked, for example by Sarradj (2012) who unravelled all the normalization possibilities and their properties depending on the goal of the imaging process. Chardon (2022) also worked this aspect from the statistical point of view and concluded that coherence beamforming of Eq.(1.2.3) should be used to figure out source positions while CBF is suitable for source strength estimation.

Later on, Jordan *et al.* (2002) started to investigate the use of directional sources and introduced dipolar FRF. It reads as

$$\boldsymbol{H}_{i,j} = -\mathrm{i}\omega\rho D\left(\boldsymbol{r}_i, \boldsymbol{r}_j, \boldsymbol{d}\right) = -\mathrm{i}\omega\rho \frac{e^{\mathrm{i}kr_{ij}}}{4\pi r_{ij}} \left(-1 + \mathrm{i}kr_{ij}\right) \frac{2\pi\left(\boldsymbol{r}_i - \boldsymbol{r}_j\right)\cdot\boldsymbol{d}}{kr_{ij}^2}, \tag{1.3.3}$$

$\boldsymbol{d}$ being the axis along which are aligned the two opposit-phased monopoles forming the dipoles (see Fig-1.5-(b) for a display of the radiative patterns). Porteous *et al.* (2015, Fig-1) or Zhou *et al.* (2020, Fig-5) pointed out how counter-productive could acoustic imaging become when using Eq.(1.3.2) as FRFs to identify sets of dipolar sources.

Here again, this elementary transfer model is appraised in a consistent panel of articles and its main issues are stated :

- The setting of $\boldsymbol{d}$ can be either fixed as assumption from the physical origin of sound emission (see section 1.4), or considered as an additional unknown in CBF as did Gao *et al.* (2020) using a greedy process:
  1. Implementation of an *angular grid* $(\theta_d)_{d\leq N_d}$ covering $[0,\pi]$.
  2. Beamformer calculation for every orientation

$$q_j^d = \frac{\boldsymbol{H}_j^d \boldsymbol{S}_{pp} \boldsymbol{H}_j^{d\mathsf{H}}}{\left\|\boldsymbol{H}_j^d\right\|^4} \quad \text{where} \quad \boldsymbol{H}_{ij}^d = D(\boldsymbol{r}_i, \boldsymbol{r}_j, \theta_d) \tag{1.3.4}$$

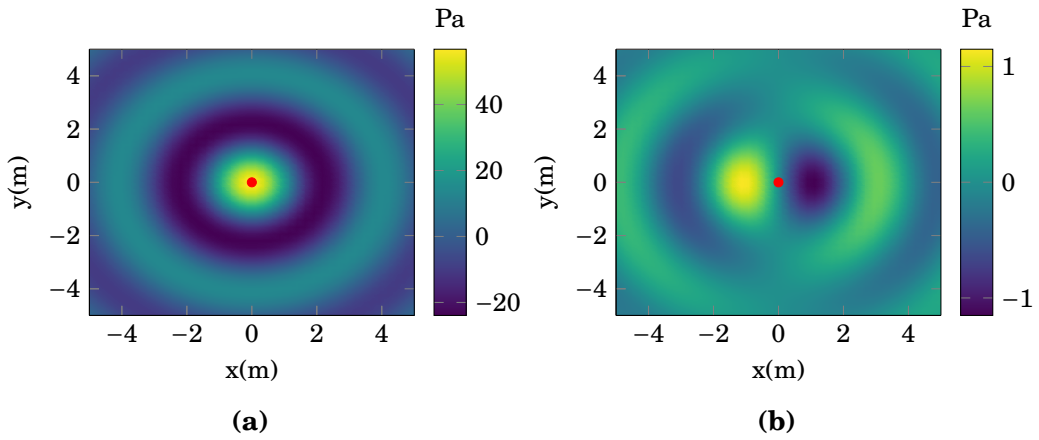

FIGURE 1.5 - *Acoustic pressure (real part) of a monopole (a); and a dipole with* $\boldsymbol{d} = (1,0,0)$ *(b) at* $f = 100$ *Hz. The red dot indicates the position of the sources.*

3. Selection of the maximum valued result

$$q_j = \max_{d \leq N_d} q_j^d. \tag{1.3.5}$$

Proved to be operational, this strategy yet adds a $\mathcal{O}(N_d)$ factor to the computational cost likely to be problematic when using more advanced inverse methods.

- Directivity may imply the apparition of masked area (grid points *hidden* from the microphone array) when used for three-dimensional cases. In mathematical terms, this leads to null columns of $\boldsymbol{H}$ and additional troubles when solving Eq.(1.1.1). This aspect is not much tackled in the literature (Evans *et al.*, 2019, worked on a spatial filter for beamforming). It is hence discussed in the scope of this thesis in sections 1.4 and 2.3.

Concerning the sources strength, it should be underlined that the issue of dipole quantification is hardly tackled in the literature. The actual definition of the pressure radiated by two monopoles in opposition of phase should be

$$\boldsymbol{H}_{i,j} = k^2 L \rho c_0 D\left(\boldsymbol{r}_i, \boldsymbol{r}_j, \boldsymbol{d}\right), \tag{1.3.6}$$

featuring the distance L between the two monopoles as another prior information on the dipole. Within both the acoustic analogies and the acoustic imaging frameworks, dipolar-like radiation patterns more than genuine dipoles physically stemming from two out-of-phase monopoles are sought, hence a case dependent

quantification.

In cases where no assumption is made on the nature of the noise, Suzuki (2011) designed a correction term to *normalize* dipolar beamforming levels with those usually obtained with conventional monopolar beamforming:

$$\boldsymbol{H}_{i,j} = \frac{r_{\mathrm{mc}}}{k r_{\mathrm{aper}}} D\left(\boldsymbol{r}_i, \boldsymbol{r}_j, \boldsymbol{d}\right) \tag{1.3.7}$$

with r_{mc} the mean distance to the array center and r_{aper} the array aperture (i.e. the maximum distance between to microphone).

In addition to that, it may also be noticed some promising tries, for example from Bader (2010), to mix various types of elementary source models and recover sound sources defined as

$$\boldsymbol{H}_{i,j} = -\mathrm{i}\omega\rho \frac{e^{\mathrm{i}kr_{ij}}}{4\pi r_{ij}\left(1-\alpha\left(1-\frac{(\boldsymbol{r}_i-\boldsymbol{r}_j)\cdot\boldsymbol{d}}{r_{ij}}\right)\right)}, \tag{1.3.8}$$

α being a user defined parameter defining some sort of a balance between monopoles and dipoles. One could also quote Leclère *et al.* (2005) who designed a *directive monopole* source model, by introducing a directivity function in Eq.(1.3.2).

Such models offer on the one hand the advantage of being numerically robust and convenient for real time sound source identification since they can be computed on the fly. On the other hand, any additional boundary condition introduced by the presence of a scattering object or a reflecting ground is totally ignored in this approach and misleading sources are likely to be highlighted (see for example Le Magueresse *et al.*, 2020, section 4). Having more precise depiction of the actual propagation from the sources toward the microphones is a lever of improvement for source reconstruction. Various options to achieve this purpose made the case of a recent literature, the rest of the current section is dedicated to their overview.

1.3.2 Spherical transfer model

Restricted to specific array and structure geometries, a straightforward option is to rely on analytical FRF formulations. The latter are now extensively documented and the transfer functions of elementary sources in the vicinity of simple geometries such as cylinder, boxes and planes are now well known (reader may refer to Skudrzyk, 1971, for a wide panel of available models). This section exemplifies their use by putting the focus on Sphere Related Transfer Function (SRTF). It is the most commonly used refined FRF in the acoustic imaging community for

applications in enclosed spaces with rigid spherical arrays (see Haddad and Hald, 2008; Schmitt *et al.*, 2010). It also turns out to be an insightful reference all along this PhD work to benchmark FRF simulation methods presented in the next two chapters.

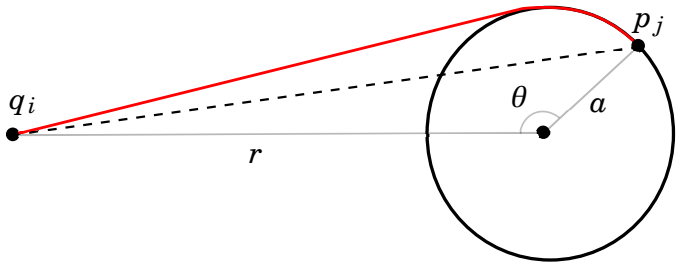

FIGURE 1.6 - *Considering a rigid sphere of radius a, SRTF analytically provides the pressure at p_i given a monopole of volumic flow q_j while taking into account the scattered path in red instead of the free field one (dashed).*

As displayed on Fig-1.6, SRTF pertains to directly compute the transfer function between a grid point and a microphone located on a infinitely rigid sphere. The underlying mathematical development can be found in (Williams, 1999, section 8.8), it is based on spherical harmonics decomposition and reads as (with the notations of Fig-1.6)

$$\boldsymbol{H}_{i,j} = \frac{-\mathrm{i}\rho c}{4\pi a^2} \sum_{n\in\mathbb{N}} (2n+1) \frac{h_n(k\,\|\boldsymbol{r}_i\|)}{h_n'(ka)} P_n\left(\frac{\boldsymbol{r}_i \cdot \boldsymbol{r}_j}{\|\boldsymbol{r}_i\|\,\|\boldsymbol{r}_j\|}\right), \tag{1.3.9}$$

h_n, h_n' and P_n respectively referring to spherical Bessel Functions of second kind and order n, its derivative, and Legendre polynomials of order n.

The formulation above does not provide the same set-up ease as those of Eq.(1.3.2, 1.3.3,1.3.8), but is still easily manageable numerically speaking with modern processors. Pereira (2013, chapter 2) showed empirically that the maximum order $n_{\max}$ to ensure a truncation error lesser than 10^{-9} on the sum could be linked to the frequency of interest through

$$n_{\max} > 1.2(ka)^2 + 8\frac{r/a+1}{r/a}, \tag{1.3.10}$$

while Duda and Martens (1998, Appendix B) proposed an accelerated routine to compute high orders (used for every computation of SRTFs in this document).

With Fig.1.7 can be appreciated the contribution of the SRTF in comparison with a free-field elementary source. In terms of FRF for imaging applications,

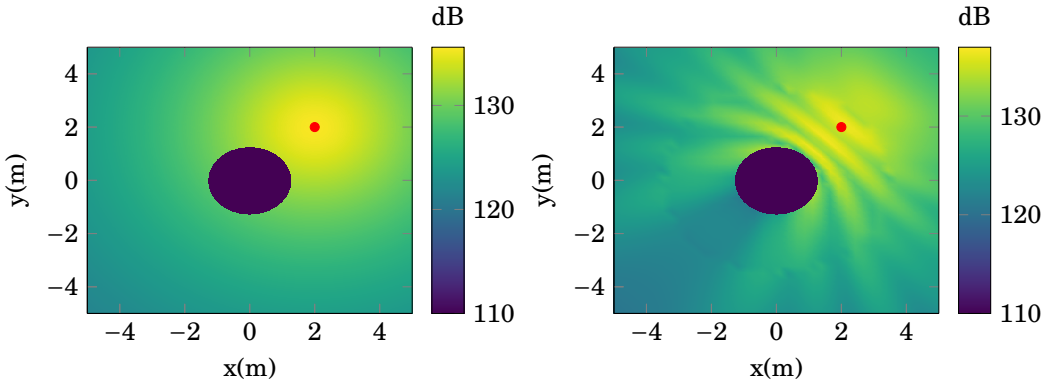

FIGURE 1.7 - *Acoustic pressure (amplitude) of (a) a free-field monopole; (b) a monopole scattered by a rigid sphere of radius $a = 1$ m at $ka = 2.1$. The red dot indicates the position of the sources.*

Rafaely (2015) summarized the whole scope of algorithms based on the use of SRTF with spherical arrays mainly for applications in enclosed space imaging. Holland and Nelson (2012) showed experimentally such non free-field propagation improves the quality of source reconstruction when fed to both beamforming and inverse methods. Typically, misleading conclusions can be drawn on source location at high frequencies as exemplified on Fig-1.8, and this point is outlined in detail later on in section 3.4.

1.3.3 FRF construction for 3D arbitrarily shaped geometries

At that stage, the logical continuation for the design of a consistent process of three-dimensional imaging is to extend the results obtained with SRTF to arbitrarily shaped geometries. As emphasized with Fig-1.3 the free-field assumption loses its relevancy with three-dimensional grids, and a strategy to provide FRFs taking into account scattered propagations between grids and arrays needs to be proposed when the chosen boundary Γ matches the skin of the radiating body. The two next subsections survey those already assessed in the literature.

1.3.3.1 Measured transfer functions

A first option consists in recording experimentally the FRFs. Although the relatively simple protocol (the experimenter is supposed to move a calibrated source along every control points and save the signal recorded by the microphones for each one of them), the process is tedious and time consuming but proved out to

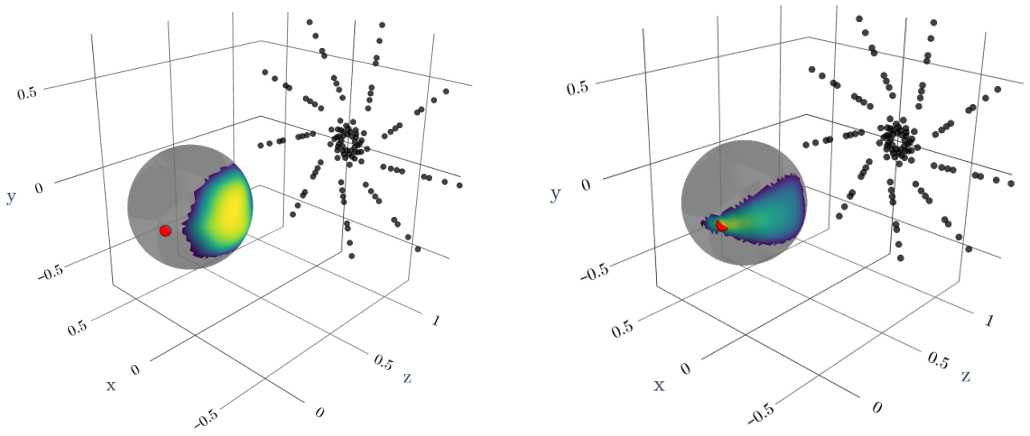

(a) **(b)**

FIGURE 1.8 - *CBF example maps obtained on simulated data at $ka = 16$; (a) Free-field transfer functions; (b) SRTF. The red dot indicates the ground truth position of the source, which was purposely placed on the opposite side from the planar array (black dots). It is clear in that case that an accurate transfer model is required to localize the source.*

yield fine results (see Holland and Nelson, 2012; Dumbacher and Brown, 1997). Considering that actual models involve thousands of grid points and hundreds of microphones, it may however be considered as an unworkable option nowadays. In addition to that, the FRF refinement brought by the inclusion of reflections and additional facilities effects is not worth the error introduced during the measurements, to such a point that this latter alternative is seldom if ever used.

1.3.3.2 Simulated transfer function

Ultimately, a relevant course of action is to turn toward simulation algorithms. As the use of numerical methods such as Boundary and Finite Element methods (FEM/BEM) became widespread over the last decades (see Chandler-Wilde and Langdon, 2007, for an overview), the acoustic imaging naturally gave tries to use them to compute transfer functions. Veronesi and Maynard (1989); Bai (1992); Valdivia and Williams (2007) first highlighted how BEM could be suitable with the simulation of scattered plane propagation including the evanescent nearfield components and used the latter for NAH with improved results.

Regarding the set-up presented in section 1.1, i.e. FRFs of point sources on the skin of a structure, FRFs based on Boundary Element Methods got introduced

to beamforming and inverse methods via the aeroacoustic applications of Evans *et al.* (2019) who used them to apply CBF on a rear-view mirror (see Fig-1.9).

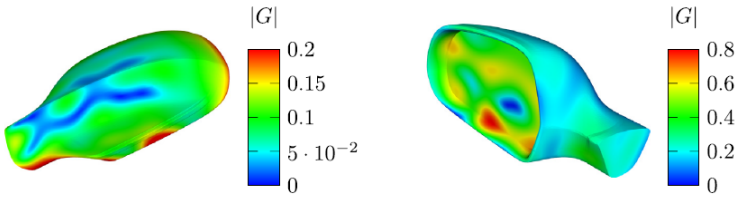

FIGURE 1.9 - *FRF (volumic flow amplitude) on a rear view mirror from an observer on the car window at $f = 4000$ Hz, from Evans* et al. *(2019).*

Lehmann *et al.* (2022) used BEM as well while working on a rotating heat exchanger and demonstrated that their refined FRFs reduced CBF sidelobes at high frequencies compared to when free-field ones were used. These two references do not mention the computational effort required to perform their simulation, but both of them used accelerated Fast Multipole Methods (Coifman *et al.*, 1993; Alouges *et al.*, 2017) as BEM comes with demanding needs of RAM and processor resources. Over and above the implementation of the method itself, BEM also requires a fine mesh management expertise. All in all its complexity can be considered disproportionate regarding the rather simple implementation of the inversion algorithms of section 1.2 and the previous approaches to build FRFs.

Other algorithms borrowed to computational acoustics were assessed for source identification in complex environments. Jeong and Ih (2009) applied ray casting for enclosed imaging, came out with strong results but restrictive hypotheses on the free-field propagation inside the enclosure and the frequency range of validity. For external acoustic imaging, Bousabaa (2018) designed an algorithm where $\boldsymbol{H}$ is the unknown and is optimized to have measurements matching with CFD data. Here again, each of this technique provides accurate results on specific test cases, at the cost of a loss in computation time and flexibility regarding the acoustic scene.

This leads to the initial purpose of this PhD work, that is to say the conception of a FRF simulation tool that might be:

- Suitable with a large span of cases, both regarding the shape of Γ and the frequency range of usability.
- Accurate enough to yield improvements in terms of source localization and quantification.

- Realtively easy to implement and prone to be tailored for specific applications from engine bench imaging to wind tunnel applications.

Such a design brief pointed out the Equivalent Source Method (ESM) of Koopmann *et al.* (1989) as an appropriate lead. Initially investigated in Le Magueresse (2016, Chapter II.3), ESM for FRF simulation was a major part of this work that is reported in details in Chapter 2.

1.4 Aeroacoustic models for wind tunnel applications

Bearing in mind the application cases of the last chapter, an additional statement about FRF models used for aeroacoustic source identification in wind tunnel is relevant. This last section covers briefly the aeroacoustic analogy formalism and highlights the part of it used in the framework of this document.

1.4.1 Aeroacoustic analogies

Given the complexity of the hydrodynamic phenomena responsible for noise production, a large field of past aeroacoustic research was dedicated to the elaboration of acoustic analogies in order to avoid the direct resolution of the Navier-Stokes equations. The use of aeroacoustic analogies consists of a clear separation between a source area and an observer area. This distinction arises from a derivation of the fluid mechanics equations that boils down to an inhomogeneous wave equation, from which the acoustic pressure in the observer region can be inferred from aerodynamic quantities in the source region. Using integral methods, the formalism of acoustic analogies allows the computation of the far field propagation of aerodynamically produced noise at the cost of a local knowledge the flow properties.

From the introduction of aeroacoustic analogies by Lighthill (1952) to the current state of the art, a wide range of source terms interpretations were established with regard to the hypotheses made on the test case.

Considering the set up of wind tunnel measurements, i.e. sound received by stationary observers from the interaction of a flow and a rigid structure, a redraft of Lighthill's equations were proposed first by Curle (1955) and buttressed by Ffowcs Williams and Hawkings (1969).

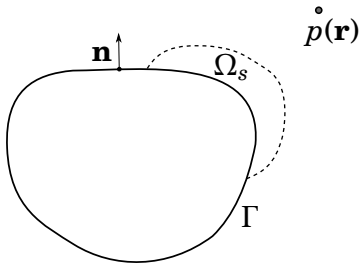

FIGURE 1.10 - *FW-H schematic set up. Ω_s accounts for the source area, and Γ denotes the boundary of a rigid object. The pressure at the observer point $\boldsymbol{r}$ can be obtained from the source region only.*

With respect to the notations on Fig-1.10, the generic formulation of Ffowcs Williams and Hawkings (FW-H) analogy in the spectral domain is given by

$$\begin{aligned} p(\boldsymbol{r}) = &- \int_{\Omega_s} \boldsymbol{T}_{xy} \frac{\partial^2 G(\boldsymbol{r},\boldsymbol{r}_s)}{\partial x \partial y} \mathrm{d}\boldsymbol{r_s} \\ &+ \int_{\Gamma} \boldsymbol{L}_x \frac{\partial G(\boldsymbol{r},\boldsymbol{r}_s)}{\partial x} \mathrm{d}\Gamma(\boldsymbol{r_s}) \\ &- \int_{\Gamma} \mathrm{i}\omega \boldsymbol{Q} G(\boldsymbol{r},\boldsymbol{r}_s) \mathrm{d}\Gamma(\boldsymbol{r_s}), \end{aligned} \tag{1.4.1}$$

where the $\cdot_x$ and $\cdot_{xy}$ underscripts denote here the implicit summation on every coordinates ($\boldsymbol{T}$ is a tensor and $\boldsymbol{L}$ an array). See for example Casalino (2002, p.422) for the full development leading to this result.

The three source terms on the right-hand of Eq.(1.4.1) are respectively defined as:

- Lighthill's tensor $\boldsymbol{T}$: associated to the quadrupolar radiation pattern, it accounts for the self-induced turbulence component in the source volume.
- The surfacic dipolar sources $\boldsymbol{L}$, often referred to as *loading noise*, transcribing the pressure changes due to the body reactive forces interacting with the flow.
- The surfacic monopolar sources $\boldsymbol{Q}$, sometimes named *thickness noise*, stemming from mass of fluid moved by the body surface.

Straightforward interpretations of the three source terms as proposed on Fig-1.11 may be untrue for some specific set ups. This source description is to be

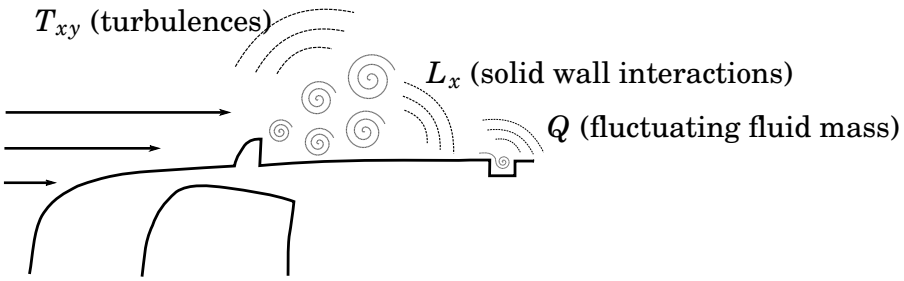

FIGURE 1.11 - *Source terms in FW-H analogy exemplified on a car (inspired by Blumrich and Helfer, 2017).*

understood as a guideline more than a actual set in stone definition (see Norton and Karczub, 2003, section 2.4.3, for a summarized rendering of FW-H analogy).

The commonly used process to benefit from this formulation is to numerically compute the physical properties of the flow inside Ω_s (pressure, particle velocity, density) thanks to an incompressible simulation tool (for instance a Large Eddy Simulation (LES) model) to get the acoustic pressure at any observer location outside the source region thanks to FW-H integrals.

Formulation 1C for wind tunnel applications

The classic FW-H formulation covers a wide range of applications as it addresses the noise produced by any moving body inside a turbulent flow. As the emphasis of this PhD was put on source identification from wind tunnel measurements, some major hypotheses can be considered to reduce the complexity of the source models.

First of all, it appears that the orders of magnitude of noise resulting from each source type can be related to the Mach number M_0 of the flow. This commonly used result (see again Norton and Karczub, 2003, section 2.4.3 for a brief justification) states that in terms of acoustic intensity

$$I_Q \sim \rho u^3 M_0, \quad I_L \sim \rho u^3 M_0^3, \quad I_T \sim \rho u^3 M_0^5. \tag{1.4.2}$$

Bearing in mind the fact that Mach number in automotive wind tunnel hardly exceeds $M = 0.1$, quadrupolar sources related to the turbulences proper sound are often neglected. Furthermore, since the body placed inside the flow is assumed perfectly rigid, the particle velocity on Γ matches the velocity field of the structure.

This leads to simplified writings of Q and $\boldsymbol{L}_x$ in (1.4.1). The last step to fall in the scope of wind tunnel testing and get a clearer view of (1.4.1) is to consider a convected wave when computing G. The set-up of moving sources in a medium at rest was formulated by Farassat (1975) and Brentner and Farassat (2003) as the

1A expression of FW-H analogy, and refined later on by Najafi-Yazdi *et al.* (2011). These are the most commonly used formulas as they get rid of the space and time derivations. The dual version for motionless sources in an uniformly moving flow was described by Wells and Han (1995). Ultimately, the optimized formulation of (1.4.1) referred to as *1C* in the literature reads as follows:

$$p(\boldsymbol{r},\omega) = p_L(\boldsymbol{r},\omega) + p_T(\boldsymbol{r},\omega) \tag{1.4.3}$$

where

$$\begin{aligned} p_L(\boldsymbol{r},\omega) &= \int_\Gamma \boldsymbol{L}_x \boldsymbol{n}_x(\boldsymbol{r}_s) \left[\mathrm{i}k\boldsymbol{R}_x + \frac{\boldsymbol{R}_x^*}{R^*} \right] \frac{e^{\mathrm{i}kR}}{4\pi R^*} \mathrm{d}\Gamma(\boldsymbol{r}_s), \\ p_T(\boldsymbol{r},\omega) &= -\int_\Gamma Q \left[\mathrm{i}\omega(1-\boldsymbol{R}_x M_0) - U_0 \frac{\boldsymbol{R}_x^*}{R^*} \right] \frac{e^{\mathrm{i}kR}}{4\pi R^*} \mathrm{d}\Gamma(\boldsymbol{r}_s), \end{aligned} \tag{1.4.4}$$

and

$$\begin{aligned} \delta\boldsymbol{r} &= \boldsymbol{r}_s - \boldsymbol{r}, \quad \delta r = \|\delta\boldsymbol{r}\|, \quad \beta^2 = \left(1 - M_0^2\right), \\ \boldsymbol{R} &= \frac{1}{\beta^2}\left(\boldsymbol{R}^* - \boldsymbol{M}_0 \cdot \delta\boldsymbol{r}\right), \quad R = \|\boldsymbol{R}\| \\ \boldsymbol{R}^* &= \delta\boldsymbol{r}\beta\sqrt{1 + \beta^2 \boldsymbol{M}_0 \cdot \delta\boldsymbol{r}}, \quad R^* = \left\|\boldsymbol{R}^*\right\|. \end{aligned} \tag{1.4.5}$$

1.4.2 CFD and acoustic imaging

As exposed in section 1.3.1, the core principle of analogies shares with acoustic imaging methods the underlying idea to boil down the measured sound to the one radiated by elementary acoustic sources, with the difference that sources are considered continuously distributed in the formulation of analogies. From then on, a logic step was to link up the two domains and introduce transfer functions that are inspired from FW-H in the inverse problem of source identification. It led to a large collection of publications in aeroacoustic imaging based on convected monopoles and dipoles (see for example Liu *et al.*, 2008; Leclère *et al.*, 2020). Concerning the second integral in Eq.(1.4.3), Papamoschou and Mayoral (2013) proposed a clear statement of convected models and emphasized the subtle distinction between convected sources and convected Green functions. He showed that the transfer function defined as

$$\boldsymbol{H}_{i,j} = \frac{e^{\mathrm{i}kR}}{4\pi R^*} \tag{1.4.6}$$

(with R and R^* taken from Eq.(1.4.5) with $\delta\boldsymbol{r} = \boldsymbol{r}_j - \boldsymbol{r}_i$) was relevant even though suitable for the identification of pressure point sources more than monopoles. It is

illustrated on Fig-1.12.

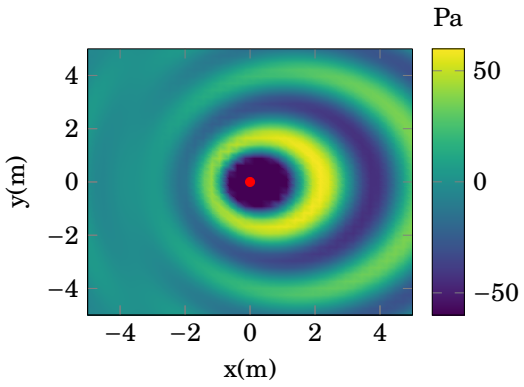

FIGURE 1.12 - *Acoustic pressure (real part) of a thickness noise source at $f = 100$ Hz and $\boldsymbol{M}_0 = (-0.2, 0., 0.)$. The red dot indicates the source position.*

To extend the range of acoustic imaging to the identification of loading noise dipolar sources, the straightforward idea is then to fuel the classical inversion algorithms from section 1.2 with dipolar directivities. Bearing in mind the *structure reaction* in the interpretation of the loading noise source, Evans *et al.* (2019) therefore proposed to use the structure normal components $\boldsymbol{n}$ as $\boldsymbol{d}$ in Eq.(1.3.3) to model the first integral in Eq.(1.4.3) with accurate results. The approaches mentioned in section 1.3.1 notably pertain to this scope.

When it comes to perform acoustic imaging on simulated fluid dynamic data, two different schemes can be found in the literature:

- The first and intuitive one consists in the use of a Direct Numerical Simulation (or alternatives) for the resolution of the Navier-Stokes in the source region Ω_s. From this is sampled the compressible pressure, then propagated toward a virtual array in the far field using analogies.

- Adam *et al.* (2007) then Pignier *et al.* (2016) investigated the option of having the microphonic pressures directly inside the CFD domain with compressible solvers. Named Direct Numerical Beamforming, this technique definitely parts with practical acoustic imaging : according to the authors, its aims at using large numbers of microphones very close to the sources region to assume it as uncorrelated and suitable with CBF (which remains a questionable point). The use of three-dimensional FRFs capable of accounting for dipolar directivities or diffraction remains a blind spot of this approach as well.

1.5 Conclusion

This chapter surveys a literature review on the acoustic imaging problem, purposely oriented toward the issues that arised with increasing interest for three-dimensional source identification in complex environments. Over the last decades, the span of algorithms assessed for the inversion of a propagation model to fetch acoustic sources from multi-sensor arrays became vast. Through the chosen examples presented in the previous pages it was underlined that they now cover many possibilites in terms on source assumption, from sparse and uncorrelated with beamforming and deconvolution to extended and fully correlated with inverse methods and regularization.

However, the conclusion differs when the stake shifts to the use of a realistic propagation model between potential sources and microphone arrays. Simple source models like multipoles propagating in free field stick around as the robust and easy to implement option, but it also lacks precision when acoustic paths are hampered by scattering components. Other analytical options are available but limited to basic geometries, and the only avenue for improvement on transfer models is numerical simulation.

From that perspective, BEM was already tested on various cases showing good results at the cost of consequent computational ressources. Based on this state of the art, the work presented in this thesis positions itself as an investigation of the use of equivalent sources to construct FRFs. The next chapter delves into the ESM process as introduced by Koopmann *et al.* (1989) for that purpose, and features the modifications and settings added to it for the industrial applications.

CHAPTER 2

EQUIVALENT SOURCES FOR TRANSFER FUNCTION SIMULATION

First introduced by Koopmann *et al.* (1989), the Equivalent Source Method (ESM) as it is currently stated in the literature (see Lee, 2017) enters the scope of simulated refined FRFs presented in section 1.3.3.2. This chapter starts with some literature clarification concerning equivalent sources in acoustic imaging. Then ESM is depicted from both the theoretical and practical point of views, and finally are laid down the contributions of this PhD with parametric studies and declensions of the method to realistic set-ups.

Computer resources

Every results presented in the last 3 chapters were obtained using sequential PYTHON 3 on a laptop, fitted with an INTEL CORE I7 8750H (2.2 Ghz).

2.1 The use of ESM terminology for acoustic imaging

The bibliographic review in chapter 1 pointed out that the Equivalent Source Method denomination in the literature was associated to a large panel of appli-

cations. Notably, a substantial distinction should be drawn between equivalent sources used for imaging purposes and ESM as simulation algorithms.

Historically, Koopmann *et al.* (1989) designed and assessed the ESM as more simple and flexible alternative to BEM for more simple test cases. Its physical principle can be stated concisely : considering a rigid body exposed to an incident acoustic field, a volume interior distribution of elementary sources can be set to offset the boundary condition induced by the incident field on the skin of the object. The main interest of having equivalent sources strictly in the interior domain is to avoid numerical singularities issues encountered with BEM. These sources are thus considered as acoustically equivalent to the presence of the rigid body, and can be propagated toward the domain outside the skin to get the scattered sound field. After describing the theoretical background of ESM, Koopmann *et al.* (1989) also established its numerical version in which the rigid body and the volume of equivalent sources are respectively modeled by a rudimentary mesh and a discrete set of acoustic monopoles.

The generic set-up common to all acoustic imaging problems, described with Eq.(1.1.1) and Fig-1.1, can be cast in ESM problems: it aims at identifying a set of sources acoustically *equivalent* to those that actually produced the sound field covered by the microphone array. When it comes to acoustic imaging, the ESM terminology was used for instance by Fernandez-Grande *et al.* (2017); Hald (2020); Sarkissian (2005); Valdivia and Williams (2007) for applications in near-field acoustic holography, by Leclère *et al.* (2017) for inverse methods or Pereira (2013, Chapter 2) for imaging in enclosed space. If they differ in the algorithm used to identify the sources, the common ground to all these references lies in their use of a discrete set of equivalent monopoles (or dipoles, see for example Valdivia, 2018) to reconstruct a radiated acoustic field from array measurements. However, another common aspect is that they no more involve these equivalent sources in the simulation of a particular boundary condition in contrast to the historical purpose of ESM. Regarding now this chapter, the proposed ESM technique does not pertain to this specific scope but to the one of Koopman: Chapter 2 is about an implementation of FRF simulation upstream to acoustic imaging.

2.2 ESM process

2.2.1 Principle and theoretical statement

The ESM was originally designed to compete with Boundary Element Method (BEM) for the synthesis of acoustic fields scattered by arbitrarily shaped surfaces (see Lee, 2017; Pavić, 2005). It lies on the equivalence between the Kirchhoff-Helmholtz integral formulation and the wave superposition volumetric formulation (Schenck, 1968; Butler, 1970): as the former states that the knowledge of the pressure p and particle velocity $\boldsymbol{v}$ on the skin is sufficient to estimate the whole acoustic field, the latter achieve the same with continuous enclosed sources satisfying the impedance boundary condition on the skin of the radiator.

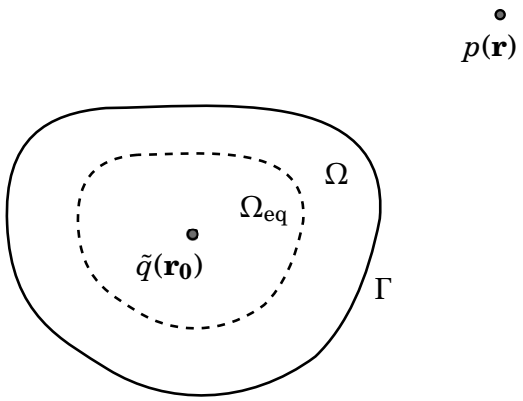

FIGURE 2.1 - *Wave superposition method : The integration of volume sources inside Ω_{eq} is strictly equivalent to the Kirchhoff-Helmholtz integration on Γ and Ω for the reconstruction of $p(\mathbf{r})$*

With the notation of Fig-2.1, the Kirchhoff-Helmholtz formulation indicates

$$p(\mathbf{r}) = \int_{\Gamma} \left(p(\boldsymbol{r}_s) \frac{\partial G(\boldsymbol{r}, \boldsymbol{r}_s)}{\partial n} + \mathrm{i}\omega\rho \boldsymbol{v}_n G(\boldsymbol{r}, \boldsymbol{r}_s) \right) \mathrm{d}\Gamma(\boldsymbol{r}_s), \tag{2.2.1}$$

while the equivalent wave superposition method may be written as

$$p(\boldsymbol{r}) = \mathrm{i}\omega\rho \int_{\Omega_{\text{eq}}} \tilde{q}(\boldsymbol{r}_0) G(\boldsymbol{r}, \boldsymbol{r}_0) \mathrm{d}\Omega(\boldsymbol{r}_0) \tag{2.2.2}$$

conditionally upon $\tilde{q}$ satisfying

$$\forall \boldsymbol{r}_s \in \Gamma, \quad \boldsymbol{v}_n(\boldsymbol{r}_s) = \int_{\Omega_{\text{eq}}} \tilde{q}(\boldsymbol{r}_0) \frac{\partial G(\boldsymbol{r}_s, \boldsymbol{r}_0)}{\partial n} \mathrm{d}\Omega(\boldsymbol{r}_0). \tag{2.2.3}$$

2.2.1.1 Implementation

The transition from the integral formulation above to its numerical approximation was first proposed by Koopmann *et al.* (1989, section I.B). Since the boundary condition on Γ satisfied by $\tilde{q}$ in Eq.(2.2.3) does not depend on the geometry of Ω_{eq}, the latter was first defined as an arbitrarily thin shell and discretized into point sources. The line of argument here is rather direct and may be questioned as we will see later in this section. The practical development unfolds as followed: considering a scattering object, N_s equivalent sources of volume flows $(\tilde{q}_l)_{l\leq N_s}$ are firstly placed inside its boundary Γ. This set of sources is then configured to meet the boundary condition on Γ as in Eq.(2.2.3) on N control points so that their combined contributions could be considered as *equivalent* to the real presence of the object. The amount of equivalent sources is a key parameter of the method, and its ratio to the number of control points is noted $\eta = \frac{N_s}{N}$ in this thesis. In the rest of the document, a Neumann boundary condition is chosen as an boundary condition example for the sake of clarity.

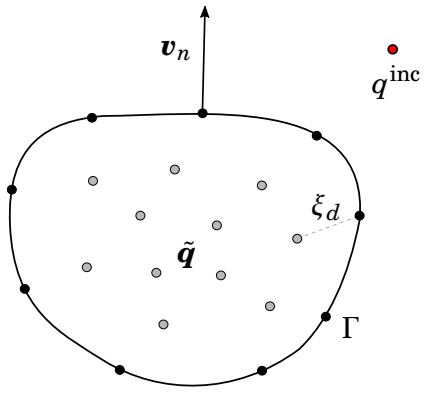

FIGURE 2.2 - *ESM schematic set-up. Equivalent sources $(\tilde{q}_l)_{l\leq N_s}$ (in grey) are adjusted to counter balance the normal velocity induced by a unitary source q^{inc} at every control points on Γ.*

The calibration of equivalent sources placed inside the scattering object basically pertains to an inverse problem. Their primary role is to offset the incident normal velocity to ensure the boundary condition. Considering the FRF simulation context, a first relevant example is to consider the incident field generated by an unitary monopole q^{inc} typically located at a microphone position with respect to the set-up presented in Fig-1.1. The compensating sources $(\tilde{q}_l)_{l\leq N_s}$ are thus

mathematically established by

$$\text{Find} \quad \tilde{\boldsymbol{q}} \in \mathbb{C}^{N_s} \quad \text{that satisfies} \quad \boldsymbol{v}_n^i = -\boldsymbol{T}\tilde{\boldsymbol{q}}. \tag{2.2.4}$$

$\boldsymbol{v}_n^i \in \mathbb{C}^N$ denotes here the normal velocity induced by q^{inc} at each control points. Noting $\boldsymbol{r}_i$ the position of q^{inc}, θ_{ji} the angle between $\boldsymbol{r}_j - \boldsymbol{r}_i$ and the normal to Γ at the j^{th} control point, it reads as $\forall j \leq N$

$$\boldsymbol{v}_{n,j}^i = \frac{e^{\mathrm{i}kr_{ji}}}{4\pi r_{ji}^2}(1 - \mathrm{i}kr_{ji})\cos\theta_{ji} \tag{2.2.5}$$

considering a monopolar incident source as q^{inc}.

Similarly, $\boldsymbol{T} \in \mathbb{C}^{N \times N_s}$ emphasizes the transfer between the equivalent sources volume flows and the corresponding normal velocities on the skin: $\forall j \leq N, \quad \forall l \leq N_s$,

$$\boldsymbol{T}_{j,l} = \frac{e^{\mathrm{i}kr_{jl}}}{4\pi r_{jl}^2}(1 - \mathrm{i}kr_{jl})\cos\theta_{jl}. \tag{2.2.6}$$

Once Eq.(2.2.4) is solved, the last step is to re-propagate the equivalent sources towards any point of interest to get the radiated pressure field :

$$p(\boldsymbol{r}) = \underbrace{\boldsymbol{G}\tilde{\boldsymbol{q}}}_{\text{scattered pressure}} + \underbrace{\boldsymbol{G}q^{\text{inc}}}_{\text{incident pressure}}, \tag{2.2.7}$$

using a the monopolar volume flow to pressure transfer function

$$\forall j \leq N, \quad \forall l \leq N_s, \quad \boldsymbol{G}_{jl} = -\mathrm{i}\omega\rho G\left(\boldsymbol{r}_j, \boldsymbol{r}_l\right). \tag{2.2.8}$$

Contrary to the initial inverse problem of acoustic imaging of section 1.1, the ESM inverse problem is purely numerical and does not involve measured data. It is thus worth using simple methods that provides the least square solution of the problem, and no sparse inducing penalties or advanced regularization step are required. The most intuitive approach is to compute $\boldsymbol{T}^+$, the pseudo inverse of $\boldsymbol{T}$. Considering the Singular Value Decomposition (SVD)

$$\boldsymbol{T} = \boldsymbol{P}\boldsymbol{\Sigma}\boldsymbol{Q}^{\mathsf{H}}, \quad \boldsymbol{P} \in \mathscr{O}_N(\mathbb{C}), \quad \boldsymbol{Q} \in \mathscr{O}_{N_s}(\mathbb{C}) \tag{2.2.9}$$

with $\boldsymbol{\Sigma}$ containing the singular values on its diagonal and zeros everywhere else,

the pseudo inverse is defined as

$$\boldsymbol{T}^{+} = \boldsymbol{Q}\boldsymbol{\Sigma}^{-1}\boldsymbol{P}^{\mathrm{H}} \tag{2.2.10}$$

With $\boldsymbol{\Sigma}^{-1}$ denoting here a diagonal matrix in $\mathbb{C}^{N_s \times N}$ filled with the inverted coefficients of Σ. It provides the source distribution that satisfies Eq.(2.2.4) with minimum energy. It may also be noticed the complexity of the SVD computation algorithm reaches $O(N^2 N_s)$ and the pseudo inversion rapidly represents the most costly step of the ESM process for large scale structures at high frequencies. For the purpose of computing the transfer functions between M microphone position and a mesh, M different equivalent sources sets have to be computed, each one being tailored to match with the incident field stemming from one microphone position. Within this context, the numerical view of ESM is summarized in table 2.1.

ESM stage	**Operations**
Incident field - Eq.(2.2.5)	MN
$\boldsymbol{T}$ computation - Eq.(2.2.6)	NN_s
$\boldsymbol{G}$ computation	$N(N_s + M)$
$\boldsymbol{T}$ pseudo inversion - Eq.(2.2.9)	$O(N^2 N_s)$
Final Backpropagation - Eq.(2.2.7)	NN_s

TABLE 2.1 - *FRF simulation through ESM numerical costs, considering M microphones, N grid points and N_s equivalent sources.*

2.2.1.2 ESM in the Boundary Element Method framework

In order to nail the ESM benefits and limits, it is of interest to discuss it further with the vocabulary dedicated to the boundary integrals background. In particular, the integral formulation Eq.(2.2.1) of the wave equation is often spoken in terms of *single and double layer potentials* (see for example Bonnet, 1999; Chandler-Wilde and Langdon, 2007) respectively defined as

$$\mathscr{S} : u(\cdot) \mapsto \int_{\Gamma} u(\mathbf{r}_s) G(\cdot, \mathbf{r}_s) \mathrm{d}\Gamma(\mathbf{r}_s) \tag{2.2.11}$$

and

$$\mathscr{D} : u(\cdot) \mapsto \int_{\Gamma} u(\mathbf{r}_s) \frac{\partial G(\cdot, \mathbf{r}_s)}{\partial n} \mathrm{d}\Gamma(\mathbf{r}_s). \tag{2.2.12}$$

From that starting point, a well known result is that the radiated pressure field can be sought as

$$p(\mathbf{r}) = \mathscr{S}\lambda(\mathbf{r}) - \mathscr{D}\mu(\mathbf{r}) \tag{2.2.13}$$

where λ and μ are the discontinuity functions

$$\mu = (p^{\text{int}} - p)|_{\Gamma} \quad \text{and} \quad \lambda = \left(\frac{\partial p^{\text{int}}}{\partial n} - \frac{\partial p}{\partial n}\right)\Big|_{\Gamma}. \tag{2.2.14}$$

p^{int} stands here for an arbitrary chosen prolongation of p inside Γ. On the choice of this prolongation will unfold a relationship between λ and μ (see for example Burton and Miller (1971) for an overview of commonly used prolongation choices or Alouges *et al.* (2017, section 2) for an application example). This relationship is then introduced in ∂_n of Eq.(2.2.13) evaluated on Γ, and leads to the boundary integral equation that needs to be reversed to finally compute p everywhere outside the radiating surface.

Without going further into details, the boundary elements method refers to the numerical resolution of this inversion by means of an quadrature integration rule to approximate the single and double layer potentials on a discretized Γ (in the form of *boundary elements*).

From that perspective, Wilton *et al.* (1993) proposed a valuable interpretation of the wave superposition method in this framework. First the wave superposition in Eq.(2.2.2) can be considered as an alternative formulation of Eq.(2.2.13) without double layer potential and evaluated on an enclosed surface Γ_{eq}. The acoustic field produced by the equivalent sources may then be understood as a particular choice of the prolongation p^{int}, that notably implies the continuity of the pressure field on Γ or equivalently $\mu \equiv 0$. At last the assessment of Eq.(2.2.3) would correspond with the boundary integral equation.

Crossing various applications of the method available in the literature, it is possible to give an overview of the practical consequences of this analogy:

- Leblanc *et al.* (2010) and Kondapalli *et al.* (1992) stated the choice in the location of the equivalent sources offers a great flexibility to avoid the non uniqueness issues that boundary element methods suffer at particular eigen frequencies. The straightforward counterpart for this is that their optimal positioning is likely to be geometry and frequency dependent and remains an open-ended question.

- Since point sources are considered, ESM is a *quasi-meshless* process and

bypasses the potentially high order numerical integration on boundary elements. As demonstrated by Valdivia and Williams (2007), the firm grasp of $\mathbf{G}$ and $\nabla\mathbf{G}$ assembling step is more accessible than the boundary element method integral operators and the coding effort is considerably reduced.

- Providing an appropriate equivalent sources distribution, it is often possible to consider fewer equivalent sources than control points thus often turns out to be an overdetermined problem which numerical complexity is upper bounded by the lowest possible boundary elements method matrix size corresponding to a zero order surface integration.

- Koopmann and Fahnline (1991) or Lee (2017) highlighted that the boundary elements method are prone to instabilities when Eq.(2.2.13) is evaluated in the vicinity of Γ due to the Green function singularity. As the equivalent sources are strictly enclosed inside the skin, ESM is normally not concerned by such issues and consequently suitable when the surface pressure on Γ is of interest.

All these assets come at the cost of a coarser approximation of the reconstructed acoustic field when the incident acoustic field and the geometry are complex and requires high order basis function for an accurate boundary integral quadrature.

2.2.2 Validation for FRF simulation

ESM as presented so far can be operated for the construction of $\boldsymbol{H}$ and enters the approaches listed in section 1.3. This section features the assessment of ESM accuracy for such a purpose, tackled from the various parameters evoked before.

2.2.2.1 Reciprocity principle

The problem of FRF construction seemingly falls into the scope of the reciprocity principle established for various types of sources (see Pierce, 1981; Samarasinghe *et al.*, 2017). Instead of identifying the pressure at the antenna given acoustic sources on the object, the FRF may also be understood as the ratio between the volume flow of a source placed on a microphone position and the pressure taken on the skin of the object :

$$\forall \boldsymbol{r}_0 \in \Gamma, \quad \forall \boldsymbol{r} \in \bar{\Omega}, \quad G(\boldsymbol{r}_0, \boldsymbol{r}) = G(\boldsymbol{r}, \boldsymbol{r}_0). \tag{2.2.15}$$

With respect to Eq.(1.3.1), this boils down to determine the transpose $\boldsymbol{H}^{\top}$ instead of the genuine transfer function and use its conjugate $\boldsymbol{H}^{\mathrm{H}}$ to account for the reversed propagation. The reciprocal approach paves the way for numerical simulations methods allowing the computation of the acoustic field of a source scattered by the object, and ESM benefits from it by avoiding singularity issues: when solving Eq.(2.2.5) it is more sustainable to have q^{inc} propagating from location far from boundary condition support. In other words, dealing with incident sources at the microphone positions is more careful than having it on the skin.

2.2.2.2 SRTF comparison

Highlighted in section 1.3.2 as an analytic transfer function describing scattering around a sphere, the SRTF is used in this section as a validation case. Considering the set-up of Fig-2.3, the transfer function between two different control points and one microphone is computed using the ESM process as presented previously.

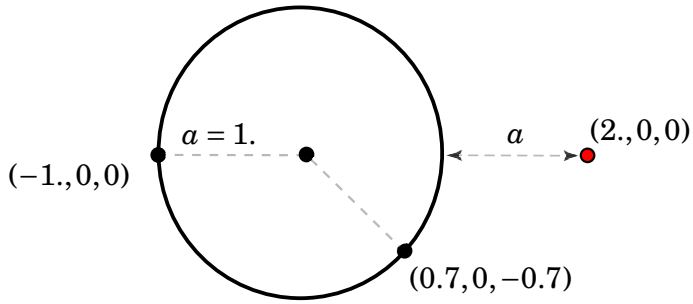

FIGURE 2.3 - *Geometric values chosen for the SRTF validation. The first control point under scrutiny is located on the opposite to the microphone (in red) for the diffraction to be significant, while the second one it more similar to a free field propagation.*

Transfer functions are computed up to 5 kHz so that the frequency limitation due to the number of control points on the sphere could be observed. Following the recommendation stated in Eq.(1.3.10), spherical harmonics are truncated at the 40^{th} order. For this first test, $N = 1000$ control points a regularly placed on the sphere following a Fibonacci lattice, and $N_s = 500$ equivalent sources ($\eta = 0.5$) are used.

Figures 2.4 and 2.5 display side-by-side the acoustic FRFs between points on the sphere and the arbitrary located microphone in red on Fig-2.3 on the 100 to 3000 Hz frequency range (i.e. $ka \in [0.5, 17]$). It substantiates the ability of ESM to accurately model a simple acoustic transfer up to a certain frequency limit. No

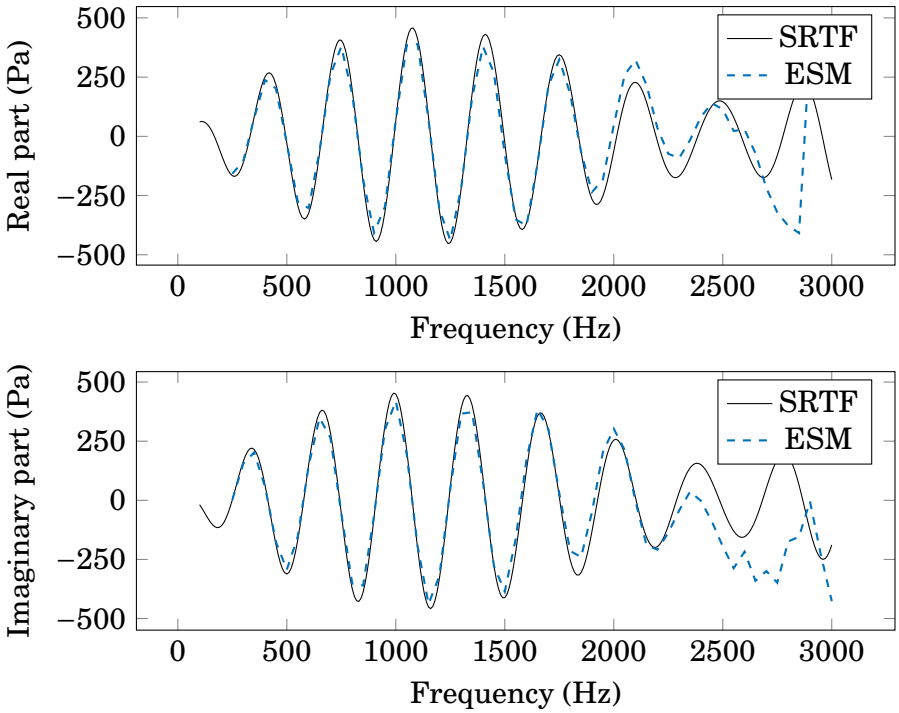

FIGURE 2.4 - *Comparison of ESM with analytical SRTF results on the (-0.25,0,0) position.*

assessed demonstration of this frequency limit exist in the literature, the latter seems to depend on the geometry of the test and every application of ESM comes with its empirical statement on the maximum frequency range (see Lee, 2017, for an overview). The one used during the PhD is exposed in section 2.2.3 dedicated to the parametric study of ESM.

On Fig-2.6 is illustrated the concept of computing successively $\boldsymbol{G}\tilde{\boldsymbol{q}}$ and $\boldsymbol{G}q^{\text{inc}}$ with the display of the incident and scattered fields on the spherical case at a given frequency, echoing these two terms in Eq.(2.2.7). The equivalent sources generate an acoustic field offsetting the incident one on Γ and their combination yields exactly the pressure field scattered by the sphere exhibited analytically on Fig-1.7.

2.2.3 Parametric study

As mentioned in section 2.2, ESM proved out to be a highly efficient algorithm. However, its accuracy is highly dependant on the input parameters related to the equivalent sources that, i.e. their number and positions. This section discusses the contributions of the PhD to this path of research that is hardly tackled in the literature.

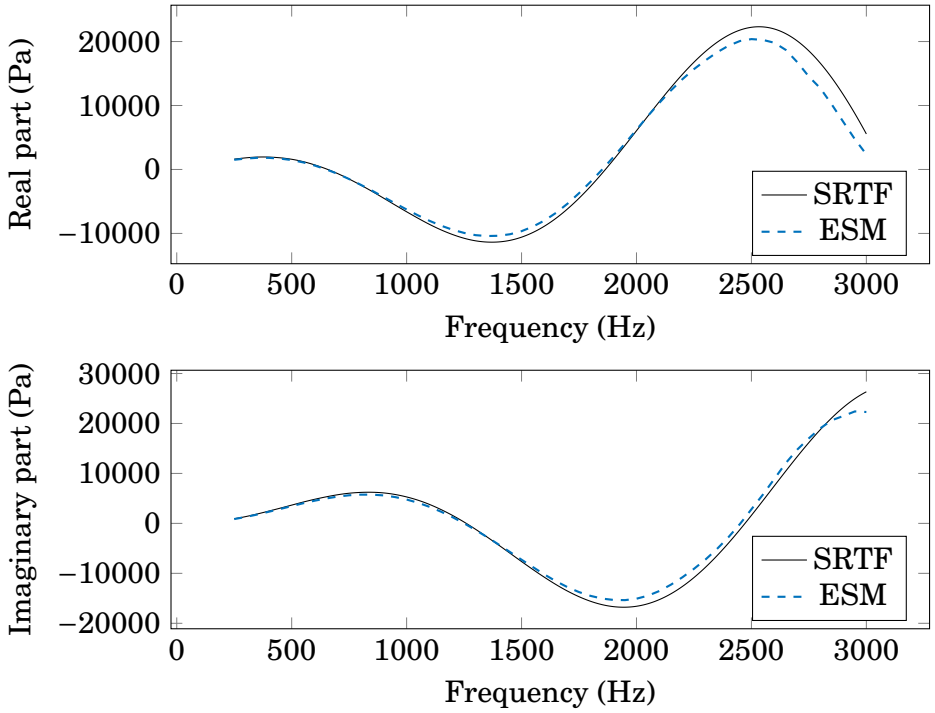

FIGURE 2.5 - *Comparison of ESM with analytical SRTF results on the (-0.17,0.17,0) position.*

For the assessment of ESM accuracy, SRTF stands for a reference and an L^2 error indicator is defined as

$$\varepsilon = \frac{\left\| \boldsymbol{H}^{\mathrm{ESM}} - \boldsymbol{H}^{\mathrm{SRTF}} \right\|^2}{\left\| \mathbf{H}^{\mathrm{SRTF}} \right\|^2}, \tag{2.2.16}$$

corresponding to the L^2 relative error on the FRFs averaged on every control points. Besides are evaluated the sensitivity to the condition number of $\boldsymbol{T}$, conventionaly given by the ratio κ of the utmost singular values $\sigma_{\max}$ and $\sigma_{\min}$. The SVD in Eq.(2.2.10) is indeed responsible for both the ESM limitations : if the conditioning number is high due to small singular values, $\boldsymbol{\Sigma}^{-1}$ will be filled with extremely high entries and thus amplify any numerical approximation made on the model. In that case, the commonly used solution is to cut off the inverse of the smallest singular values and trade accuracy for numerical stability.

2.2.3.1 Positions of the equivalent sources

As the monopole formula presents a singularity at the origin, precautions must be taken to avoid unmanageable entries in $\boldsymbol{T}$. The minimum distance between sources and control points, called the *retreat distance* (see Bai *et al.*, 2011) noted

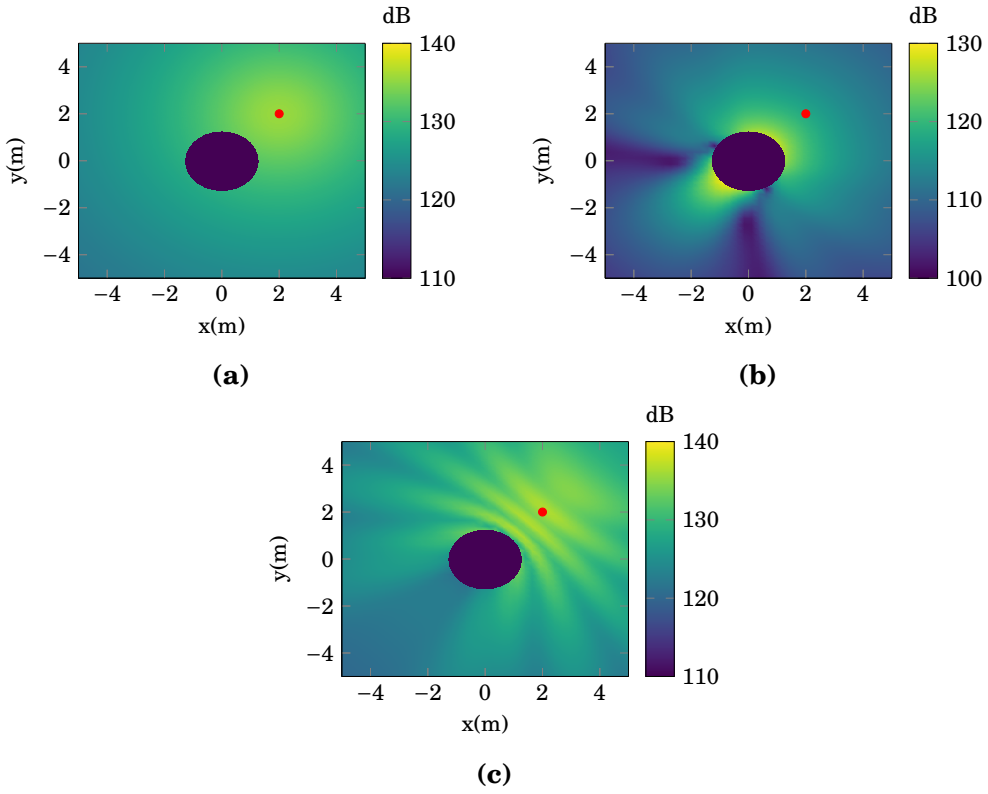

FIGURE 2.6 - *Acoustic pressure (amplitude) of (a) the incident field produced by a monopole (red dot); (b) the radiated field emitted by the equivalent sources; (c) the complete field, at* $ka = 2.1$.

as ξ_d on Fig-2.2, is a tricky question: if ξ_d is close to zero, propagation matrices are not numerically stable. If however ξ_d is chosen too large, all the equivalent sources are very close from one another and $\boldsymbol{T}$ becomes ill-conditioned. Noteworthy is that no clear answers are given in the literature except on a case-by-case basis.

A common solution is to consider a scaled replica of the object surface (Dunn and Tinetti, 2004), but arranging them as a random cloud of points also yields encouraging results. The latter approach sometimes labelled as the Method of Fundamental Solution aims at preventing the equivalent sources to be located on nodal lines. Here lies a critical advantage of ESM over boundary elements method as random equivalent sources distribution allows to avoid the non-uniqueness issues similar to those observed using (Chen, 2006; Kondapalli *et al.*, 1992). Leblanc *et al.* (2010) proposed a dual version with both randomly chosen and replicated equivalent sources to reach an acceptable conditioning number for $\boldsymbol{T}$ without sacrificing its geometrical adequacy with the rigid surface.

A more sophisticated approach exposed by Pavić (2005) and Le Magueresse (2016, chapter 3) pertains to the optimal selection of a reduced number of equivalent sources using an iterative greedy algorithm to solve Eq.(2.2.4). It provided impressive results on both analytical and experimental test cases, but also turned to be drastically time consuming and probably unsuitable for large scale models.

The random positioning approach is tested and illustrated on Fig-2.7 on the spherical test case, with the set-up previously used for Fig-2.4. As expected, κ is improved when the source distribution matches the best with Γ, until it becomes too close and the $1/r$ singularity prevails. Nevertheless, the best overall performance occurred with the randomly placed sources. Based on this outcome, a routine allowing to generate a random cloud of points inside a triangular mesh is presented in Appendix A. These plots also highlight that the retreat distance can be set quite large without any loss of precision.

Since equivalent sources are selected randomly, one must assess the stability of ESM with respect to the random seed. This can be achieved by launching the source generation routine a large amount of times and check the ability of the resulting equivalent sources to compensate the incident velocity field. This is achieved again with an L^2 indicator on the residual normal velocity on Γ:

$$\varepsilon^v = \frac{\left\| \boldsymbol{v}_n^{\text{inc}} - (-\boldsymbol{T}\tilde{\boldsymbol{q}}) \right\|^2}{\left\| \boldsymbol{v}_n^{\text{inc}} \right\|^2}. \tag{2.2.17}$$

The latter was computed for a monopole incident source at several frequencies

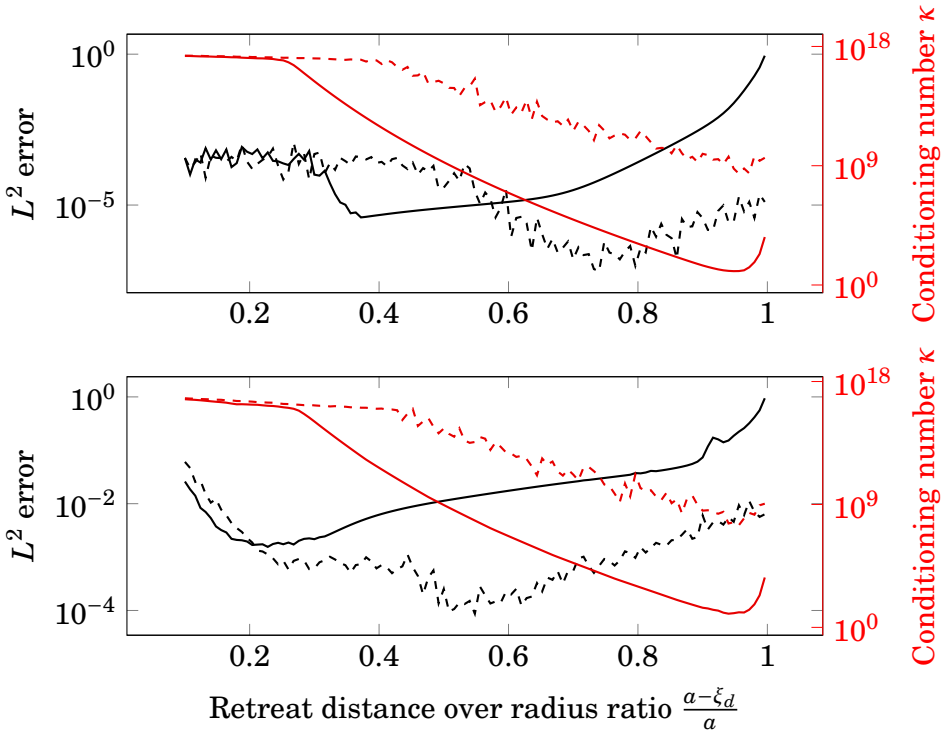

FIGURE 2.7 - *ESM sensitivity to the retreat distance at $ka = 2.2$ (top) and $ka = 11.2$ (bottom). In black is plotted the L^2 error on the SRTF reconstruction, in red the conditioning number of $\boldsymbol{T}$, and dashed lines were obtained with random equivalent source positions while plain lines with a scaled replica of the sphere.*

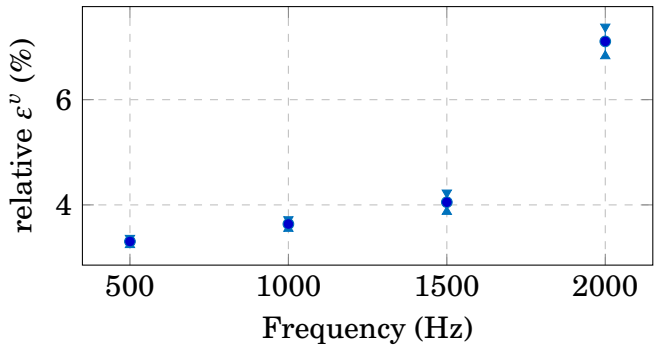

FIGURE 2.8 - *Mean value (dark blue dot) ± the standard deviation (sky blue arrows) of the ε^v indicator.*

on the spherical case: the result on Fig-2.8 clearly indicate that ESM is robust given the low variance of ε^v regarding the source distribution sampled from the random process.

2.2.3.2 Number of the equivalent sources

The optimal number of equivalent sources is an unresolved problem. A balance has to be found between too few sources unable to describe the complex scattered field of the object and a too high density of sources worsening the conditioning of the problem. This number is commonly set proportional to the number of control points to remain consistent with the frequency range of interest. In the framework of thin aeroacoustic profiles, Dunn and Tinetti (2004) pointed out experimentally that a ratio $\eta = N_s/N$ equal to 0.33 (i.e. three times less sources than control points) was optimal for their applications. To enforce stability for simple geometries, one could also mention the possibility of setting a highly overdetermined ratio $\eta \approx 0.1$ coupled with a regularized resolution of Eq.(2.2.4) as demonstrated by Lam *et al.* (2015).

2.3 Dipolar ESM

In accordance with aeroacoustic analogies, the noise arising from the interaction of an object and a low Mach number flow is likely to be accurately described by the radiation of elementary dipoles. Combined with the diffracting behaviour of a rigid body, three-dimensional source identification in wind tunnel is thus prone to sketchy or misleading interpretations when only free field monopolar steering vectors are used.

As mentioned in section 1.4.2, Evans *et al.* (2019) designed a half dipole formulation to filter the dipole directivity that would propagated through the scattering body. This approximation stands as a simple and robust approach to include the rigid behaviour of the body in the propagation model:

$$\boldsymbol{H}_{i,j} = \begin{cases} A_j \frac{e^{\mathrm{i}kr_{ij}}}{4\pi r_{ij}^2}(1-\mathrm{i}kr_{ij})\,\boldsymbol{r}_{ij}\cdot\boldsymbol{n}_j & \text{if} \quad \boldsymbol{r}_{ij}\cdot\boldsymbol{n}_j > 0 \\ 0 & \text{if} \quad \boldsymbol{r}_{ij}\cdot\boldsymbol{n}_j < 0, \end{cases} \tag{2.3.1}$$

Here the condition related to the incident angle serves as a filter to remove microphones located in the blind spot of the dipole: without it, any small coherent signal leads to largely overestimated sources because of the transfer function tending to-

ward zero. The purpose of this section is to address the few adjustments due to this change of incident source models, in view of aeroacoustic application cases.

2.3.1 ESM steps update

With respect to section 2.2.1.1, some major modifications are to be taken into consideration. First of all, the computation of the incident normal velocity profile is no longer independant from the grid point on Γ of which the FRF is sought. As exposed on Fig-2.9, reciprocity still works but it requires a different computation of $\boldsymbol{v}_n^i$ for each node of the mesh since each node is associated to its own directivity $\boldsymbol{n}$ as a potential dipole source. This reads in practical as a modification of Eq.(2.2.5) as

$$\forall j \leq N, \quad \boldsymbol{v}_{n,j}^{i,m} = A_m \frac{e^{\mathrm{i}kr_{ji}}}{4\pi r_{ji}^3} \left[\begin{array}{c} \left((k^2 r_{ji}^2 - 2\mathrm{i}kr_{ji} + 2 \right) \boldsymbol{r}_{ji} \cdot \boldsymbol{n}_m \\ \mathrm{i}kr_{ji} + 1 \end{array} \right] \cdot \boldsymbol{n}_j. \tag{2.3.2}$$

Notably, the new dependency on the m index implies an significant increase of the computational cost.

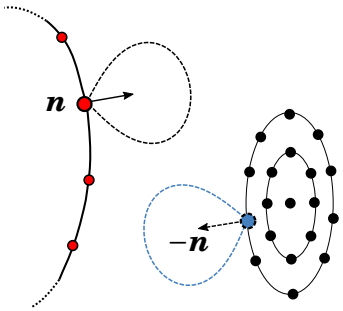

FIGURE 2.9 - *Reciprocity principle applied to dipolar FRFs. The computation of a half dipole on the mesh radiating toward a microphone can be traded against the one of a dipole with opposite direction located on the array toward the surface.*

The costliest step from that perspective remains the pseudo inversion of $\boldsymbol{T}$, but added to it has to be considered the loop on every node on the mesh to compute the incident velocity vector. This step is more demanding with dipoles because of the m dependency in Eq.(2.3.2) (which cannot be vectorized anymore). The overall cost remains in $\mathcal{O}(N_s N^2)$, but dipolar ESM features double the number of operations as monopolar ESM. In practical The latter issue is a current drawback of dipolar ESM, partly tackled during the thesis by grouping the computation of Eq.(2.3.2) for each flat parts of the boundary Γ where the orientation $\boldsymbol{n}_m$ remains constant.

Ultimately, the spatial filter from Eq.(2.3.1) is applied. The Point Spread Function (PSF) of a dipole scattered by a rigid sphere with respect to a $M = 300$ spherical array is displayed on Fig-2.10.

(a) **(b)**

FIGURE 2.10 - *Scattered dipole PSF at $ka = 22$, the red dot indicates the ground truth position of the source and the black ones refers to the microphone array; (a) Unfiltered; (b) Filtered with Evans et al. (2019) process depicted in Eq.(2.3.1).*

2.3.2 SVD truncation with Picard plots

The truncation of low singular values when computing $\boldsymbol{T}^+$ through Eq.(2.2.10) has to be carefully tuned. For that purpose, Hansen (1990) proposed a criterion named *discrete Picard condition*. Its underlying concept is to somehow check the adequacy between the boundary condition and the volumic flow to normal velocity propagator. The associated formalism with the notation of this thesis boils down to ensure that the incident vector $\boldsymbol{v}_n$ does not have coefficient carrying numerical noise correlated with $\boldsymbol{T}$ smallest singular values. Hansen (1990) demonstrated that this was equivalent to check that these singular values $(\sigma_l)_{l\in N_s}$ decrease slower with l than $|\boldsymbol{P}_l \cdot \boldsymbol{v}_n|$, $\boldsymbol{P}$ being defined in Eq.(2.2.9) as the orthogonal matrix from $\boldsymbol{T}_\Gamma$ SVD.

This simple approach was the one used for the monopolar ESM examples in the previous section, as it allows to rapidly fix the threshold under which singular values in $\boldsymbol{\Sigma}$ must be removed to keep the ESM inverse problem stable.

From the Picard plots illustrated in Fig-2.11 it can be stated that influence on the numerical behaviour of ESM of dealing with dipole-issued incident velocity fields does not differ much from the monopolar one, as the slope of the blue and green lines that determines the SVD truncation is unchanged.

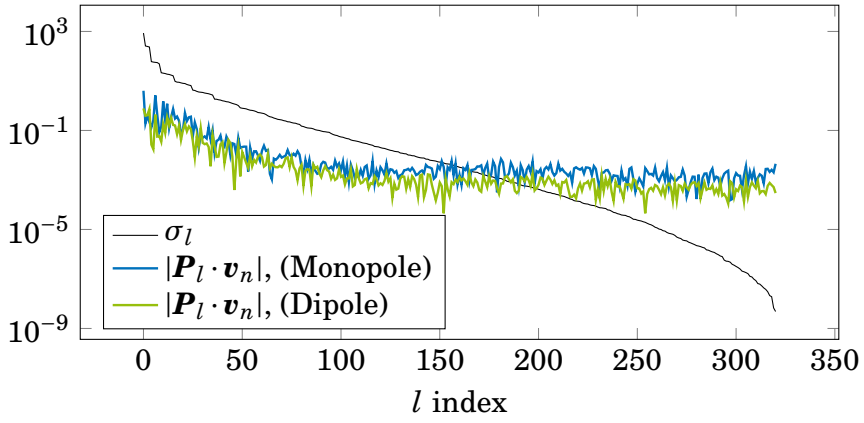

FIGURE 2.11 - *Picard plot of the $-\boldsymbol{v}_n = \boldsymbol{P}\boldsymbol{\Sigma}\boldsymbol{Q}^{\mathsf{H}}\tilde{\boldsymbol{q}}$ inverse problem at $ka = 2.1$. The set-up is the same as the one of Fig-2.3. On this example, singular values starts to decrease faster than $|\boldsymbol{P}_l \cdot \boldsymbol{v}_n|$, $\boldsymbol{P}$ for $l > 120$.*

2.4 Refinements for wind tunnel applications

2.4.1 Ground effects

Considering the rigid ground of a wind tunnel, a first significant step is to include ground reflections in the FRF computation process. Valdivia (2018, section 6) proposed to complete Eq.(2.2.4) with its copy assuming a symmetric set of equivalent sources underneath the ground. Formally, it leads to a new construction of the propagation matrices as $\forall j \leq N, \quad \forall l \leq N_s$,

$$\boldsymbol{G}_{j,l} = -\mathrm{i}\omega\rho\left(G\left(\boldsymbol{r}_j, \boldsymbol{r}_l\right) + G\left(\boldsymbol{r}_j, \boldsymbol{r}'_l\right)\right) \tag{2.4.1}$$

and

$$\boldsymbol{T}_{j,l} = \frac{e^{\mathrm{i}kr_{jl}}}{4\pi r_{jl}^2}(1-\mathrm{i}kr_{jl})\cos\theta_{jl} + \frac{e^{\mathrm{i}kr'_{jl}}}{4\pi r'^2_{jl}}(1-\mathrm{i}kr'_{jl})\cos\theta'_{jl}, \tag{2.4.2}$$

where $\boldsymbol{r}'_l, \theta'_l$ respectively denote the distance and the angle between the symmetric of the equivalent source $\tilde{q}_l$ about the ground and the j^{th} control point. By construction, any control point located on the surface of the ground corresponds to the case

$$r_{jl} = r'_{jl}, \quad \theta_{jl} = \pi - \theta'_{jl} \tag{2.4.3}$$

and the velocity normal to the ground is ensured to be zero.

Numerically speaking, equivalent image sources has the advantage of leaving unchanged the dimensions of the ESM inverse problem compared to the initial

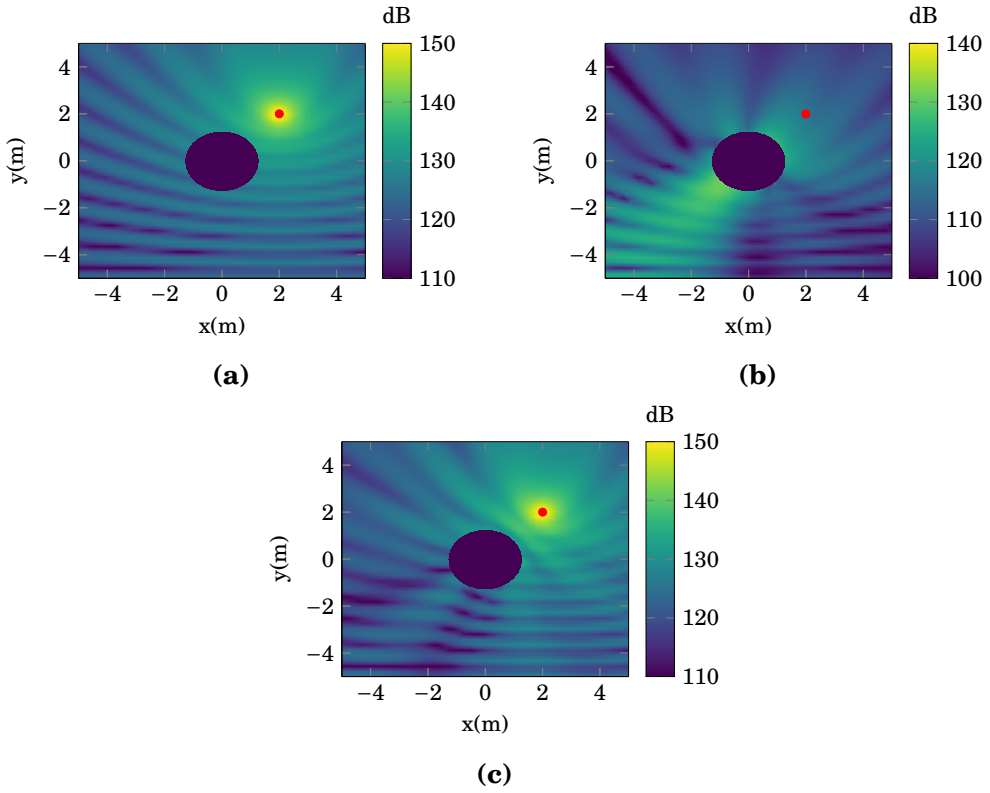

FIGURE 2.12 - *Acoustic pressure (amplitude) of (a) the incident field produced by a monopole (red dot); (b) the radiated field emitted by the equivalent sources; (c) the complete field, over a rigid ground at* $y = -5.5$ *m at* $ka = 1.3$.

case with no ground reflections. Again, an example of acoustic field simulated with source image ESM is given on Fig-2.12.

2.4.2 Shear layer refraction

The last major gap between a free field propagation and a wind tunnel set up lies in the convective effect of the flow and the shear layer appearing at the nozzle boundary levels. Under the assumption of an uniform flow at low Mach number, Amiet (1978) proposed an analogy with geometric optics to account for those phenomena : the shear layer is supposed infinitely thin and treated only as a sound speed variation between inside and outside the flow. Such a model does not take into account the effects of turbulences, but it accurately depicts modified trajectory of the sound waves swept away by the flow. Without it, imaging algorithms produces sources maps erroneously shifted downstream.

In the framework of section 2.2.1.1, the computation of the incident normal

velocity field in Eq.(2.2.5) is modified according to Amiet's model and the boundary condition part of the ESM inverse problems becomes:

$$\left(\mathbf{v}^i\mathbf{n}^\top\right)_j = \frac{e^{\mathrm{i}k\left(r_{ij}^{\mathrm{flow}}+r_{ij}^{\mathrm{ff}}\right)}}{4\pi\left(r_{ij}^{\mathrm{flow}}+r_{ij}^{\mathrm{ff}}\right)^2}\left(1-\mathrm{i}k\left(r_{ij}^{\mathrm{flow}}+r_{ij}^{\mathrm{ff}}\right)\right)\cos\theta'_{ij}. \tag{2.4.4}$$

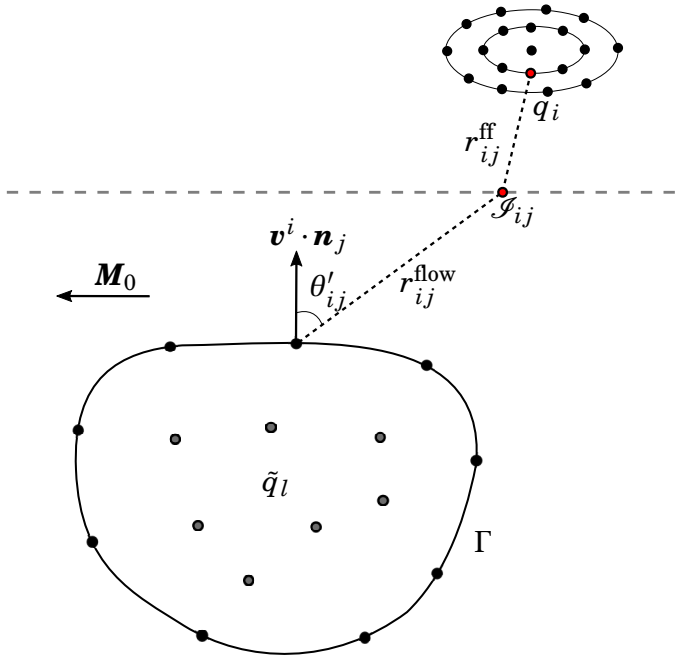

FIGURE 2.13 - *Refracted acoustic path in the ESM set up. The acoustic transfer is now composed of the paths covered outside and within the flow r_{ij}^{ff} and r_{ij}^{flow}, the impact point $\mathscr{I}_{ij}$ on the shear layer being obtained thanks to a iterative integrating scheme (Allen et al., 2002).*

As described on Fig-2.13, the FRF computation is thus completed assuming new angles of incidence with impact points on the shear layer instead of the arrays reciprocal sources, and spatial $1/r$ attenuation resulting from the refracted paths. The same treatment can be applied to equivalent image sources and dipolar incident sources as well.

2.5 Conclusion

Throughout this chapter was appraised the Equivalent Source Method for the simulation of FRF in an industrial context. After a depiction of the method, subtleties

related to the specific use of ESM for transfer functions between punctual sources and microphone arrays is given, notably the handling of singularity issues thanks to the paramount intervention of the reciprocity principle.

Some insights on the optimal settings are advocated in the perspective of aeroacoustic applications. As agreements on the equivalent source point cloud hardly arose from the literature, a study was conducted as a contribution to this field of research. Based on validations with respect to the spherical transfer function presented in section 1.3.2, the investigation exhibits random distributions as the most reliable option and a simple process to produce random point clouds inside arbitrarily shaped meshes was given in appendix A.

Lastly, declensions of the core ESM are exposed for the inclusion of facility related acoustic perturbations in the model. These modifications emphasizes the flexibility of ESM regarding on-the-fly adjustments to cope with various environments: the incident sound field and the propagation the equivalent sources can be seen as levers likely to be tailored. In the end, ESM is an algorithm simulating FRF taking into account scattering effects, and customisable for additional phenomena like ground reflections or shear layer refractions.

As it stands, FRF simulation for three-dimensional imaging is achievable with classical ESM but remains completely independent from array measurements. As mentioned in section 2.1, equivalent sources were already used in acoustic imaging without the notion of boundary conditions. With a view to level these observations, a new ESM approach specifically conceived for acoustic imaging was designed and presented in the next chapter.

CHAPTER 3

EQUIVALENT SOURCES AND INVERSE PROBLEM UNIFICATION: GALERKIN ESM

From the two previous chapters arises that significant benefits can be obtained from the use of ESM transfer functions. At this stage, ESM is however performed upstream to the measurements and the imaging process. The latter feature, added to the lack of published work on the interaction between inverse methods and refined FRFs, opens the path of further research on a well thought-out involvement of equivalent sources in acoustic imaging. In this chapter is proposed the Galerkin ESM (GESM) method as a new imaging algorithm that aims at the reconstruction of scattered sound fields based on array measurement without the intervention of pre-computed transfer functions.

3.1 Motivations

Several problems remain with the use of an externally computed $\boldsymbol{H}$ matrix. First has to be noticed that it splits the acoustic imaging process in two subsidiary inverse problem that are the simulation of the FRFs (for example with ESM, which boils down to a regularized pseudo inverse) and their inversion to identify the significant sources. Even though ESM is a quite fast algorithm that can be accelerated through GPU parallelization, an inevitable computational cost is added

especially for large models studied at high frequencies. In addition to that, the obtained FRFs concern only the acoustic path from the grid to the array, and the source distributions resulting from the inverse problem cannot be repropagated to specific points of interest without another FRF calculation.

It got clarified with section 2.1 that ESM in the literature refers both to a span of inverse methods involving free-field sources inside a radiating body and a simulation algorithm modeling sound propagation around surfaces supporting boundary conditions. The underlying idea of the Galerkin ESM exposed in this chapter is to formalize a connection between Koopman's initial ESM concept and its acoustic imaging applications: The concept of fitting a set of equivalent sources to conform to a given boundary condition can be borrowed from ESM, and included in the acoustic imaging inverse problem. Considering a Neumann boundary condition, this embedding takes the form of an orthogonal projection of the equivalent sources on the kernel of a matrix modeling the impedance of a rigid body. The basic inverse problem in Eq.(1.1.1) remains, but finds itself restricted to solutions satisfying an orthogonality constraint. A common feature between this approach and classical Galerkin approaches lies in the concept of searching for an optimal orthogonal basis arisen from the boundary condition of the model to solve a continuous physical inverse problem, hence the proposed Galerkin ESM denomination. The aim of Galerkin ESM is also to devise a crossover between classical ESM and acoustic imaging ESM in light of the differences discussed in section 2.1: the data provided by the phased microphone array is processed to identify virtual equivalent sources, and the latter are to be propagated to synthesize the acoustic fields at areas of interest.

By doing so, the reader may also consider that the question of the source support evoked in section 1.1.2 is bypassed : whatever the location of the actual acoustic sources (on the skin or in a detached region) or their nature (point or extended), the equivalent sources are supposed to reproduce the resulting pressure field if set correctly as it was demonstrated by Koopmann *et al.* (1989, section I).

The chapter is organized as follows : section 3.2 is dedicated to the mathematical formulation of GESM, from the statement of the inverse problem to the repropagation step providing the display of the pressure maps synthesized from equivalent sources. Then, in section 3.3, the emphasis is put on an in-depth study of the orthogonal projector involved in GESM. A lead to precondition the kernel matrix with a physical maximization of the radiation efficiency of the sources is exposed. In section 3.4, GESM is put to the test head-to-head against the well-assessed acoustic imaging methods that are CBF and iBF on a various set of test

cases featuring scattered sound propagations. With a full control on the target pressure fields, this benchmark is an opportunity to discuss the importance of supplying imaging algorithms with realistic transfer functions instead of the commonly used free field models.

3.2 Galerkin ESM

3.2.1 Overall methodology

Here again is considered a three-dimensional radiating body bounded by a closed surface Γ. The acoustic field is sensed via a set of M microphones located at the positions $(\boldsymbol{r}_i)_{i\leq M}$. The purpose of the method is to provide a description of the exterior acoustic field (both phase and amplitude) by means of equivalent sources placed inside Γ. The latter are to be determined with respect to the measured pressures $(\boldsymbol{p}_i)_{i\leq M}$ on the one hand, and to the impedance condition induced by the behaviour of the body on the other hand.

A discrete formulation of the problem is proposed now. Γ is modelled by a surface mesh featuring N nodes of positions $\left(\boldsymbol{r}_j\right)_{j\leq N}$ and a set of N_s equivalent monopolar acoustic sources are introduced at the positions $(\boldsymbol{r}_k)_{k\leq N_s}$ in the volume Ω (see Fig-3.1 for a schematic display).

Let $\boldsymbol{G}\in\mathbb{C}^{M\times N_s}$ be the matrix defining the acoustic free-field transfer functions between the equivalent sources and the pressure at the microphone positions, i.e. $\forall i\leq M,\ \forall l\leq N_s$,

$$\boldsymbol{G}_{il}=-\mathrm{i}\omega\rho G(\boldsymbol{r}_i,\boldsymbol{r}_l)=-\mathrm{i}\omega\rho\frac{e^{\mathrm{i}kr_{il}}}{4\pi r_{il}},\quad \boldsymbol{r}_i\in\bar{\Omega},\boldsymbol{r}_l\in\Omega. \tag{3.2.1}$$

Similarly can be defined the matrix $\boldsymbol{G}_\Gamma\in\mathbb{C}^{N\times N_s}$ describing the source to pressure transfer between the equivalent sources and the nodes on Γ, and $\boldsymbol{T}_\Gamma\in\mathbb{C}^{N\times N_s}$ the source to normal velocity transfer $\forall j\leq N,\ \forall l\leq N_s$,

$$\boldsymbol{T}_{\Gamma,jl}=\frac{e^{\mathrm{i}kr_{jl}}}{4\pi r_{jl}}\left(1-\mathrm{i}kr_{jl}\right)\cos\theta_{jl},\quad \boldsymbol{r}_j\in\Gamma,\boldsymbol{r}_l\in\Omega. \tag{3.2.2}$$

where θ_{jl} here denotes the angle between $\boldsymbol{r}_j-\boldsymbol{r}_l$ and the direction normal to Γ at $\boldsymbol{r}_j$.

Finally the impedance imposed by the radiating body is introduced as

$$z_j=\frac{p(\boldsymbol{r}_j)}{v_n(\boldsymbol{r}_j)},\ \boldsymbol{r}_j\in\Gamma. \tag{3.2.3}$$

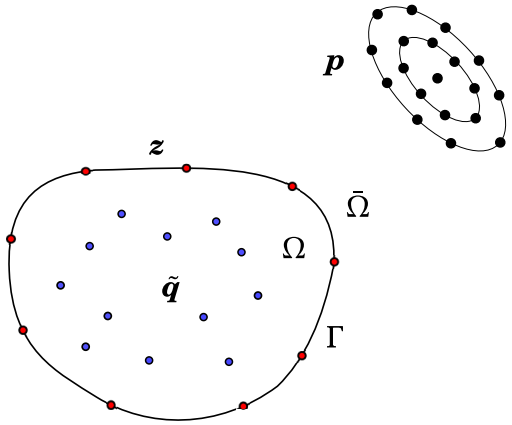

FIGURE 3.1 - *A set of equivalent monopolar sources with complex amplitudes $\tilde{\boldsymbol{q}}$ (blue dots) is sought after to match both the impedance condition $\boldsymbol{z}$ on the skin of the body and the pressure $\boldsymbol{p}$ measured by a microphone array at a given frequency.*

After stacking the impedances z_j into the diagonal matrix $\boldsymbol{Z}$, the inverse problem under scrutiny boils down to

$$\begin{cases} \boldsymbol{p} = \boldsymbol{G}\tilde{\boldsymbol{q}} & \text{(measurements matching)} \\ (\boldsymbol{Z}\boldsymbol{T}_\Gamma - \boldsymbol{G}_\Gamma)\tilde{\boldsymbol{q}} = 0 & \text{(boundary condition).} \end{cases} \tag{3.2.4}$$

From a mathematical standpoint, the goal here will be to solve a classical acoustic imaging inverse problem whose solution has to be projected on a null space accounting for the presence of the boundary condition.

Assuming Eq.(3.2.4) solved, the last step of the approach consists in the re-propagation of the obtained sources $\tilde{\boldsymbol{q}}$ on any observation region Γ_{obs} thanks to free field transfer matrices defined similarly to Eq.(3.2.1) and (3.2.2).

In the continuation of chapter 2, the particular case of a perfectly rigid body is investigated for the sake of simplicity. In other words, the admittance on Γ is set to zero which implies

$$\boldsymbol{T}_\Gamma \tilde{\boldsymbol{q}} = 0 \tag{3.2.5}$$

to account for a Neumann boundary condition, and the overall problem as stated in Eq.(3.2.4) becomes

$$\begin{cases} \boldsymbol{p} &= \boldsymbol{G}\tilde{\boldsymbol{q}} & \text{(measurements adequation)} \\ \boldsymbol{T}_\Gamma\tilde{\boldsymbol{q}} &= 0 & \text{(boundary condition).} \end{cases} \tag{3.2.6}$$

3.2.2 Null space of the boundary condition matrix

As the acoustic inverse problem turns into an algebraic projected inversion, the settings of the operating matrices dimensions is a major stake for the practical implementation of the method. M and N are considered as inputs of the problem: the number of microphones is given by the available hardware, and the number of nodes describing the body is fixed in accordance with the minimum wavelength under scrutiny. Concerning the test cases presented in section 3.4 and the next chapter, a 5 nodes per wavelength condition is matched to ensure a margin (Lee *et al.* (2011) showed that ESM approaches could be more resilient than FEM and BEM on this point).

The number of equivalent sources N_s is a key parameter of the method and requires further clarification. As it is mandatory that Eq.(3.2.5) admits non zero solutions for the proper operation of the method, the lowest N_s is first given by the rank theorem:

$$N_s = \mathrm{Rg}(\boldsymbol{T}_\Gamma) + \dim(\ker \boldsymbol{T}_\Gamma). \tag{3.2.7}$$

As $\boldsymbol{T}_\Gamma$ *is of full rank* (i.e. $\mathrm{Rg}(\boldsymbol{T}_\Gamma) = \min(N, N_s)$), a non-empty kernel implies $N_s > N$ and the number of equivalent sources must be greater than the number of nodes supporting the boundary condition on the body.

Under this assumption, the resolution of Eq.(3.2.6) involves the extraction of the kernel of $\boldsymbol{T}_\Gamma$. The simplest way to do so is based on the classical relationship

$$\ker \boldsymbol{T}_\Gamma = \left(\mathrm{Im}\boldsymbol{T}_\Gamma^{\mathsf{H}}\right)^{\perp} \tag{3.2.8}$$

where $\perp$ denotes the orthogonal set of a vector space.

From then on, the QR decomposition (see for example Golub and Van Loan, 1996) of $\boldsymbol{T}_\Gamma^{\mathsf{H}}$ is sufficient to sample a K sized matrix $\boldsymbol{B} \in \mathbb{C}^{N_s \times K}$ from the null space of $\boldsymbol{T}_\Gamma$. Let us first introduce

$$\begin{aligned} \boldsymbol{T}_\Gamma^{\mathsf{H}} &= \boldsymbol{Q}\boldsymbol{R} \\ &= \begin{bmatrix} \underbrace{\begin{matrix} \boldsymbol{Q}_{1,1} & \cdots & \boldsymbol{Q}_{1,N} \\ \boldsymbol{Q}_{2,1} & \cdots & \boldsymbol{Q}_{2,N} \\ \vdots & \cdots & \vdots \\ \boldsymbol{Q}_{N_s,1} & \cdots & \boldsymbol{Q}_{N_s,N} \end{matrix}}_{\mathrm{Im}\boldsymbol{T}_\Gamma^{\mathsf{H}}} & \underbrace{\begin{matrix} \boldsymbol{Q}_{1,N+1} & \cdots & \boldsymbol{Q}_{1,N_s} \\ \boldsymbol{Q}_{2,N+1} & \cdots & \boldsymbol{Q}_{2,N_s} \\ \vdots & \cdots & \vdots \\ \boldsymbol{Q}_{N_s,N+1} & \cdots & \boldsymbol{Q}_{N_s,N_s} \end{matrix}}_{\text{null space of } \boldsymbol{T}_\Gamma} \end{bmatrix} \boldsymbol{R}, \end{aligned} \tag{3.2.9}$$

where $\boldsymbol{Q} \in \mathbb{C}^{N_s \times N_s}$ is an unitary matrix and $\boldsymbol{R} \in \mathbb{C}^{N_s \times N}$ is an upper triangular

matrix.

Equation (3.2.9) can be rewritten as

$$\boldsymbol{T}_\Gamma^{\mathsf{H}} = \begin{bmatrix} \boldsymbol{Q}_1 & \boldsymbol{Q}_2 \end{bmatrix} \boldsymbol{R}, \tag{3.2.10}$$

with $\boldsymbol{Q}_1 \in \mathbb{C}^{N_s \times \mathrm{Rg}(\boldsymbol{T}_\Gamma)}$ describing the image of $\boldsymbol{T}_\Gamma^{\mathsf{H}}$ and $\boldsymbol{Q}_2 \in \mathbb{C}^{N_s \times (N_s - \mathrm{Rg}(\boldsymbol{T}_\Gamma))}$ being a set of orthogonal rows in the kernel of $\boldsymbol{T}_\Gamma$. From there, any matrix $\boldsymbol{B}$ of the form

$$\boldsymbol{B} = \boldsymbol{Q}_2 \boldsymbol{\Lambda}, \quad \boldsymbol{\Lambda} \in \mathbb{C}^{(N_s - \mathrm{Rg}(\boldsymbol{T}_\Gamma)) \times K} \tag{3.2.11}$$

ensures that $\boldsymbol{T}_\Gamma \boldsymbol{B}$ will equal zero.

The $\boldsymbol{B}$ matrix is the cornerstone of the proposed Galerkin ESM as it plays two major roles:

- Because of its similarity with $\boldsymbol{Q}_2$, it can force equivalent sources to respect the Neumann boundary condition stated in Eq.(3.2.5).
- The appropriate construction of $\boldsymbol{\Lambda}$ allows the reduction of the inverse problem dimension in Eq.(3.2.4) from N_s to K unknowns.

Leads to define what can be a relevant definition of this matrix is investigated in section 3.3.

3.2.3 Practical inversion

The initial system (3.2.4) can now be reduced to a single inverse problem

$$\boldsymbol{p} = \boldsymbol{G}\tilde{\boldsymbol{q}} = \boldsymbol{G}\boldsymbol{B}\boldsymbol{d} \tag{3.2.12}$$

where the new unknown vector $\boldsymbol{d} \in \mathbb{C}^K$ may be understood as a set of equivalent source coefficients projected on a basis accounting for the Neumann boundary condition on the body.

Since it is desirable for this new statement of the problem to be correctly conditioned, a parametric condition arises from Eq.(3.2.12) as it should not be under determined. This means that the size of the kernel basis K has to be larger than the output dimension M of the matrix $\boldsymbol{G}\boldsymbol{B}$ to invert, which necessarily leads to

$$M \leq K \leq N_s - N. \tag{3.2.13}$$

This prerequisite on the number of equivalent sources will be supported by numerical considerations in section 3.4.

Now that the inverse problem boils down to the formulation Eq.(3.2.12) remains the choice of an inversion algorithm to reach the solution $\boldsymbol{d}$. A large scope of sophisticated algorithms are available in the literature, briefly presented in the literature review at section 1.2. The shape of the optimal solution $\boldsymbol{d}$ (i.e. for example sparse or with minimum energy) is case-dependant and likely to be influenced by the choice of $\boldsymbol{\Lambda}$. For that reason, the generic choice would be to make use of an L^2 regularized inversion. This is the one made in the framework of this chapter in the validation sections, with the regularization parameter set up according to Pereira *et al.* (2015) Bayesian regularization algorithm.

Once $\tilde{\boldsymbol{q}}$ is recovered from Eq.(3.2.12), the last step consists in the repropagation of the optimal equivalent sources vector $\tilde{\boldsymbol{q}} = \boldsymbol{B}\hat{\boldsymbol{d}}$ to estimate the radiated pressure in the region of interest within $\bar{\Omega}$. This is simply achieved with the free field propagator following

$$\boldsymbol{p}_{\text{obs}} = \boldsymbol{G}_{\bar{\Omega}}\tilde{\boldsymbol{q}}. \tag{3.2.14}$$

For this repropagation to be meaningful, a noticeable precaution has to be highlighted: since the equivalent sources arising from Galerkin ESM are designed to acoustically model the object defined by Γ, it is mandatory for this region of interest not to intersect Γ. This would indeed boil down to evaluating the pressure radiated by the body inside or on itself, and most likely lead to incoherent results and interpretations. Indeed, like classical ESM or BEM, the Galerkin inverse problem is dedicated to the simulation of the acoustic field outside the source region since the $1/r$ singularity of the monopoles is unmanageable within Ω. Apart from this area, it is supposed to provide a realistic synthesized acoustic field outside the rigid body based on the microphone array measurements.

In the end, the overall execution of Galerkin ESM is summarized in Algorithm 3.2.3.

From the computational cost point of view, the two most significant steps are the QR decomposition ($\mathcal{O}\left(N^3\right)$ operations using PYTHON numpy Householder reflectors) and the inversion of $\boldsymbol{GB}$ that will depend on $\boldsymbol{\Lambda}$ and the chosen inverse methods.

3.3 Kernel layout through principal surfaces

When choosing the simplest form for $\boldsymbol{\Lambda}$, i.e. a rectangular matrix with unitary entries on its diagonal, there is no genuine reason to expect any dimension reduction

Algorithm 1 Step-by-step description of Galerkin ESM

Require: Array measures $\boldsymbol{p} \in \mathbb{C}^M$, N node positions on Γ, N_s equivalent sources positions in Ω, and a region of repropagation Γ_{obs} featuring N_{obs} points.
Ensure: $M \leq N_s - N$ and $\Gamma \cap \Gamma_{\text{obs}} = \varnothing$
$\boldsymbol{G} \in \mathbb{C}^{M \times N_s} \leftarrow$ Eq.(3.2.1).
$\boldsymbol{T}_\Gamma \in \mathbb{C}^{N \times N_s} \leftarrow$ Eq.(3.2.2).
$\boldsymbol{Q}_2, \boldsymbol{R} \leftarrow$ QR decomposition of $\boldsymbol{T}_\Gamma^{\mathsf{H}}$.
$\boldsymbol{\Lambda} \in \mathbb{C}^{(N_s - \text{Rg}(\boldsymbol{T}_\Gamma)) \times K} \leftarrow$ User defined, see section 3.3.
$\boldsymbol{B} \leftarrow \boldsymbol{Q}_2 \boldsymbol{\Lambda}$.
$\hat{\boldsymbol{d}} \leftarrow$ regularized inversion of $\boldsymbol{p} = \boldsymbol{G}\boldsymbol{B}\boldsymbol{d}$.
$\boldsymbol{p}_{\text{obs}} \leftarrow \boldsymbol{G}_{\Gamma_{\text{obs}}} \boldsymbol{B} \hat{\boldsymbol{d}}$.

from $N_s - N$ to K: in that case $\boldsymbol{B}$ is directly sampled from the QR decomposition, which is a pure mathematical operation with no physical meaning involved. The selection of columns from $\boldsymbol{Q}_2$ is thus bound to be arbitrary and it is shown in the next section that Galerkin ESM is unlikely to provide meaningful results with small values of K in this set up.

As mentioned in the previous section, the construction of $\boldsymbol{\Lambda}$ thus deserves an in-depth analysis since it impacts both the physical meaning of the equivalent sources model and the numerical cost of the inverse problem. The current section is dedicated to a practical way to define an acoustic operator from which are derived principal radiating surfaces. For the sake of clarity, only one promising option is advocated in this section, but some other leads could be studied as well depending on the application cases.

Sources with maximum radiation efficiency

The proposed option is to *tidy up* the columns of $\boldsymbol{Q}_2$ following an order of increasing efficiency in terms of acoustic radiated power. For that purpose, the choice was to test Galerkin ESM featuring a $\boldsymbol{\Lambda}$ matrix filled with K eigenvectors associated to the largest eigenvalues of the radiation efficiency operator.

Given a closed surface completely covering the rigid body ($\Gamma_W \subset \bar{\Omega}$) and discretized in N_W nodes and surface elements, the acoustic power propagated by the equivalent sources $\tilde{\boldsymbol{q}}$ through Γ_W is determined by

$$W = \frac{1}{2}\Re e\left(\boldsymbol{v}_n^{\mathsf{H}} \boldsymbol{A} \boldsymbol{p}\right) = \frac{1}{2}\Re e\left(\left(\boldsymbol{T}_{\Gamma_W}\tilde{\boldsymbol{q}}\right)^{\mathsf{H}} \boldsymbol{A} \boldsymbol{G}_{\Gamma_w}\tilde{\boldsymbol{q}}\right) \tag{3.3.1}$$

where $\boldsymbol{T}_{\Gamma_W}, \boldsymbol{G}_{\Gamma_W}$ are the free field propagation matrices of $\tilde{\boldsymbol{q}}$ on Γ_W respectively

for normal velocity and pressure, and $\boldsymbol{A} \in \mathbb{R}^{N_W \times N_W}$ is a diagonal matrix containing the areas of Γ_W surface elements.

From that perspective, it seems relevant to favour distributions of equivalent sources with the best radiation efficiency when reducing the size of the inverse problem. In practice this can be achieved by setting the columns of $\boldsymbol{\Lambda}$ as

$$\boldsymbol{\Lambda} = [\boldsymbol{\lambda}_1, \ldots, \boldsymbol{\lambda}_K] \tag{3.3.2}$$

where

$$\boldsymbol{\lambda}_i = \underset{\substack{\|\boldsymbol{u}\|=1 \\ \boldsymbol{u}^{\mathsf{H}}\boldsymbol{\lambda}_j=0,\ j\leq i-1}}{\arg\max} \ \frac{1}{2}\boldsymbol{u}^{\mathsf{H}} \Re e\left(\boldsymbol{Q}_2^{\mathsf{H}} \boldsymbol{T}_{\Gamma_W}^{\mathsf{H}} \boldsymbol{A} \boldsymbol{G}_{\Gamma_w} \boldsymbol{Q}_2\right) \boldsymbol{u}. \tag{3.3.3}$$

All in all, the matrix $\boldsymbol{B} = \boldsymbol{Q}_2\boldsymbol{\Lambda}$ brings in a combination of a projection on the kernel of $\boldsymbol{T}_\Gamma$ while sorting the equivalent sources distribution in ascending order regarding their radiation efficiency on Γ_W. Through this intermediary step, a physical behaviour is coupled to $\boldsymbol{Q}_2$ and allows to significantly reduce the size of the inverse problem without damaging its accuracy. An illustration of how radiate such principal surfaces and the quantitative gain of the introduction of $\boldsymbol{\Lambda}$ defined with Eq.(3.3.3) is put forth in section 3.4.

Another subsidiary benefit lies in the orthogonality between the columns of $\boldsymbol{B}$. Considering further applications of Galerkin ESM, one could think of decomposing the overall radiated acoustic power on the principal surfaces according to

$$W = \sum_{i=1}^{K} w_i, \quad \text{where } w_i = |d_i|^2 \, \Pi_i, \tag{3.3.4}$$

with Π_i being the i^{th} eigenvector of the matrix $\frac{1}{2}\Re e\left(\boldsymbol{Q}_2^{\mathsf{H}} \boldsymbol{T}_{\Gamma_W}^{\mathsf{H}} \boldsymbol{A} \boldsymbol{G}_{\Gamma_w} \boldsymbol{Q}_2\right)$ in Eq.(3.3.3) and d_i the i^{th} coefficient of $\boldsymbol{d}$. Such a process is likely to provide some insightful hierarchy in the operating radiative patterns (see Fig. 3.8,3.9,3.10 in the next section for a example on an academic case).

3.4 Numerical Validation

A comparison of Galerkin ESM with other acoustic imaging algorithms is proposed in this section. The purpose of the method is to reconstruct acoustic fields outside a rigid surface. To evaluate these methods from that angle, the spherical geometry used in the previous chapter is chosen: with respect to Fig-3.1, Γ is modelled here by a spherical mesh of radius $a = 0.3$ meters featuring 1280 triangular elements

and $N = 642$ nodes. As they get equally spread over the sphere, this set of nodes allows a 5 elements per wavelength condition up to $ka = 15$.

The acoustic field radiated around a rigid box (see for example Koopmann and Fahnline, 1991; Bouchet *et al.*, 2000) is a common test case for ESM approaches. However, the point of this chapter is also to put Galerkin ESM to the test in terms of three-dimensional diffracted source identification based on array imaging. From that perspective, the spherical case offers valuable advantages. First of all, the pressure in the vicinity of a rigid sphere given a monopolar source on its skin is analytically known (Williams, 1999, section 8.8)): considering the sphere centred on the origin, the acoustic transfer function between a unitary monopolar source located at $\boldsymbol{r}_l$ on the spherical surface Γ and a microphone at $\boldsymbol{r}_i$ in the outer field was given in chapter 1.3.2 by Eq.(1.3.9).

An observation surface Γ_{obs} is set up for the display of the acoustic fields propagated by the equivalent sources from Galerkin ESM and the sources identified through classical acoustic imaging methods. It consists in an additional sphere of radius $a_{\text{obs}} = \frac{4}{3}a$ merged with a cutting plane of size $5a$ (see Fig-3.2). This set-up allows to check discrepancies between the obtained propagated fields and the analytical one on both near and far field.

For the sake of simplicity, the choice was made to use a regular spherical array of radius $\frac{16}{3}a$ with $M = 250$ microphones.

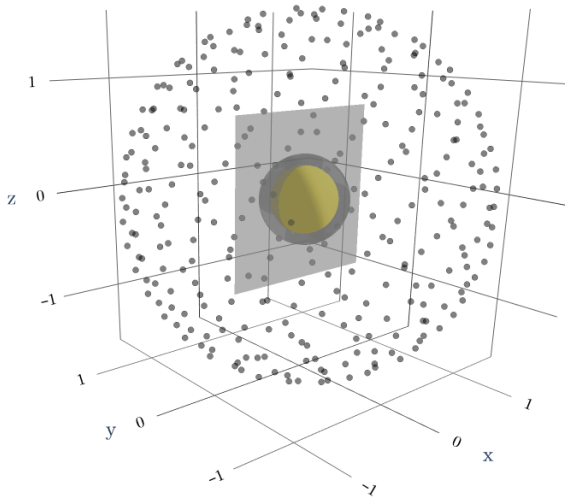

FIGURE 3.2 - *Geometrical set-up for validation. The yellow surface is the control point support Γ, the transparent grey (plane and concentric outer sphere) is Γ_{obs} and the cloud of points around it is the microphone array.*

In accordance with section 2.2.3.1, The positioning of the equivalent source

cloud point remains an open-ended question. It is all the more a prospective issue that the numerical stability of GESM relies on the $\boldsymbol{GB}$ matrix more than on $\boldsymbol{T}$: this means that the results already available in the ESM literature are likely not to be as relevant as they were for classical ESM. As it stands, the trial-and-error is still the most straightforward option and it was used in this section. The retreat distance ξ_d was set to 0.15a. This was empirically stated by Dunn and Tinetti (2008), and the same conclusion emerged from Fig-3.3.

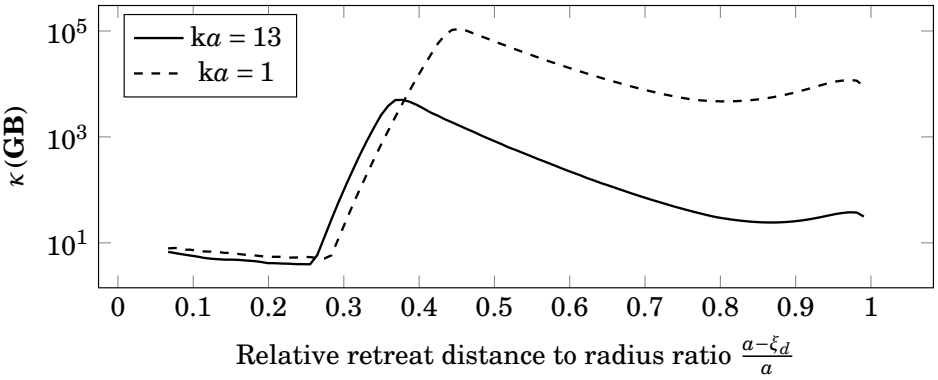

FIGURE 3.3 - *Sensitivity of the GESM propagation matrix $\boldsymbol{GB}$ to the retreat distance ξ_d for the spherical geometry.*

This plot emphasizes that the best numerical set up is achieved either with equivalent sources concentrated in a small volume nearby the center of the mesh $\left(\frac{a-\xi_d}{a}\right) < 0.25$ or limited to a $\left(\frac{a-\xi_d}{a}\right) \approx 0.85$ scaled version. Concentrated equivalent sources lead to well conditioned matrices but Ochmann (1995) showed that they were physically irrelevant at high frequencies for disturbed acoustic fields. In the end, the second option $\xi_d \approx 0.15a$ was considered as a good balance to keep manageable conditioning numbers.

3.4.1 Presentation of the benchmark protocol

Considering the validation case below, Galerkin ESM is benchmarked against two already existing acoustic imaging approaches presented earlier on in section 1.2.

- The first is Conventional Beamforming. Even if it is only theoretically justified for the identification of a single monopolar radiating source in a free field toward the array, CBF remains a reference in industrial applications and a comparison with CBF output is a necessary step for the evaluation of new acoustic imaging methods.

- The second is iterative Bayesian Focusing. The purpose here is to benchmark Galerkin ESM with a current state-of-the-art algorithm, assessed as an imaging approach that provides the full cross spectral matrix of the sources, which includes a regularization step to deal with noisy measurements or poorly conditioned FRFs

The comparison study features five different approaches to reconstruct the acoustic field:

1. CBF between N monopole sources on the mesh Γ and the array, featuring the free-field propagation of Eq.(3.2.1) in the transfer matrix $\boldsymbol{H}$ of Eq.(1.2.2).

2. CBF involving the analytical transfer Eq.(1.3.9) in $\boldsymbol{H}$.

   With these first two is tested the usability of CBF for sound field synthesis and its ability to handle non free-field FRFs.

3. iBF between N monopole sources on Γ and the array, with free-field FRF and without any prior hypothesis on the sources in terms of regularization.

   This one serves at evaluating what a *turnkey* version of iBF produces.

4. Galerkin ESM as described in section 3.2, with $N_s = 3N = 1926$ and $K = N_s - N = 1284$ in a first stage, to maintain a margin regarding Eq.(3.2.13). No principal surfaces for the validation in comparison with other imaging algorithms to remain general. The equivalent sources are distributed inside the mesh according to classical ESM literature guidelines: half of it are placed on a 85% scaled replica of Γ and the other half randomly located but at least $0.15a$ m away from the control points (see Leblanc *et al.*, 2010).

5. Lastly iBF again, but with the use of the analytical FRF in $\boldsymbol{H}$ and a strong sparsity constraint (L^1 regularization). It should be noted that this last approach differs from the first four as it is the only one that features a suitable a priori on the sources. It aims at displaying the maximum degree of accuracy reachable on the reconstructed scattered field when the inverse method perfectly fits with the ground truth source distribution.

The aim of such a methodology is multiple:

- Checking the error induced by approximated FRFs in CBF and iBF when the actual propagation is not free field.

- Assessing the ability of CBF and iBF to benefit from the use of a perfectly accurate transfer function.

- Evaluating Galerkin ESM comparatively to what is reachable with *blind* acoustic imaging approaches (i.e. without proper assumptions on the source distribution) and with the perfectly tuned iBF version.

3.4.2 Monopolar sources on sphere

3.4.2.1 Uncorrelated monopoles

The first test case consists in the reconstruction of the acoustic field produced by $N_{\text{src}} = 10$ uncorrelated monopoles randomly placed on the yellow sphere (on Fig. 3.2). The cross spectral matrix (CSM) resulting from their combined radiation at the microphones is computed through

$$\boldsymbol{S}_{pp} = \boldsymbol{H}^{\text{s}} \boldsymbol{S}_{qq} \left(\boldsymbol{H}^{\text{s}}\right)^{\text{H}}, \tag{3.4.1}$$

where $\boldsymbol{H}^{\text{s}}$ is determined according to Eq.(1.3.9) and $\boldsymbol{S}_{qq}$ is set to the identity matrix in order to describe completely uncorrelated sources of unitary strength. Each algorithm is then fed with this CSM and the sources obtained are finally repropagated on a circle of radius $1.5a$. The directivities resulting from this process are plotted on Fig-3.4.

This first configuration is supposed to fall in the range of all the methods assessed, but this first benchmark offers interesting preliminary conclusions. Methodwise, it seems that the overall directivity pattern is seized by both CBF, iBF and Galerkin ESM.

It appears then that the use of the accurate FRFs leads to an enhancement at high frequencies, dealing with some 5 dB discrepancies for both beamforming and Bayesian Focusing. This item is quite intuitive and shows how the diffraction of the spherical body plays a role in the acoustic transfer and should not be underestimated.

With respect to the classical methods, Galerkin ESM (green dotted line Fig-3.4) may be ranked at the second place in terms of accuracy. It outperforms CBF in general, deals with the impact of diffraction in a much better way than iBF with free-field FRFs, but does not compete with the latter when used with spherical transfer functions and induced sparsity.

It may be noticed that at both high and low frequencies, iBF with correct trans-

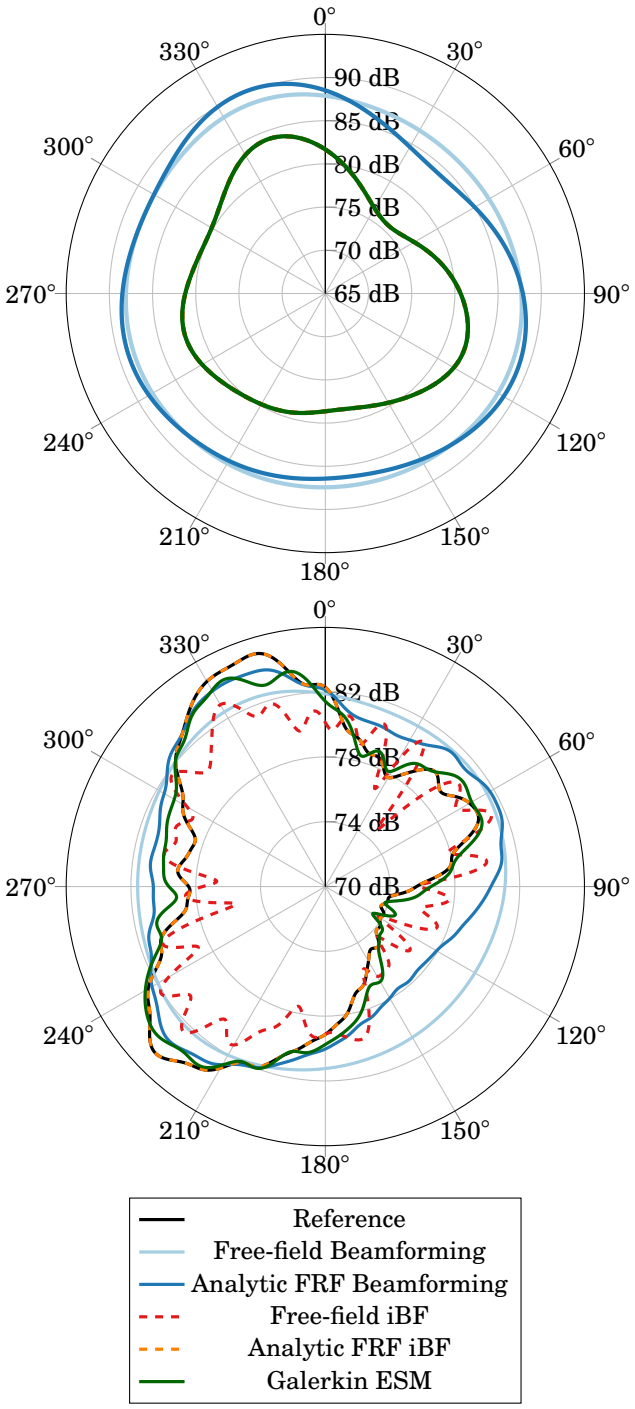

FIGURE 3.4 - *Directivity pattern of 10 uncorrelated monopoles on a rigid sphere at $ka = 1$ (top) and $ka = 13$ (bottom), computed through various imaging algorithms. At low frequency, both Galerkin ESM and iBF are matching with the reference (all 4 plots are overlapped).*

fer functions (yellow dashed line) perfectly managed to reconstruct the reference directivity of the ten sources. This basically means that the number and the disposition of the microphones allows enough information to fully describe the acoustic field. That being said, it should be concluded that Galerkin ESM is by far the best performing algorithm among the without *a priori* approaches even if there is still room for improvements.

3.4.2.2 Correlated monopolar sources

The panel of imaging approaches is now put to the test for the recovery of an acoustic field produced by the same ten monopoles, but this time correlated: the CSM and the the reference directivity pattern is obtained in the same way as in the previous section using Eq.(3.4.1), except that $\boldsymbol{S}_{qq}$ is no longer the identity matrix. Instead, it gets defined as

$$\boldsymbol{S}_{qq} = \boldsymbol{I}_{N_{\text{src}}} + \boldsymbol{\Delta}_{N_{\text{src}}} + \boldsymbol{\Delta}_{N_{\text{src}}}^{\mathsf{H}} \tag{3.4.2}$$

where $\boldsymbol{\Delta}_{N_{\text{src}}}$ is an upper triangular matrix randomly filled with 0 or 1 entries. The ten sources on the sphere are thus either fully or not correlated one with each other, causing a much more complex and uneven directivity pattern than in the previous paragraph.

Results are plotted on Fig-3.5. As expected, CBF loses relevance when dealing with correlated sources and fails at nailing the interference peaks. Regarding iBF, the scattering effect of the sphere becomes of first order at large ka number and the quality of the output is damaged as long as a free field transfer function is used. In that case, levels seem to be underestimated with respect to the reference: inherently to their propagation model, the identified sources are namely interfered *through* the spherical mesh at the repropagation step of the process leading to overall lower levels because of the inappropriate L^2 regularization with respect to the source model.

Here again, Galerkin ESM does well as being in the efficiency range of the optimal set-up offered by iBF with spherical related transfer functions. Every interference lobe is well rendered at both high and low frequencies, only remain some local discrepancies with the reference. This uneven aspect may likely result from a non optimal disposition of the equivalent sources, which constitutes the major lead for further improvements of the method.

With a view to exemplify the potential applications of Galerkin ESM, the repropagation depicted in Eq.(3.2.14) is achieved and displayed on Fig-3.7 and Fig-

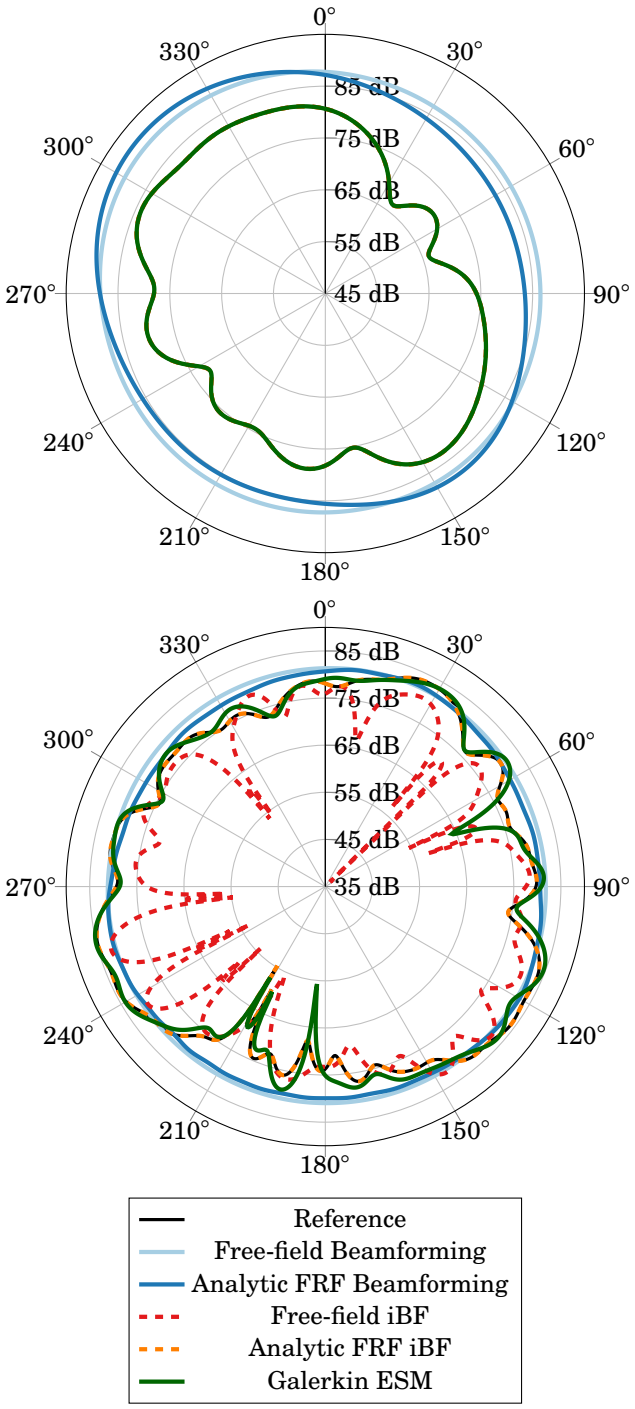

FIGURE 3.5 - *Directivity pattern of 10 correlated monopoles on a rigid sphere at $ka = 1$ (top) and $ka = 13$ (bottom), computed through various imaging algorithms. At low frequency, both Galerkin ESM and iBF are matching with the reference (all 4 plots are overlapped).*

3.6 for un correlated and correlated monopoles (5 only for the sake of readability). Comparing (a) and (b), this result highlights to what extent the free assumption leads to misleading interpretations on the left side of the sphere. On this test case, it appears that iBF with accurate FRFs and Galerkin ESM only can provide a reliable repropagated sound field.

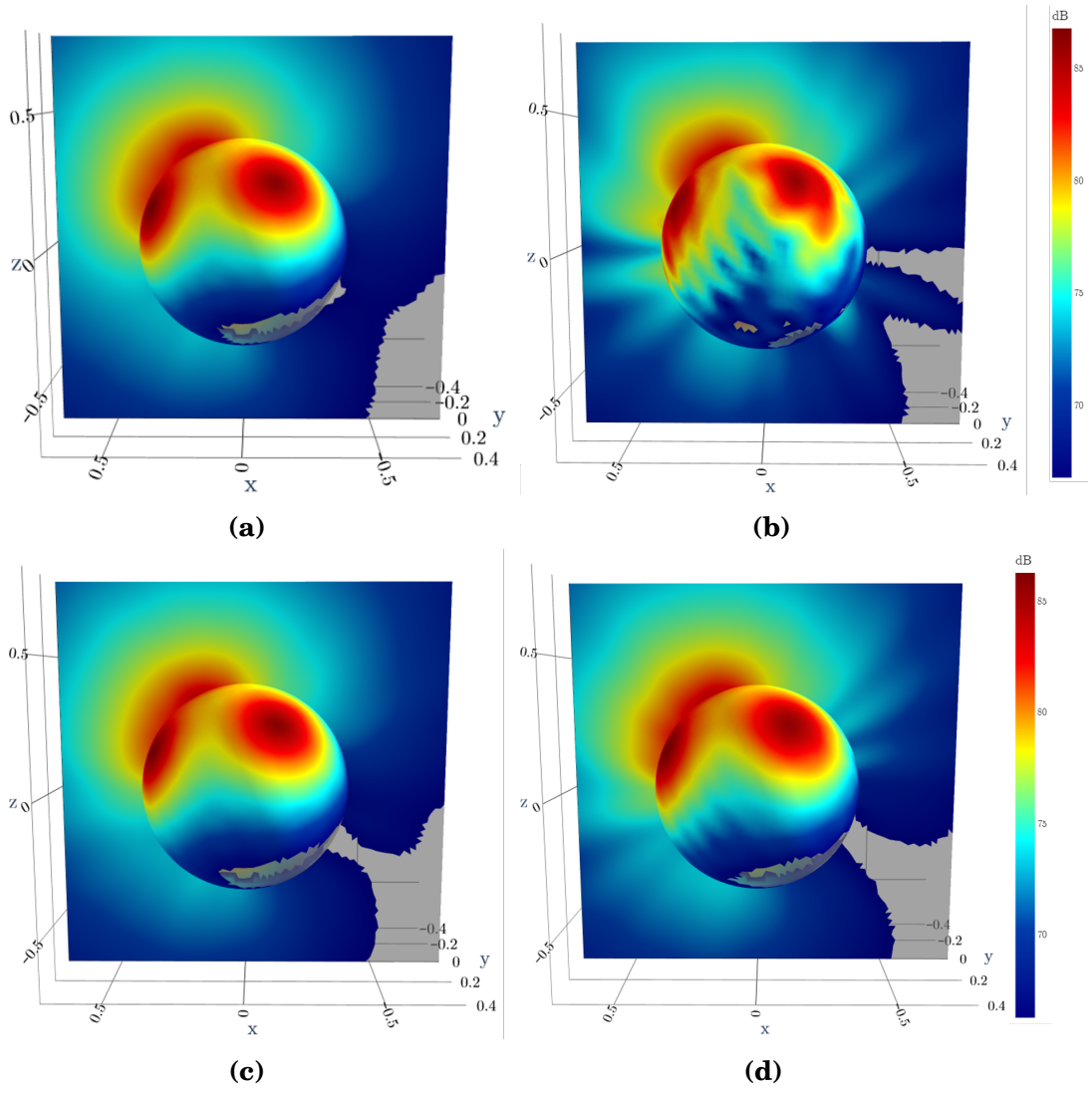

FIGURE 3.6 - *Acoustic pressure (amplitude) on Γ_{obs} radiated by 5 uncorrelated monopoles at $k = 13$ (with a 20 dB dynamic range). (a) Analytical sound field. (b) Sound field propagated by sources identified with iBF featuring free-field FRF. (c) Sound field propagated by sources identified with iBF featuring analytical FRF. (d) Sound field propagated by sources identified with Galerkin ESM.*

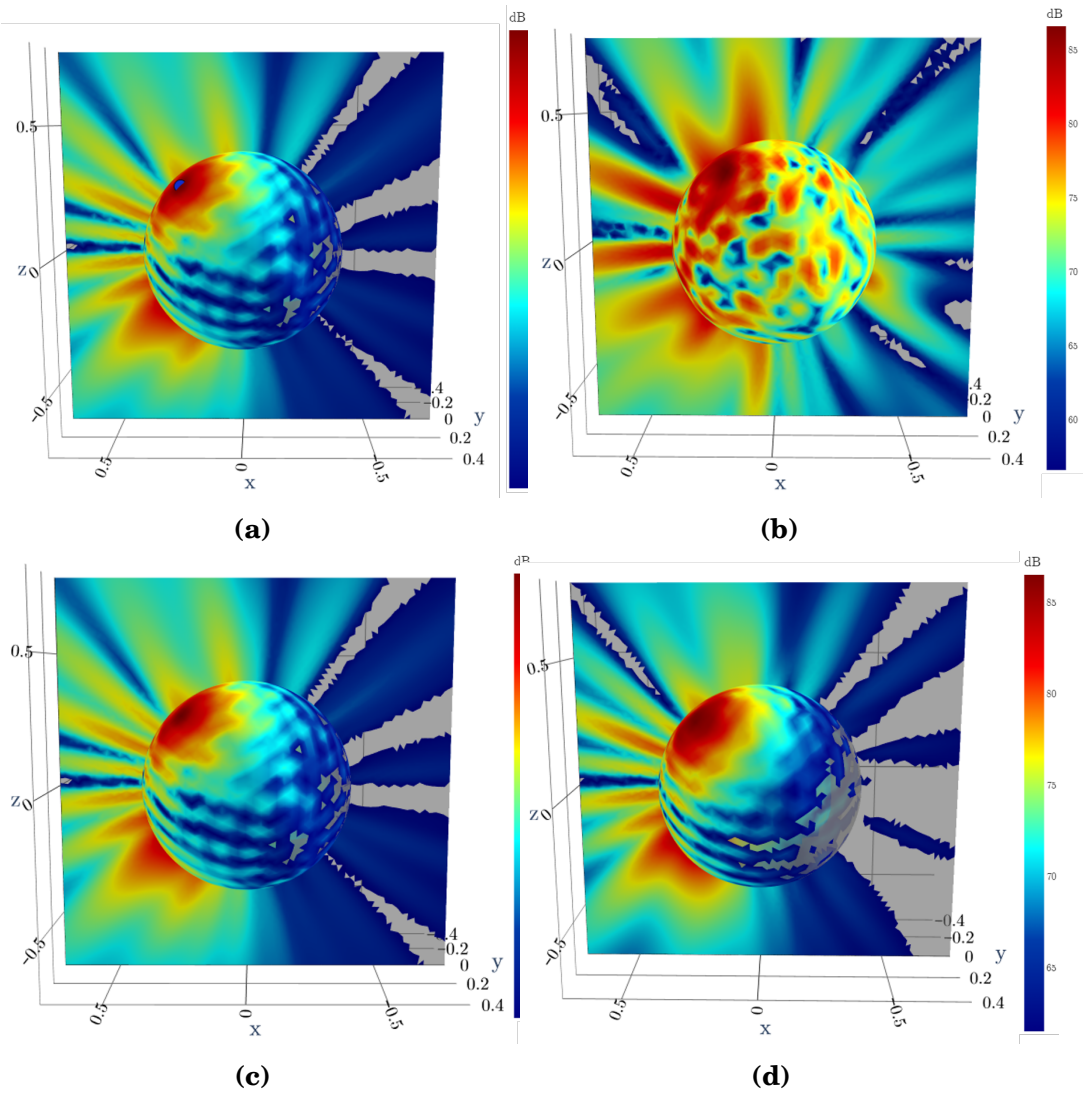

FIGURE 3.7 - *Acoustic pressure (amplitude) on Γ_{obs} radiated by 5 randomly correlated monopoles at $k = 13$ (with a 20 dB dynamic range). (a) Analytical sound field. (b) Sound field propagated by sources identified with iBF featuring free-field FRF. (c) Sound field propagated by sources identified with iBF featuring analytical FRF. (d) Sound field propagated by sources identified with Galerkin ESM.*

All in all, the conclusion regarding the numerical test cases seems consistent. In terms of methods ranking, it can be stated that:

- Beamforming is unusable at low frequencies for radiated field reconstruction. The poor spatial resolution on the identified sources leads to over smoothed propagated fields completely blurring directivity patterns. At large ka values, the use of accurate FRFs as steering vectors for CBF slightly improves it but this statement remains especially when dealing with correlated sources.

- At high frequencies, i.e. when the scattering behaviour of the sphere is of first order, the identification of the outer pressure field with iBF should be achieved with great precautions. Without any prior knowledge on the sources nature, the generic parametrization of the algorithm with free-field transfer functions and L^2 regularization leads to significant inaccuracies. In practice, this means that iBF should be used for array-based field synthesis only when refined transfer functions and funded assumptions on the sources are available.

- Galerkin stands out as a powerful alternative to have a proper simulation of the acoustic field around the rigid sphere without ground truth FRFs. Discrepancies with the reference are observable but local and acceptable. The peaks induced by the scattering presence of the sphere is well modelled by the kernel projection added to precondition the free-field transfer matrices as exposed in section 3.2.

3.4.3 Principal Surfaces

Given its reasonable size, the spherical case used throughout this section is ideal to evaluate the contribution of principal surfaces introduced in section 3.3.

A 5/4 scaled version of the mesh plotted in Fig-3.2 was chosen as Γ_W discretized in $N_W = N = 642$ nodes. The $\boldsymbol{\Lambda}$ matrix of size $N_s \times N_s$ was filled with columns computed following Eq.(3.3.3) and it is insightful to visually check their radiative pattern as basis vector for the Galerkin ESM inverse problem. For that purpose, the amplitude of the pressure field radiated by the columns of $\boldsymbol{B}$ on Γ_{obs}, i.e.

$$\boldsymbol{p}_{\text{obs}}^{\boldsymbol{\lambda}_i} = \boldsymbol{G}_{\Gamma_{\text{obs}}} \boldsymbol{B}_i \tag{3.4.3}$$

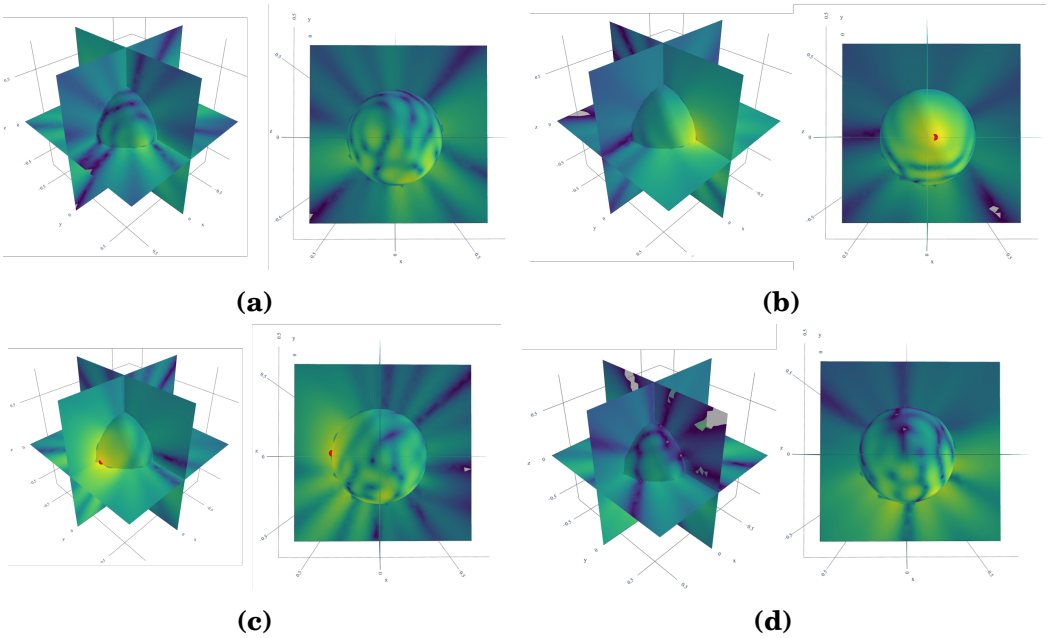

FIGURE 3.8 - *Pressure amplitudes on Γ_{obs} radiated by the i^{th} column of $\boldsymbol{Q}_2\boldsymbol{\Lambda}$ ($\boldsymbol{\Lambda}$ being the identity matrix); (a) $i = 1$; (b) $i = 10$; (c) $i = 100$; (d) $i = 250$ and $ka = 8.24$. Plots are displayed within a 30 dB dynamic range, and the red dot indicates the maximum level location.*

was computed for various i values and displayed in Fig-3.8 with $\boldsymbol{\Lambda}$ being the identity matrix and Fig-3.9 with $\boldsymbol{\Lambda}$ issued from Eq.(3.3.3).

A relevant point arises from the observation of these figures and confirms the reasoning exposed in section 3.3: On the one hand, in terms of acoustic radiation, no obvious hierarchy seems to sort the basis vector inside $\boldsymbol{B}$ when $\boldsymbol{\Lambda}$ is the identity. In other words, every columns of $\boldsymbol{Q}_2$ share the same radiation efficiency and it is unlikely to sample $K < N_s - N$ of them without any loss on the accuracy on the Galerkin ESM outcome.

On the other hand, from Fig-3.9 it appears that the power-optimized version of $\boldsymbol{\Lambda}$ leads to much more workable basis functions, with a clear ranking between the most radiating vector at low i values and the weakest ones at larger indices.

The quantitative assessment of this interpretation was conducted and shown in Fig-3.10. The latter exposes the global L^2 relative error on Γ_{obs} between the analytical pressure field and the one propagated by Galerkin ESM sources, with respect to the number of columns K selected from $\boldsymbol{\Lambda}$. Simultaneously is plotted the relative acoustic power of the equivalent sources integrated on Γ_W for rising truncation values K in the sum of Eq.(3.3.4).

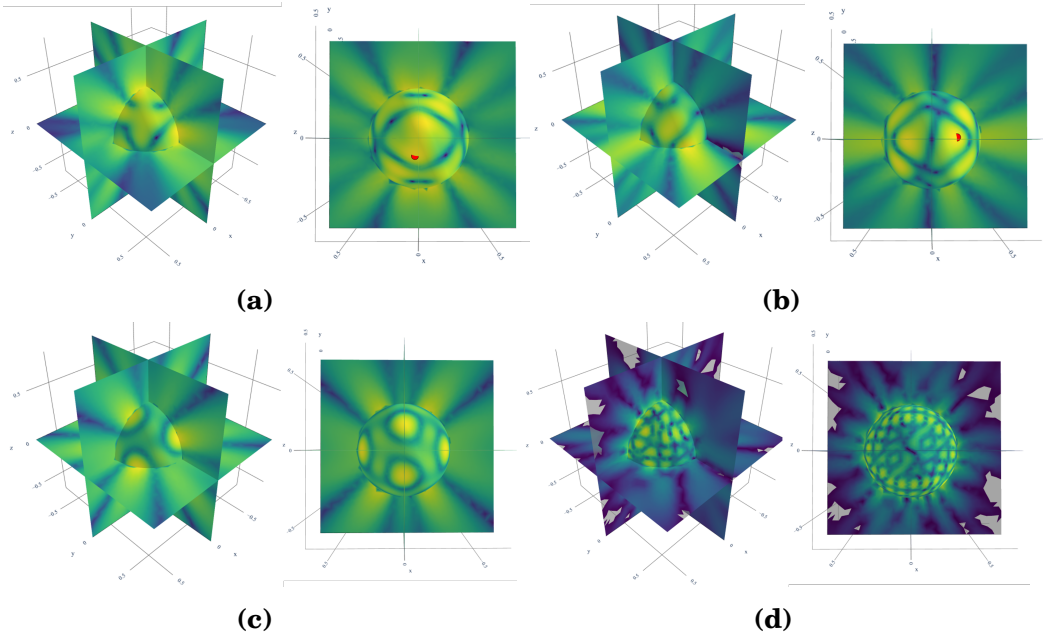

FIGURE 3.9 - *Pressure amplitudes on Γ_{obs} radiated by the i^{th} column of $\boldsymbol{Q}_2\boldsymbol{\Lambda}$ ($\boldsymbol{\Lambda}$ being defined by Eq.(3.3.3)); (a) $i = 1$; (b) $i = 10$; (c) $i = 100$; (d) $i = 250$ and $ka = 8.24$. Plots are displayed within a 30 dB dynamic range, and the red dot indicates the maximum level location.*

It can be stated from this graph that the optimized formulation of $\boldsymbol{\Lambda}$ drastically improves the convergence speed of Galerkin ESM. On this particular test case for example, the -13 dB error ratio is obtained for $K \approx 0.8(N_s - N) = 1027$ when $\boldsymbol{B}$ is only sampled from $\boldsymbol{Q}_2$ while the same accuracy can be achieved with $K \approx 0.4(N_s - N) = 513$ with the power oriented version of $\boldsymbol{\Lambda}$. This earning represents a significant reduction of the dimension of the inverse problem in Eq.(3.2.12) for practical applications of the method.

The blue lines assesses the point made above with Eq.(3.3.4): when the acoustic power oriented optimisation in Eq.(3.3.3) is used for the construction of $\boldsymbol{\Lambda}$, most of the acoustic energy is concentrated in the first coefficients of $\hat{\boldsymbol{d}}$ while at least 85% of them are required to reconstruct the same energy levels when $\boldsymbol{\Lambda}$ is simply the identity matrix.

3.4.4 Computational efficiency

Results above on the spherical test case were averaged on 25 runs of the code, 1.7 seconds per frequency were needed for the QR decomposition, 1.2 for the $\boldsymbol{\Lambda}$ calculation in Eq.(3.3.1) and 2.3 for the $\boldsymbol{GB}$ regularized inversion.

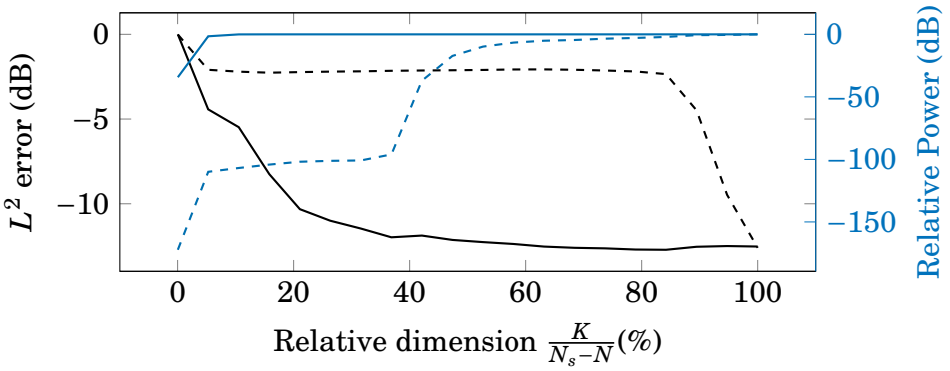

FIGURE 3.10 - *Reconstruction indicators for 10 correlated monopoles on a rigid sphere at $ka = 1$. In black is plotted the L^2 relative error, in blue is displayed radiated power from Eq. (3.3.4). Dashed lines features $\boldsymbol{\Lambda} = \boldsymbol{I}$ while solid lines were obtained with $\boldsymbol{\Lambda}$ sampled from the radiation efficiency operator.*

Given the results displayed in the current section, the fair comparison would be with iBF combined with realistic FRFs. Considering a generic test case, iBF itself is of the same complexity than the $\boldsymbol{GB}$ inversion but the FRF simulation has to achieved with FEM, BEM or classical ESM and it is likely that in the end the overall performance does not overrun Galerkin ESM.

3.5 Conclusion

In this chapter, the sketch of a new equivalent source technique named Galerkin ESM was discussed. From the idea of having equivalent sources as unknown of the acoustic imaging problem, the scattering component from classical ESM used in chapter 2 are extracted and merged to the inverse problem in the form of a preconditioner for the $\boldsymbol{p} = \boldsymbol{Hq}$ formulation.

This operation features a dissection of the $\boldsymbol{T}$ matrix and its QR decomposition, as its orthogonal eigen vectors are required to project the equivalent sources on a subspace where their acoustic radiation satisfies the boundary condition on the skin of the radiating object. Interesting displays of these eigen vectors were exposed. Galerkin ESM raises again the issue of the source physical support when performing three-dimensional imaging: it isadvocated that a relevant perspective for future works would rather be to investigate acoustic field synthesized by equivalent sources determined with imaging than drawing conclusions based on punctual sources on the discretized skin.

The recurrent test case of the spherical geometry is used again for academic validation, and GESM turned to perform much better than beamforming and Bayesian focusing with free-fieldFRF but slightly worse than iBF based on finely tailored transfer functions. Galerkin ESM thus stands out as an interesting alternative for arbitrarily shaped geometries where the simulation of accurate FRFs may be demanding.

In the chapter that follows, all the methods presented so far are put to the test on more complex test cases to provide a more industrial view on their applications.

CHAPTER 4

INDUSTRIAL VALIDATION & RESULTS

The concluding chapter covers the successive industrial cases under scrutiny in the course of this thesis. With a view to put to the test all the equivalent sources techniques depicted in chapter 2 & 3, it is organized as follows: first is checked the interest of using refined transfer functions in a standard wind tunnel framework featuring measurements of an artificial monopole supported by a car. Then is proposed the evaluation of aeroacoustic source models in ESM on simulated data. Lastly, Galerkin ESM is assessed with measurements brought back from the ECOBEX project.

4.1 Car mirror in a wind tunnel

The first test case is the one of an omnidirectional source placed in the vicinity of the left rear-view mirror of car. The model at issue concerns the entire car and is meshed with $N = 23406$ nodes, which is quite a large dimension to handle for common laptop. As a result, beamforming only is used for this case as iBF involves $N \times N$ $\boldsymbol{S}_{qq}$ matrices that would be too complex to manage from the computational standpoint. Two 100 microphone planar arrays located at $y = \pm 6.57$ meters on both sides of the car and one 160 microphone array located $z = 5.66$ meters above it were used for a 10 seconds measurement of the sound emitted by the source and scattered by the car. On Fig-4.1 is illustrated the overall set-up of the wind tunnel

test rig.

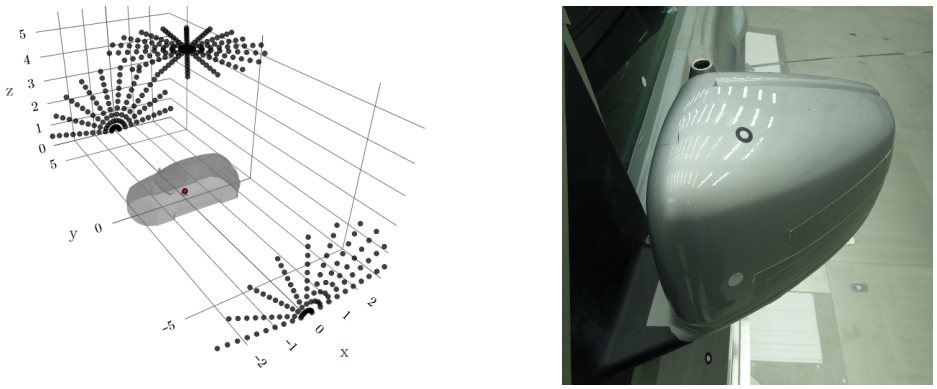

(a) **(b)**

FIGURE 4.1 - *Wind tunnel experimental set-up; (a) Disposition of the three planar arrays around the car, in red is exposed the source position; (b) Omnidirectional source at the top edge of the rear-view mirror.*

Time signals sampled at $f_s = 51200$ Hz are brought in the spectral domain thanks to the Welch (1967) process, featuring Hann windows and a 50% overlap between consecutive time blocks. On Fig-4.2 are plotted the resulting cross spectral matrices at 3 kHz for wind and no wind measurements, and with this information only it can already be inferred that scattering effects are of importance : the overall gap in pressure level between microphones facing the source (indices from 1 to 260, corresponding to top and left arrays) and those which are masked (indices from 260 to 360, right array) is of the order of 10 dB.

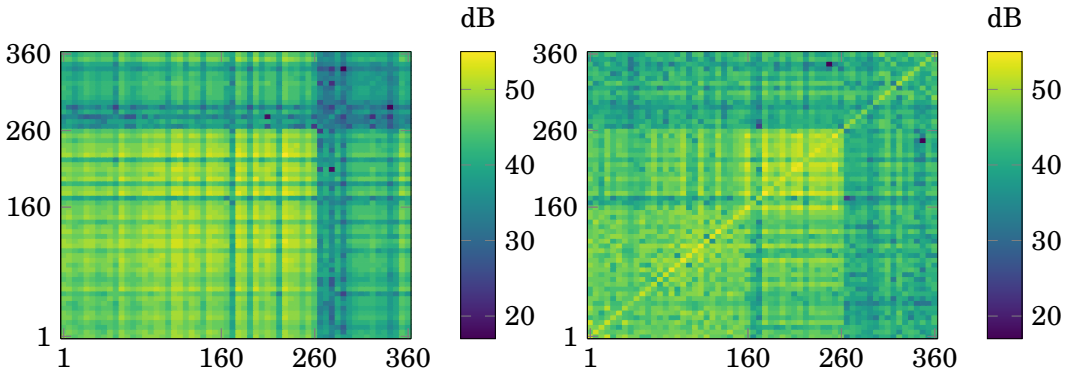

(a) **(b)**

FIGURE 4.2 - *CSM amplitudes of the combined three planar arrays at $f = 1000$ Hz, ordered as top, left and right with increasing indices; (a) No wind measurements; (b) $M_0 = 0.11$ measurements.*

Furthermore, the clear emergence of the diagonal levels on the right in Fig-4.2 emphases the apparition of uncorrelated noise on the microphones when the wind tunnel is activated. Additionally, the extra diagonal submatrices are mitigated with the wind, which results from the coherence loss between the arrays due to the turbulences in the shear layer. This phenomena was depicted by Ernst *et al.* (2016)

The relevancy of this first case regarding the developments proposed in the previous chapter lies in:

- The wind tunnel framework offers a promising set-up for practical three-dimensional imaging: combined planar array methods, ground reflections, scattering effects and shear layer refraction exposed in chapters 1 and 2 can be added to the transfer model and put to the test.

- The directivity of the source is known here (omnidirectional un baffled Q-source, see here for the technical documentation[1], which means that the inclusion of scattering effects in FRFs through ESM can be assessed independently from the choice between monopolar or dipolar models for unknown aeroacoustic source identification.

- The source was measured with a Mach number $M_0 = 0.11$ wind, and no wind at all. The previous point thus can be achieved first without worrying about correlation issues due to turbulences, and then can be tested the effect of wind on the accuracy gain due to ESM.

All in all, the purpose of the next two subsections is to illustrate how to use refined ESM techniques for monopolar FRF construction (as evoked in section 2.2) in a wind tunnel framework and seize the improvements with respect to the currently used free-field model.

It should be mentioned that the measurements took place in the DAIMLER Wind Tunnel Center in Sindelfingen (Germany) and the microphone time data involved in this section were all provided by M. Hironori Tokuno from DAIMLER.

4.1.1 ESM parametrization for industrial testing

The sensitivity of ESM to its settings is significantly higher on this type of geometry. Contrary to the spherical case used for validation, the normal velocity that

[1] https://www.qsources.be/simcenter-qsources/q-mhf-2/

has to be offset by the equivalent sources is subject to large variations and especially in the rear view mirror area. As no analytical formulation is available here to provide reference FRFs as in section 2.2.3, a *"blind"* criterion can be used to estimate the quality of the equivalent sources calibration without prior information on the correct transfer functions.

With the formalism of Eq.(2.2.4-2.2.7), the reasoning for such an evaluation can be put simply. Considering the incident pressure field of the unitary source on the i^{th} microphone position, the equivalent sources flow $\tilde{\boldsymbol{q}}$ are fixed normally with the pseudo-inverse of $\boldsymbol{T}$. A set of N_c *collocation* points is then defined on Γ as the barycentres of the mesh triangular elements and the normal velocity induced by the source at those intermediate nodes $\boldsymbol{v}^i_{n,c}$ is computed. The criterion δ_c is finally given by

$$\delta_c = \left\| \boldsymbol{v}^i_{n,c} - (-\boldsymbol{T}_c \tilde{\boldsymbol{q}}) \right\|, \tag{4.1.1}$$

where $\boldsymbol{T}_c \in \mathbb{C}^{N_c \times N_s}$ translates the flows to normal velocities transfer between the equivalent sources and the alternative discretization of Γ. δ_c can be understood as the quadratic error made on the compensation of incident normal velocity on the skin of the object. As it is computed on a different set of control points than the one used for the pseudo inversion, it is also a way to realise to what extend the ESM resolution sticks to the physical Neumann boundary condition.

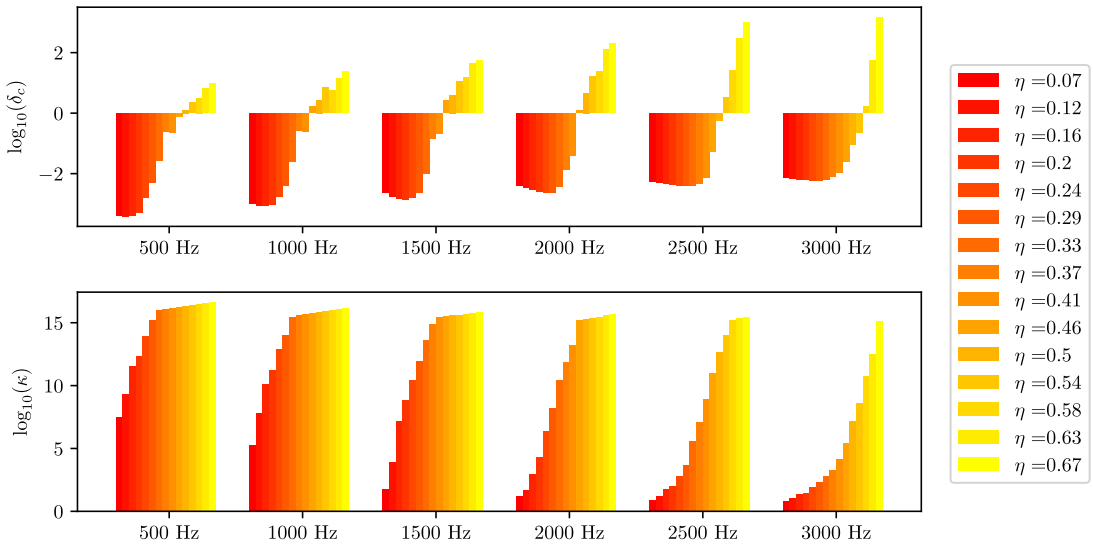

FIGURE 4.3 - *Comparative plot of δ_c and the condition number $\kappa(\boldsymbol{T})$ for various $\eta = \frac{N_s}{N}$ ratios at various frequencies.*

Insightful information emerges from the plots in Fig-4.3. Firstly it appears that the optimal number of equivalent sources with respect to δ_c differs from the

$\eta = 0.33$ ratio advocated for example by Dunn and Tinetti (2004). It seems indeed that using a constant value for η as it was often done in the literature does not present the best results, and that an adaptive ratio of equivalent sources between $\eta = 0.15$ at low frequencies and $\eta = 0.4$ at high frequencies may be more relevant.

The interpretation for this point can be put simply, as it exemplifies the reasoning on the conditioning of $\boldsymbol{G}$ and $\boldsymbol{T}$ presented in section 1.3.1: κ is somehow correlated with the groups of equivalent sources $\tilde{q}_{l_1}, \tilde{q}_{l_2}$ located in the near field of one another, i.e.

$$k \left\| \mathbf{r}_{l_1} - \mathbf{r}_{l_2} \right\| \ll 1,$$

as they mathematically have a similar role as columns of the propagation matrices. The number of equivalent sources may have to be upper bounded so that the amount of sources too close from one another could not exceed a fixed level.

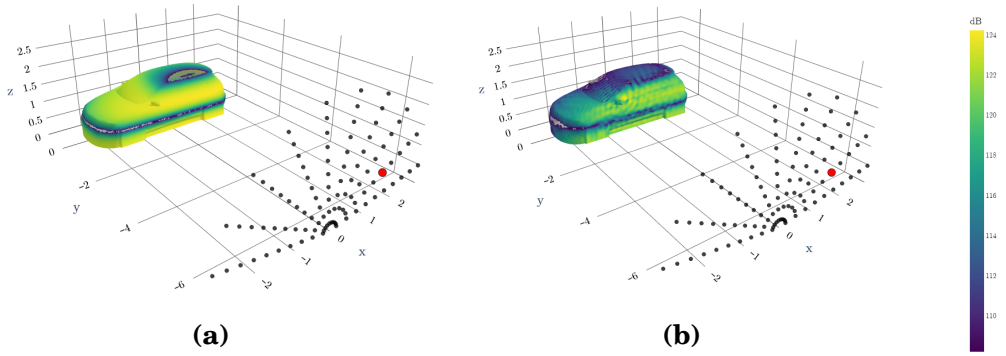

FIGURE 4.4 - *FRF amplitude between the* 85^{th} *microphone of the left array (red dot) and the car mesh at* $f = 1500$ *Hz and* $\eta = 0.25$*; (a) Free field; (b) ESM. The horizontal interferences are due to the ground reflections.*

Figure 4.4 presents an illustrative results of transfer function obtained with ESM and the process aforementioned. It highlights how shadowing effects are relevant even at medium frequencies, with the strong decrease in amplitude of the FRF on the car faces uncovered by the left array.

4.1.2 Imaging outputs

In this section are displayed a set of acoustic maps obtained with CBF and iBF with both free-field and ESM transfer functions at various frequencies. The latter are plotted within a 20 dB dynamic range for a clear exposure of the side-lobes patterns, and with absolute levels for confidentiality motives.

4.1.2.1 Q-source identification from no wind measurements

ESM is assessed first with the wind tunnel inactivated. The full CSM of the whole 360 microphones array was used to compute a 3D CBF with free field and ESM FRF both featuring image sources, for the results given in Fig-4.5 to 4.7.

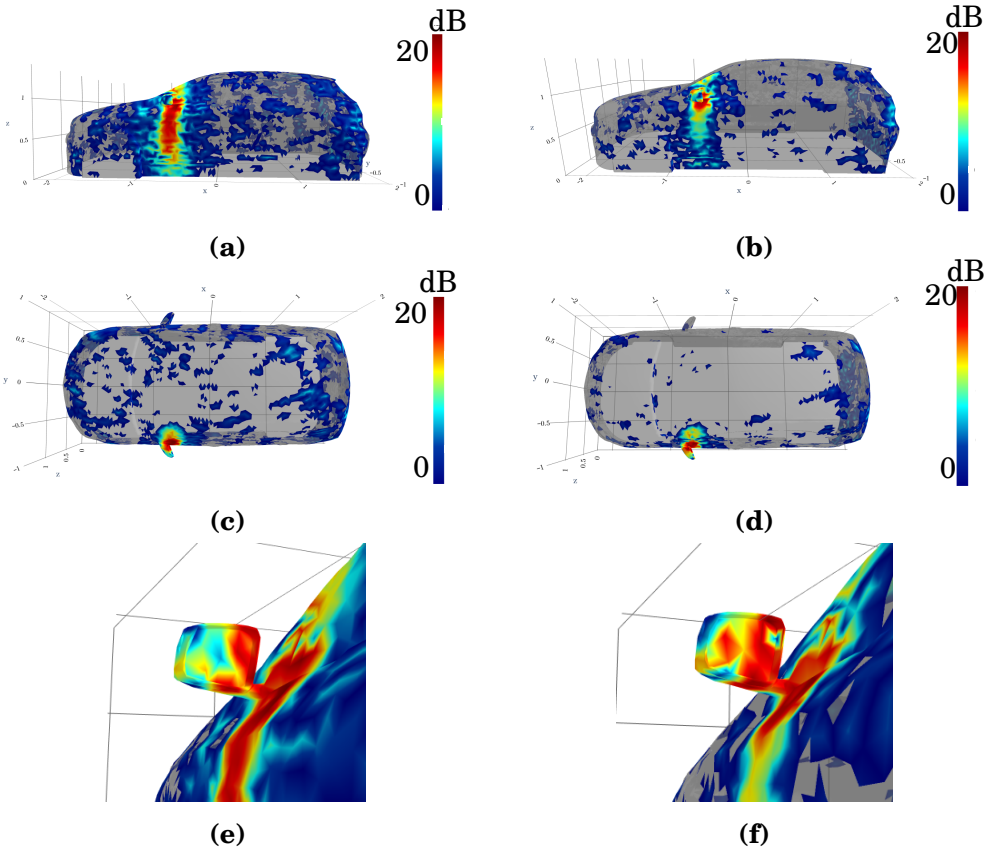

FIGURE 4.5 - *CBF maps from no wind measurements at $f = 3000$ Hz; (a,c,e) Free-field FRF; (b,d,f) ESM monopolar FRF.*

At high frequency where spurious side-lobes might hamper the proper reading of the source maps, ESM FRFs lead to clear improvement in terms of dynamic: planar arrays are less prone to spatial aliasing as the FRF gets more precise and becomes less invariant to translations (see again Fig-4.4). By doing so, sources fewer redundant sources occur from the beamformer point of view and the overall acoustic map is clearer. This is particularly highlighted with Fig-4.6-c and d where ESM enables to strongly discriminate the spurious sources on the windshield.

As expected, beamforming does not really perform well at 500 Hz but ESM still offers a slight compensation the inherent inaccuracy of CBF at low frequencies.

Another overall conclusion is that well known poor normal resolution of planar arrays is slightly attenuated when using refined FRFs. This can be observed on

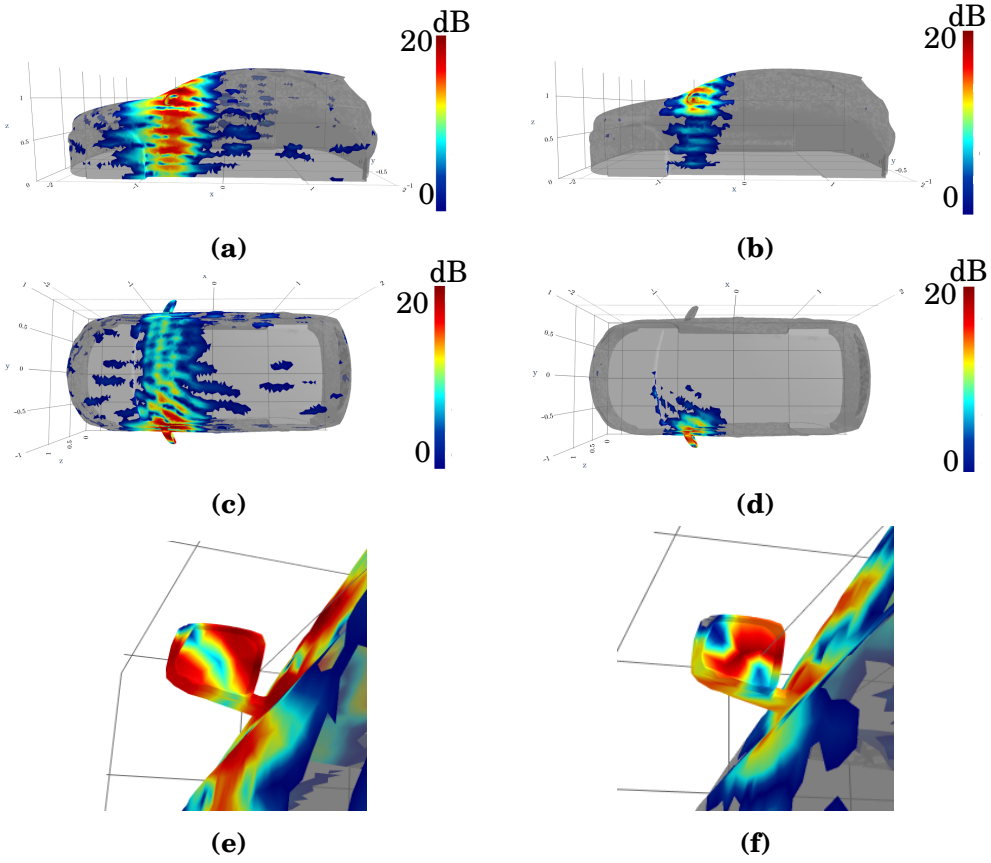

FIGURE 4.6 - *CBF maps from no wind measurements at $f = 1500\,Hz$; (a,c,e) Free-field FRF; (b,d,f) ESM monopolar FRF.*

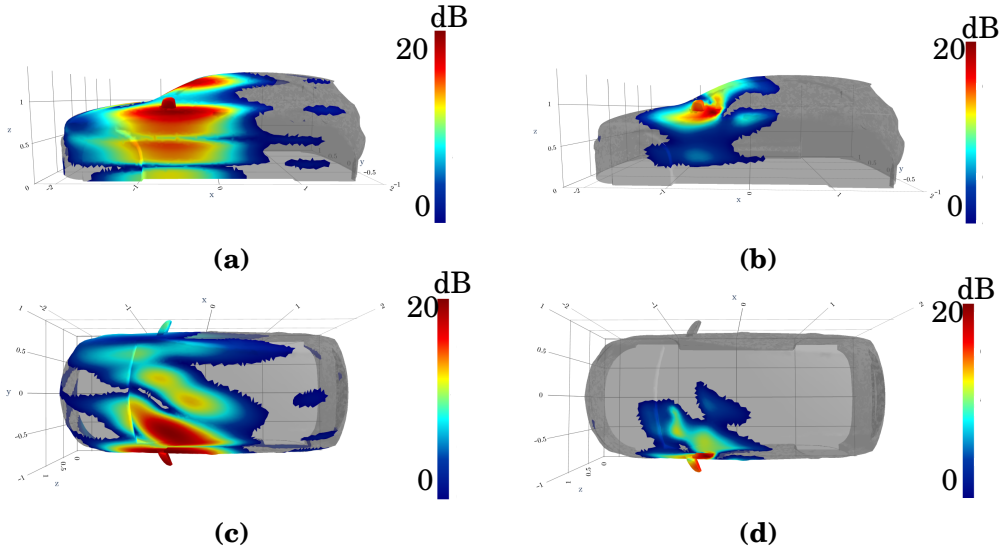

FIGURE 4.7 - *CBF maps from no wind measurements at $f = 500$ Hz; (a,c) Free-field FRF; (b,d) ESM monopolar FRF.*

(a) and (b) sub-figures where the extended source area along the z axis below the actual mirror source could origin misleading interpretations on a day-to-day industrial case where the ground truth sources location is unknown.

4.1.2.2 Q-source identification from Mach 0.11 measurements

The same free-field against refined FRF comparative study may now be led with the wind tunnel activated. The set-up and measurement parameters remain the same, but a Mach number $\boldsymbol{M}_0 = (0.11, 0, 0)$ is now considered as well as a refracted shear layer corresponding to the wind tunnel nozzle dimensions ($y = \pm 3.57$ m, $z = 4.2$ m). The diagonal removal routine is applied here to the CSM for denoising, and the ESM computation features the Amiet modification presented in section 2.4.2 to deal with the refraction.

Conclusions based on these beamforming maps do not significantly differ from those displayed in the previous section and the ESM approach achieves the strongest localization performance, and results are actually better at 3000 Hz as diagonal removal nullified every uncorrelated noise from the measurements. At 500 Hz, it seems with Fig-4.10 that ESM helps the genuine source to emerge from noise and the side lobes, but it is clearly not a strong enough step in the imaging process to produce a fully reliable acoustic map with this 20 dB dynamic range.

New sources emerge at lower frequencies due to the flow impinging the car, mainly on the door pillars, the rear-view mirrors and the bumper, but both FRF types exhibits the mirror with the Q-source as the prevailing one by more than

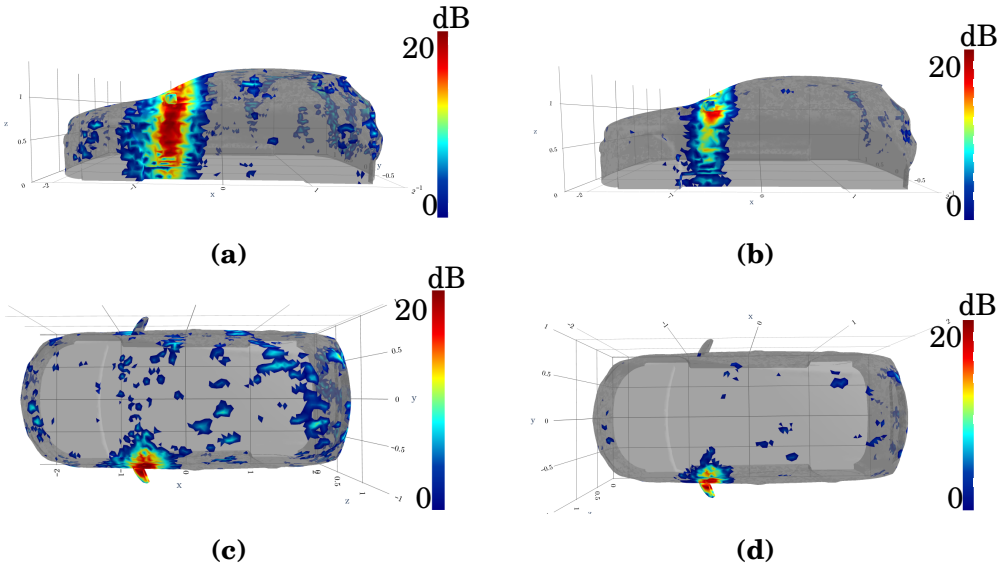

FIGURE 4.8 - *CBF maps from $M_0 = 0.11$ measurements at $f = 3000$ Hz; (a,c) Free-field FRF; (b,d) ESM monopolar FRF.*

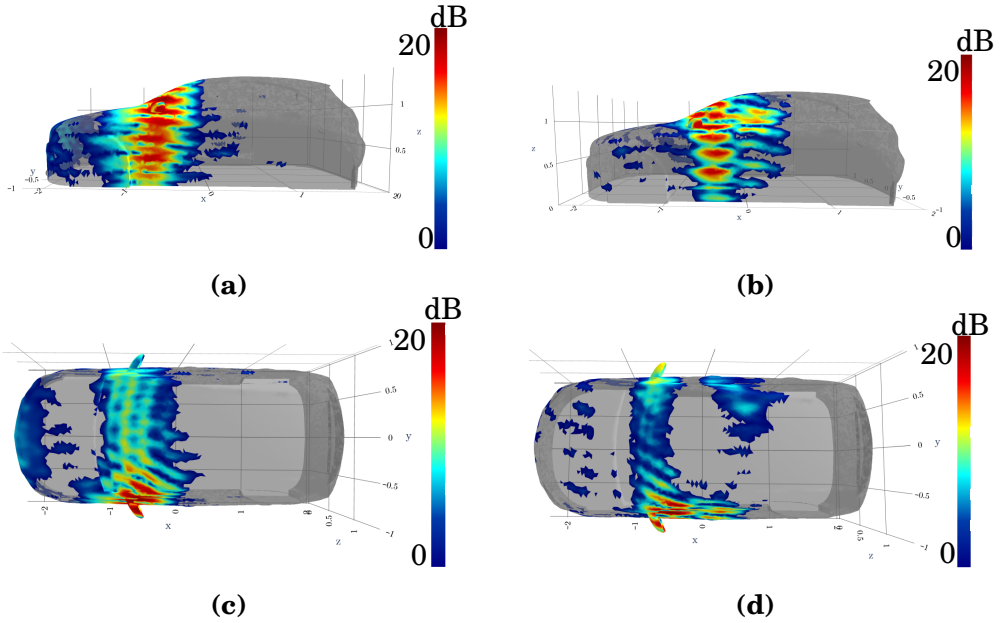

FIGURE 4.9 - *CBF maps from $M_0 = 0.11$ measurements at $f = 1500$ Hz; (a,c) Free-field FRF; (b,d) ESM monopolar FRF.*

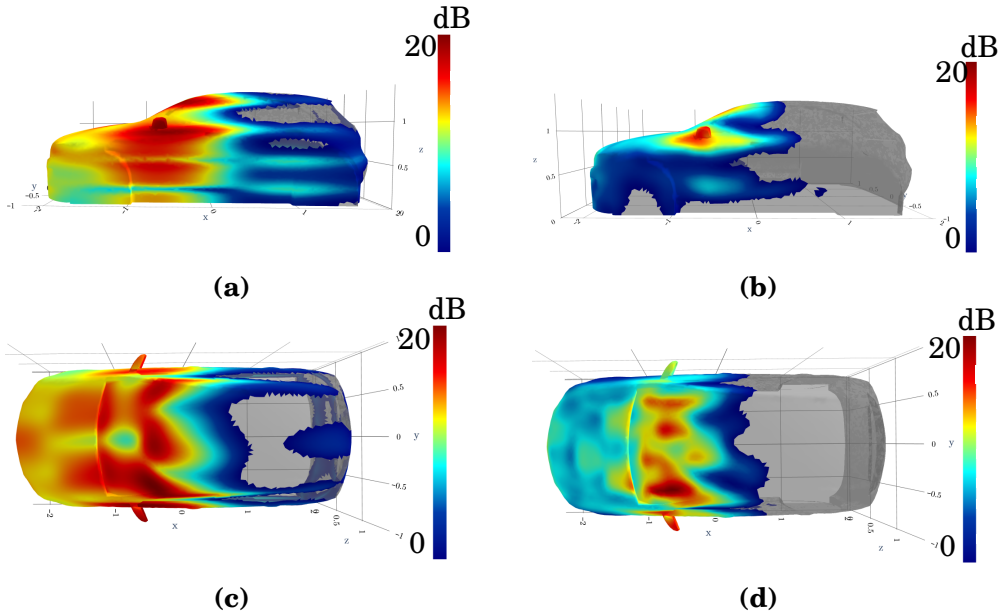

FIGURE 4.10 - *CBF maps from $M_0 = 0.11$ measurements at $f = 500$ Hz; (a,c) Free-field FRF; (b,d) ESM monopolar FRF.*

10 dB. Such a dynamic is actually consistent as the source was calibrated to produce sounds levels more than 12 dB higher than the acoustic levels recorded from purely aeroacoustic measurements.

4.2 Source identification from CFD data

As exposed in the previous section, the identification of aeroacoustic sources remains prone to a wide range of external issues: ground and wall reflections, shear layer decorrelation, flow-induced noise, etc. The purpose of the current one is to question now the sensitivity of aeroacoustic imaging to the sources nature implemented in the FRF model. The emphasis is put on the comparison of source maps obtained with convected monopolar and dipolar FRFs, and the assessment of ESM modifications presented in section 2.3.

From that perspective, a relevant alternative to wind tunnel measurements are time signals based on Computational Fluid Dynamic (CFD) as it allows a complete control of the acoustic environment: large number of microphones well positioned in the flow, no shear layer, and no facility effects in general.

4.2.1 Idealised Side Mirror

The first test case is an Idealized Side Mirror (ISM). It consists in a half cylinder topped with a quarter sphere. This model is already partly studied in the literature, Wang *et al.* (2010) investigated this geometry and achieved to propagate the far field pressure at $M_0 = 0.11$ using LES and BEM. More recently, Pan *et al.* (2020) did the same and shown interesting radiated pressure maps then supplied to a vibroacoustic software for the evaluation of the resulting noise in the car's cabin.

The ISM under scrutiny here is displayed on Fig-4.11. It notably features three small design flaws on its side and its top to trigger interactions with the flow and get closer to a genuine side mirror. The corresponding mesh features $N = 5506$ nodes for a characteristic length L equal to 0.3 meters.

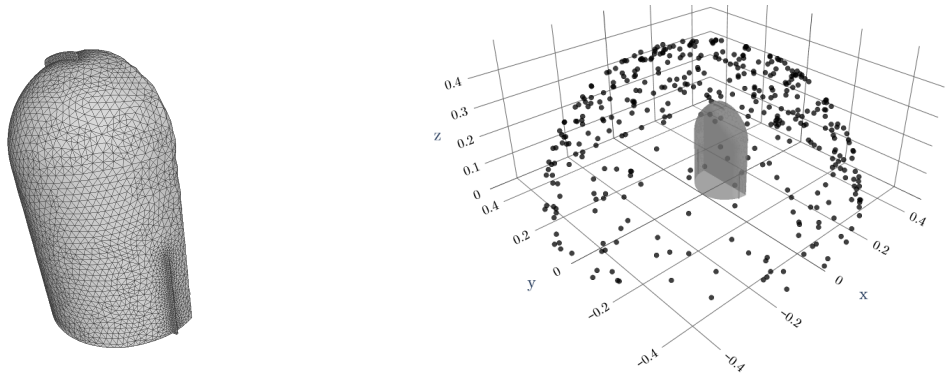

(a) **(b)**

FIGURE 4.11 - *Idealized Side Mirror geometry; (a) Triangular mesh of the modified ISM with top and side flaws; (b) Simulated microphone positions for the CFD computation. The wind direction is set along the positive x axis.*

The microphone array is a cloud of $M = 400$ points randomly distributed on a hemisphere of radius $a = \frac{5}{3}L$ fully covering the ISM. Its geometry is set randomly, but the high number of microphones yields good performances in terms of sidelobes as exposed on Fig-4.12. On this figure are displayed the free-field Point Spread Function (PSF) on a plane centred on the barycentre of the ISM.

From these figures it is clear that almost no sidelobes is likely to blur CBF maps on this case under the 12 dB dynamic.

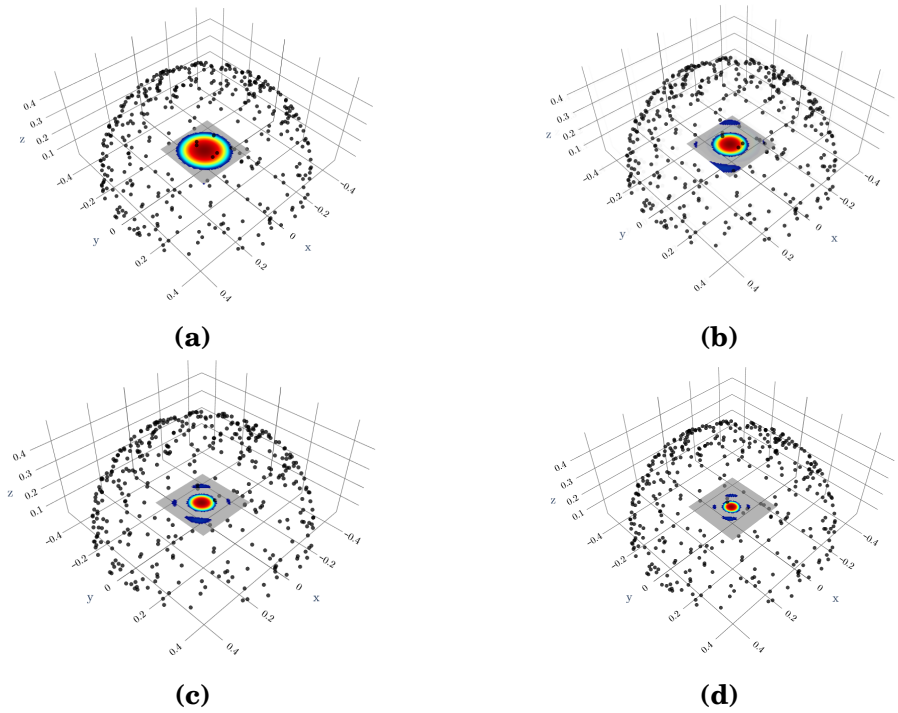

(a) **(b)** **(c)** **(d)**

FIGURE 4.12 - *Point Spread Function of the ISM array geometry (within a 12 dB dynamic range) on a plane for convected FRFs; (a) f = 1000 Hz; (b) f = 1500 Hz; (c) f = 2000 Hz; (d) f = 300 Hz.*

4.2.1.1 CFD data overview

The temporal signals associated to each microphone is computed using the Acoustic Perturbation Equation (APE) available in Siemens (2021) software Star CCM+. APE pertains to finite difference approaches designed by Ewert and Schröder (2003) that allows to predict the acoustic perturbations related to the ISM geometry and propagate them directly toward the array.

The CFD outputs take the form of 0.3 seconds time signals sampled at $f_s = 25$ kHz. For the Cross Spectral Matrices (CSM) computation, a Welch periodogram is used again with Hann windows and a 50% overlap between snapshots. As exposed on Fig-4.13 and in adequacy with the results obtained by Pan *et al.* (2020), no particular frequency emerges from the ISM geometry in terms of acoustic radiation.

On Fig-4.14 can be observed the pressure levels from the APE simulation in the frequency domain. The trend seems to be that the low frequency component of the signal corresponds to extended source distribution on the mesh with maximum levels downstream, while at higher frequency the energy gets concentrated on the small flaws impinged by the flow (and in particular the top one).

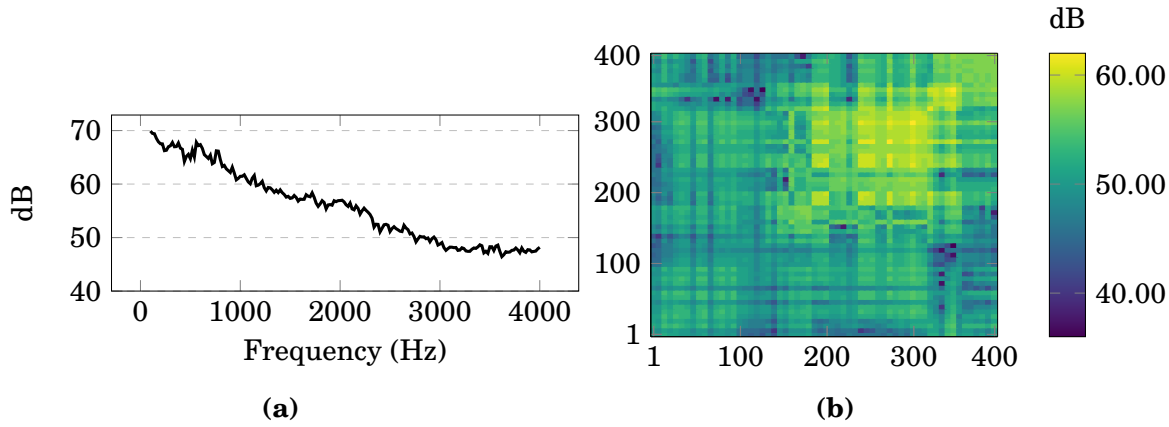

FIGURE 4.13 - *CFD issued spectra on the array for the ISM at* $M_0 = 0.11$*; (a) average autospectra on the 400 microphones; (b) CSM at* $kL = 10$ *Hz.*

The settings of the ESM process on that case is achieved in accordance with the routine advocated in chapter 2 and on the previous case in the wind tunnel: the η ratio for the source number is the one with the lowest δ_c regarding the frequency and they are randomly placed inside the mirror. From Fig-4.15 it can be stated again that the masking effect is significant on this geometry as well. It should also be noticed that the surface display of dipolar transfer functions cannot be exhibited in a straightforward way as the radiation from the dipole on the red dot is oriented differently for each node of the mirror mesh.

Despite the use of Evans *et al.* (2019) *half dipole* spatial filtering, the introduction of dipolar directivities still leads to large variations of the FRFs. Considering for instance a grid point on the rear side of the top flaw, its acoustic transfer with the front microphones is not taken into account because of the half dipole directivity, while the transfer with the rear part of the array is weak because of the masking effect of the ISM body. The phenomena is emboddied with Fig-4.16.

Consequently, it is advocated in this thesis not to use the conventional formulation of beamforming when using dipolar transfer functions because of the too steep normalization of the source level in Eq.(1.2.2) :

$$\forall j \leq N, \quad \left|q_j\right|^2 = \frac{\boldsymbol{H}_j \boldsymbol{S}_{pp} \boldsymbol{H}_j^{\mathsf{H}}}{\left\|\boldsymbol{H}_j\right\|^4}. \tag{4.2.1}$$

. The $\|\cdot\|^4$ in the denominator indeed tends to become unstable when supplied with FRFs like the rear node one in Fig-4.16 and drastically amplifies any numerical noise occurring in the process. In the next section, every beamforming source

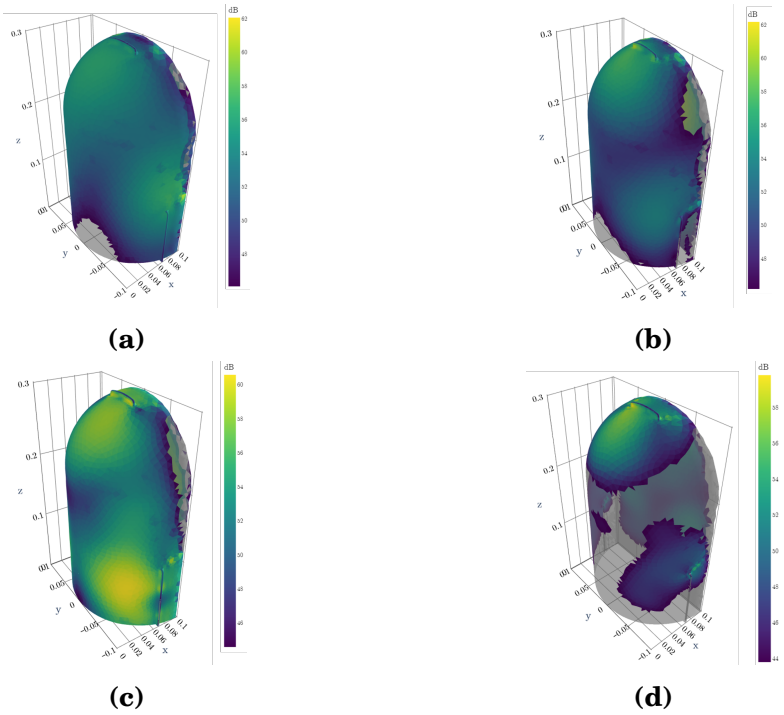

(a) **(b)** **(c)** **(d)**

FIGURE 4.14 - *Element-wise surface pressure PSD on the ISM at* $M_0 = 0.11$*; (a)* $kL = 14$*; (b)* $kL = 21$*; (c)* $kL = 28$*; (d)* $kL = 42$*. 16 dB dynamic range.*

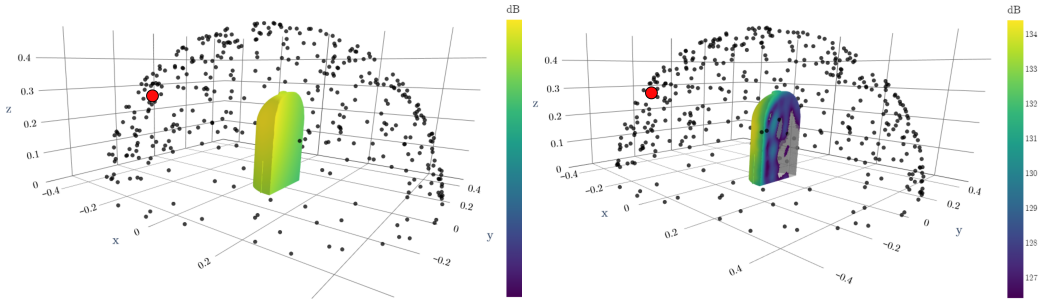

(a) **(b)**

FIGURE 4.15 - *FRF amplitude between the* 357^{th} *microphone (red dot) and the ISM mesh at* $kL = 10$*; (a) Monopolar free field; (b) Monopolar ESM.*

map were obtained with the coherence steering vector presented at the end of section 1.2.1. This option is relevant when working with simulated signals as they are noise-free and do not require the diagonal removal step. It could also mentioned that the accurate spatial localization of the sources is sought more than their quantitative levels on such a test case where the aerodynamic profile of the mirror is at stake.

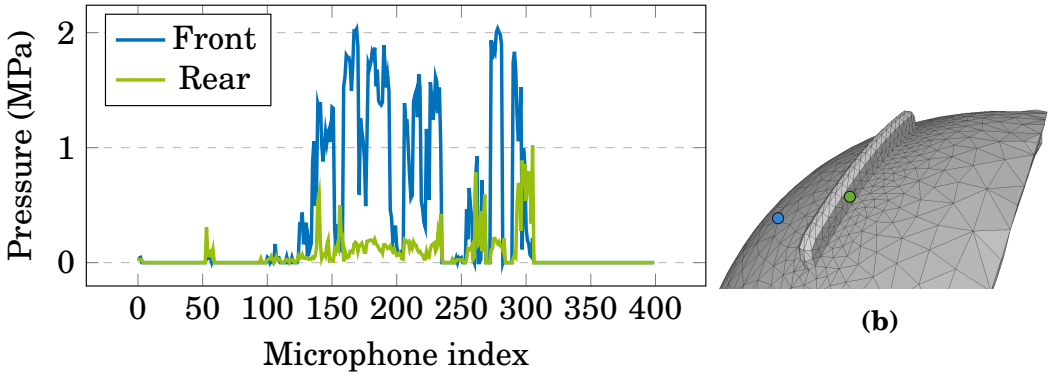

FIGURE 4.16 - *(a) Dipolar ESM FRF amplitude (pressure at the microphones considering unitary sources on the nodes) between a front (blue line) and rear flaw node (green line) and the 400 microphones at $kL = 42$; (b) Location of the nodes on the ISM mesh.*

4.2.1.2 Imaging results

From Fig-4.17 it can be inferred that all four models yield to slightly different interpretations. According to the monopolar output maps on the left, noise sources are not specifically related to the presence of the flaws in contradiction with the results on the right that features the directive source model. In both cases, the intermediate use of ESM can be associated to a resolution improvement. A common ground is the main lobe located on the rear face of the mirror, which is consistent with the results of Pan *et al.* (2020) where most of the energy is concentrated downstream.

At a higher frequency on Fig-4.19 the conclusions differ: both monopole approaches indicate that the sources are located upstream to the additional flaws. Having in mind the surface pressure exposed in Fig-4.14-(b), such a conclusion is decent but misses the actual fine pressure maxima located on the edge of the top and side flaws. From that perspective, dipolar models could offer a complementary interpretation but it appears that beamforming poorly handles directive FRFs in that case.

A solution to avoid the hazardous relationship between beamforming and singular steering vector is to switch to Bayesian Focusing and invert the full $\boldsymbol{H}$ matrix. Following the guidelines of Le Magueresse (2016), the sparsity parameter of iBF is set to the default value $p = 1.3$ while the initial spatial aperture is chosen uniform. The main benefit from iBF here is an interesting focalisation of the

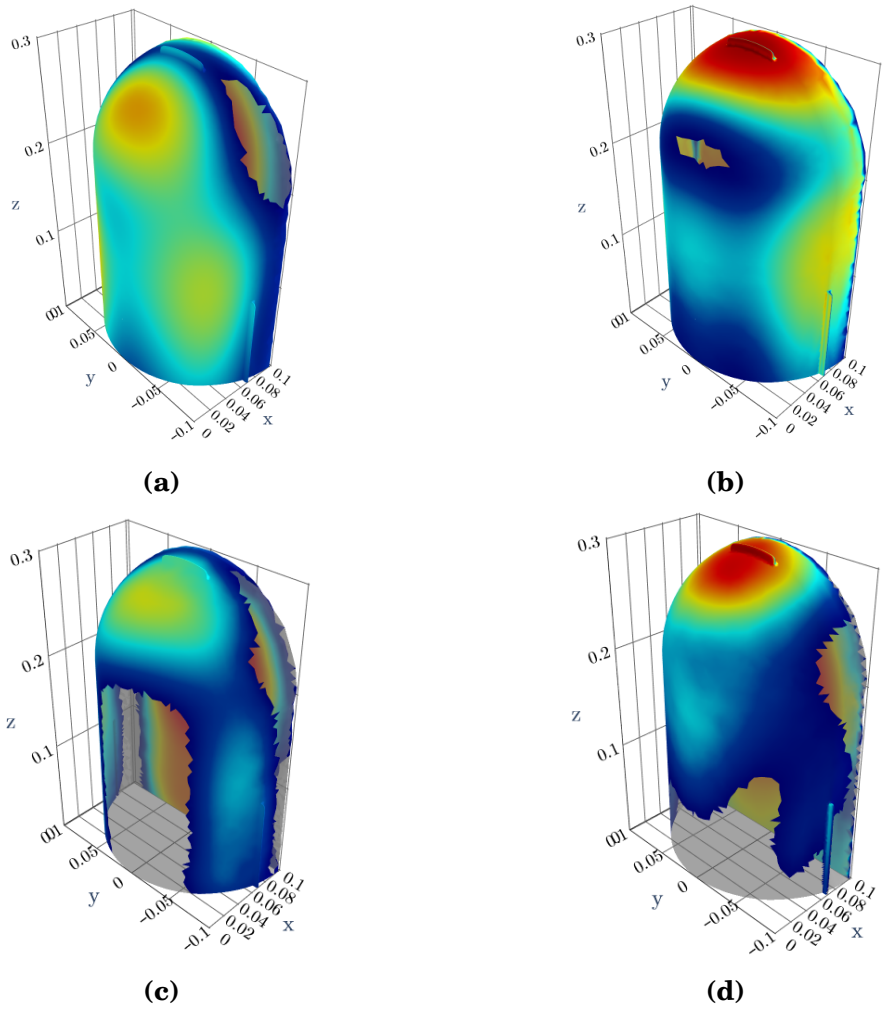

FIGURE 4.17 - *Coherence beamforming maps at $kL = 21$, within a 12 dB dynamic range. (a) Free-field monopolar FRF; (b) free-field dipolar FRF; (c) ESM FRF; (d) dipolar ESM FRF.*

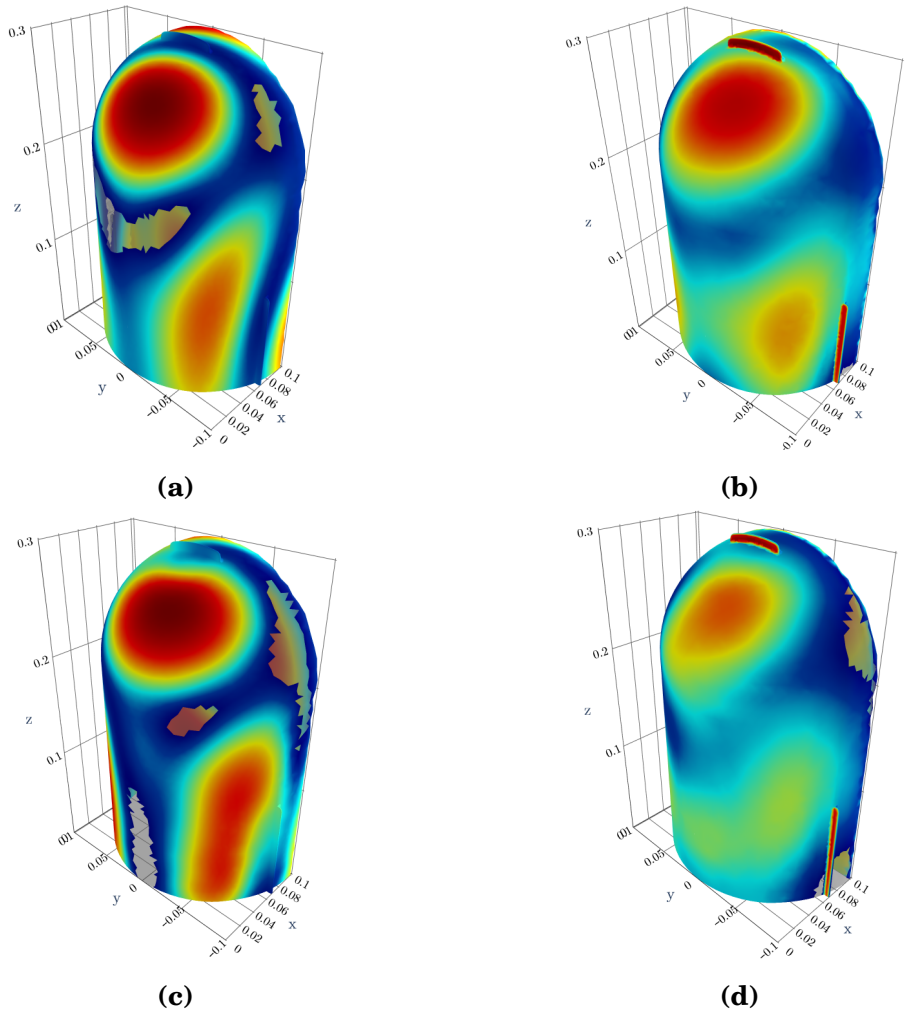

FIGURE 4.18 - *Coherence beamforming maps at $kL = 28$, within a 12 dB dynamic range. (a) Free-field monopolar FRF; (b) free-field dipolar FRF; (c) ESM FRF; (d) dipolar ESM FRF.*

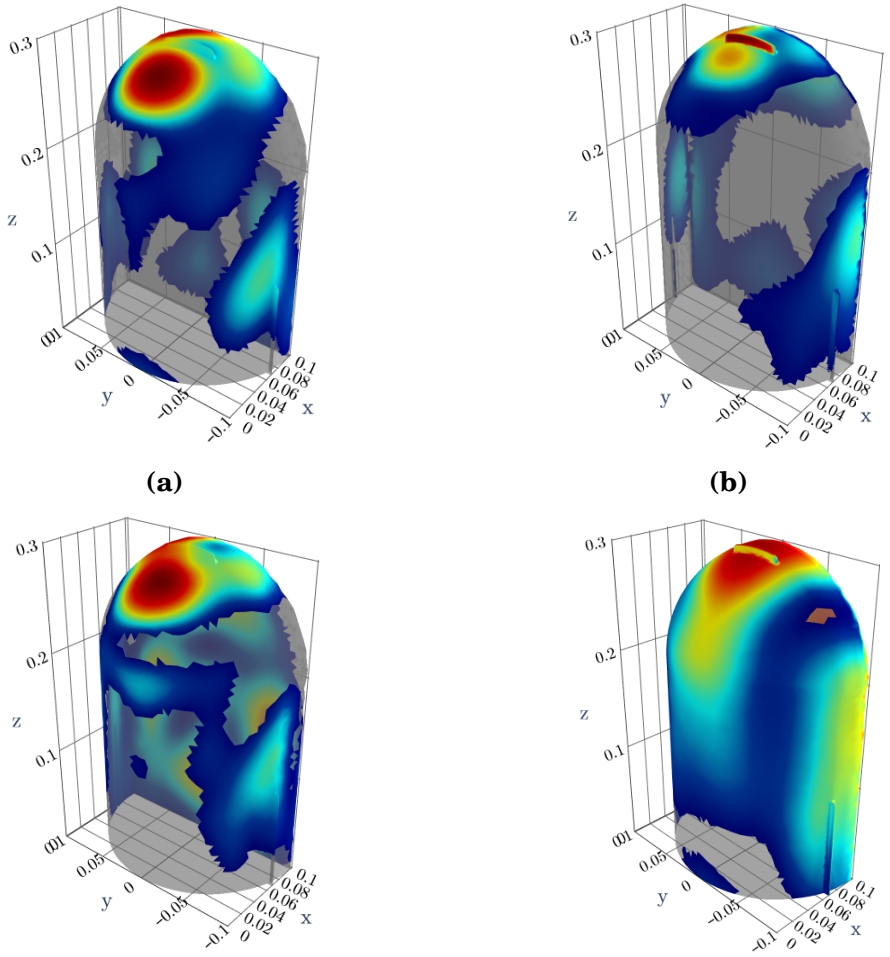

FIGURE 4.19 - *Coherence beamforming maps at $kL = 42$, within a 12 dB dynamic range. (a) Free-field monopolar FRF; (b) free-field dipolar FRF; (c) ESM FRF; (d) dipolar ESM FRF.*

dipolar sources on the flaws of the ISM, that are completely invisible from the monopolar point of view. The noticeable difference between maps on Fig-4.20 and Fig-4.21, c and d subplots, is striking from that standpoint.

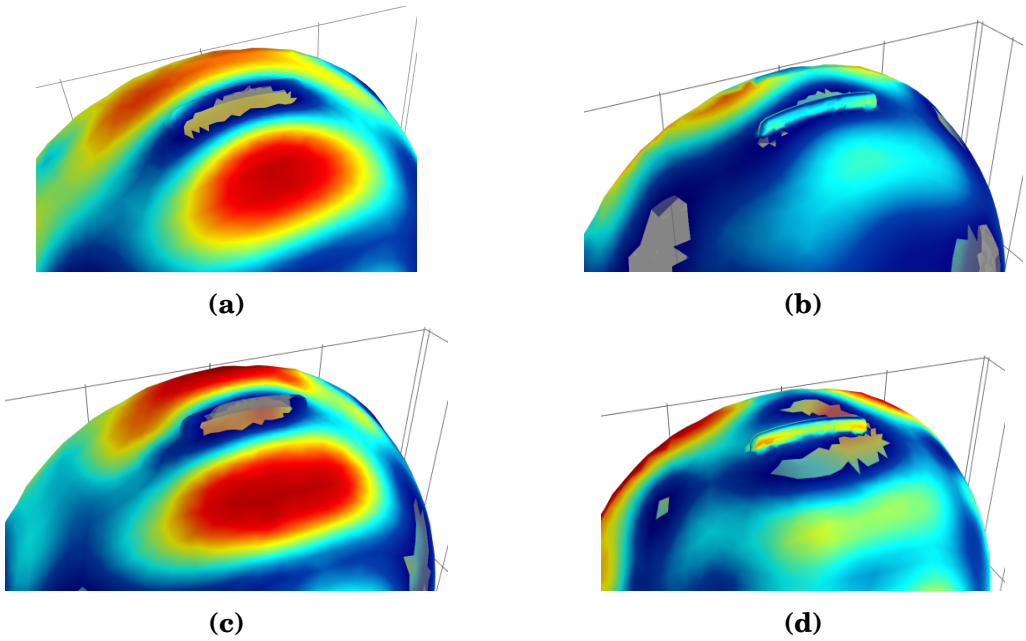

FIGURE 4.20 - *Iterative Bayesian Focusing maps at $kL = 28$, restrained to the top part of the ISM with a 20 dB dynamic range. (a) Free-field monopolar FRF; (b) free-field dipolar FRF; (c) ESM FRF; (d) dipolar ESM FRF.*

Overall, the ISM geometry turns out to be much trickier than the Q-source mounted on the car situation and the results above and the cautious outcomes can be summarized as follows:

- By setting the pressure surface as the target for acoustic imaging, the pragmatic interpretation of imaging maps obtained with purely monopole or dipole models is not fully efficient and leads to a model error reflected in the discrepancies between the surface pressure in Fig-4.14 and the imaging maps of Fig-4.17 to 4.19.

- Beamforming's interaction with dipolar and scattered dipolar FRFs yields insightful but doubtful sources distributions, and is sensitive to protruding angles of the three-dimensional grid.

- Switching to the use of an inverse method brings in additional informations on significant sources not identified with monopolar transfer functions,

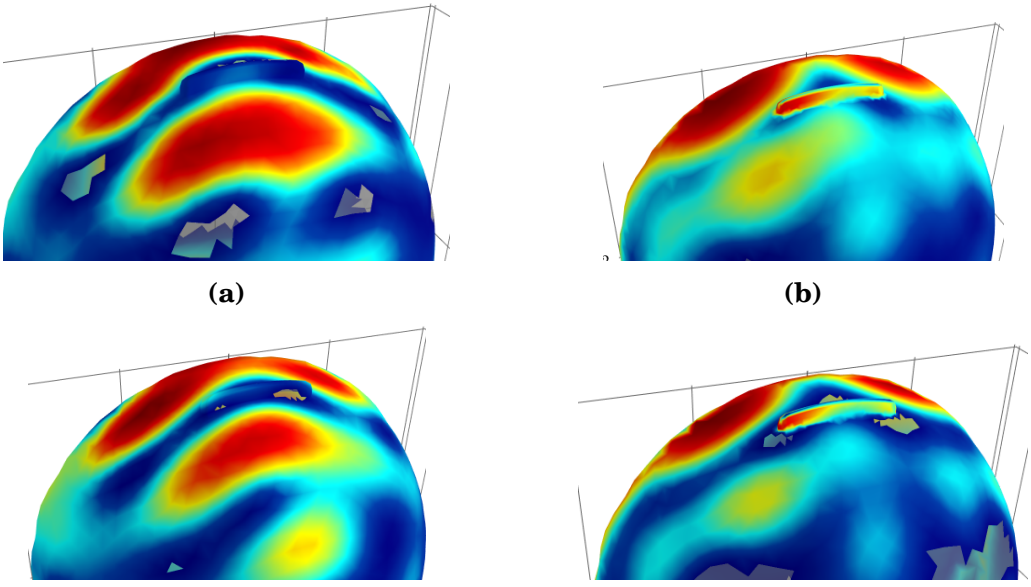

(a) **(b)**

(c) **(d)**

FIGURE 4.21 - *Iterative Bayesian Focusing maps at $kL = 42$, restrained to the top part of the ISM with a 20 dB dynamic range. (a) Free-field monopolar FRF; (b) free-field dipolar FRF; (c) ESM FRF; (d) dipolar ESM FRF.*

mainly related to the small ISM flaws. This a key step up as it precisely points out a particular geometric component of the mirror and offers a lead for a design refinement from the engineering point of view.

- Contrary to the previous test case, ESM contribution provides here a slight edge only and it is likely that the half dipole introduced by Evans *et al.* (2019) or Leclère *et al.* (2005) already account for most of the scattering component of the acoustic transfer.

4.3 Ecobex test bench

This last section lays out an experimental validation of Galerkin ESM. The aim of this final point is to gauge the behaviour of the method dealing with actual microphone array measurements on a large frequency range. The chosen case is a wooden mock-up flush mounted with monpolar sources, as described on Fig-4.22. The latter is modeled with triangular mesh of $N = 2377$ vertices.

Its characteristic length equals $L = 0.77$ meters, and the planar array features $M = 36$ analogical microphones placed at 12 centimetres from the sources plan.

Similarly to what was proposed in section 3.4, sources A and C were fully correlated while the last one (B) remained uncorrelated. The measurement is a 9.84 seconds record sampled at $f_s = 25600$ Hz.

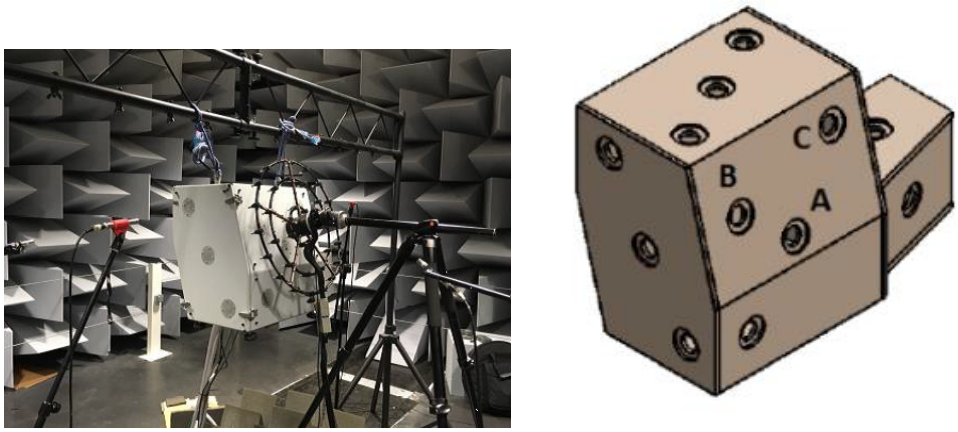

(a) **(b)**

FIGURE 4.22 - *Experimental set-up, from Le Magueresse et al. (2018). (a) Actual disposition of the array facing the source panel; (b) Disposition of the flush mounted sources.*

The session took place in a semi anechoic room with a locally treated ground, and array signals were post processed using the Welch periodogram with a Hann window. The block size was set to 2560 samples with a 50% overlap to reach a 10 Hz frequency resolution up to 12800 Hz.

Since no analytical transfer function is available for such a geometry, the relevance of this last section namely lies in this transfer function computation step : whatever the choice of the numerical method (ESM, BEM, FEM, etc.), computing transfer functions involves numerical resources and may induce additional errors for complex meshes, especially when it comes to propagate the identified sources toward observation planes. The Galerkin ESM could be seen as an alternative method that includes scattering effects in the model while bypassing this transfer simulation step. The numerical modelisation of the set up is exposed on Fig-4.23.

Results on that case were undertaken with two distinct approaches:

1. Classical three-dimensional source identification: comparatively to what was proposed in section 4.1 with the car test case, first is exhibited the interest of computing standard ESM FRFs for the identification and separation of the A, B and C sources on Fig-4.22.

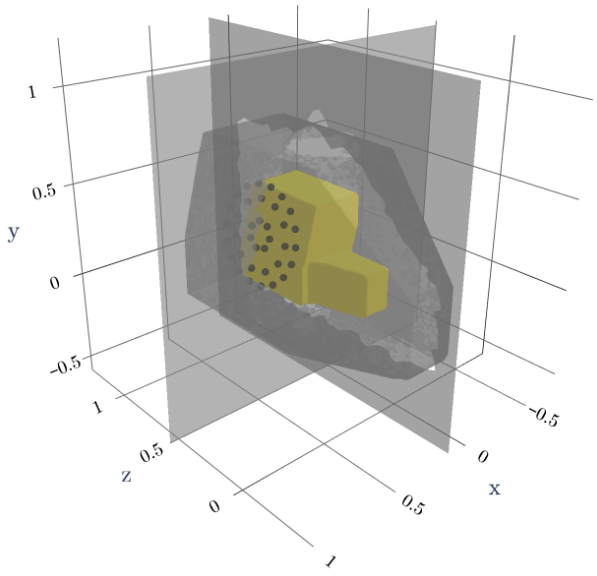

FIGURE 4.23 - *Numerical set-up for Ecobex test rig. The yellow surface is the control point support* Γ*, the transparent grey is* Γ_{obs} *and the 36 black dots represent the microphone array placed at 12 cm from the mock-up.*

2. Once the three sources identified, the process of repropagation and directivity reconstruction is engaged to assess Galerkin ESM.

4.3.1 Source identification

In this section are plotted the beamforming and iterative Bayesian focusing maps resulting from the set-up presented in Fig-4.22, using free-field and ESM simulated transfer functions, through the three-dimensional plots from Fig-4.24 to 4.26. Regarding the notations for iBF provided in the first chapter, the algorithm is used with a sparsity factor $p = 1.3$ as well as an uniform distribution for the initial prior for $\mathbf{\Omega}_{\boldsymbol{q}}$.

The conclusion based on beamforming maps does not really differ from the two previous sections of this last chapter: using the accurate FRFs brings additional dynamic to the source maps and tempers the poor normal resolution of the planar array by removing the misleading lobes on the opposite side of the mock-up.

When it comes to the inverse method, the benefits of ESM FRFs for the source identification is not significant on that case. This is likely due to the fact that Ecobex is an engine bench inspired mock-up where the array completely covers the genuine sources plane : from that perspective, the acoustic transfer is already

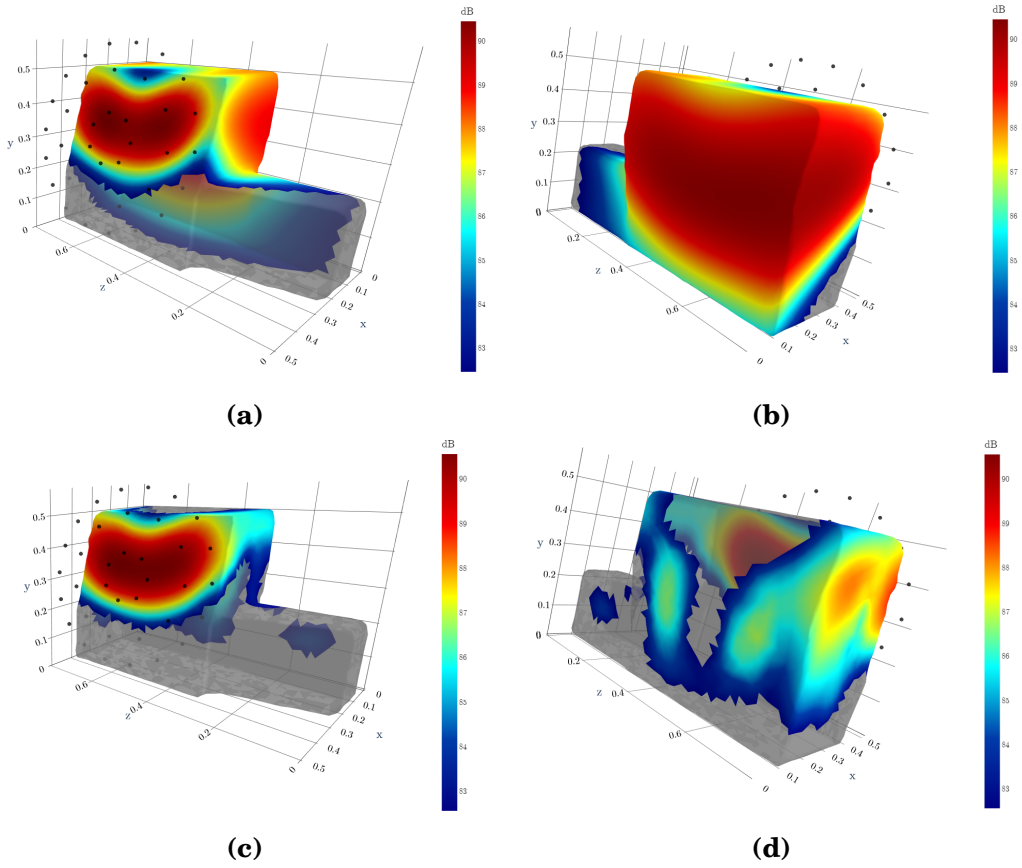

FIGURE 4.24 - *CBF on the Ecobex flush-mounted sources at $kL = 11$, within an 8 dB dynamic range; (a,b) Free-field FRFs; (c,d) ESM FRFs.*

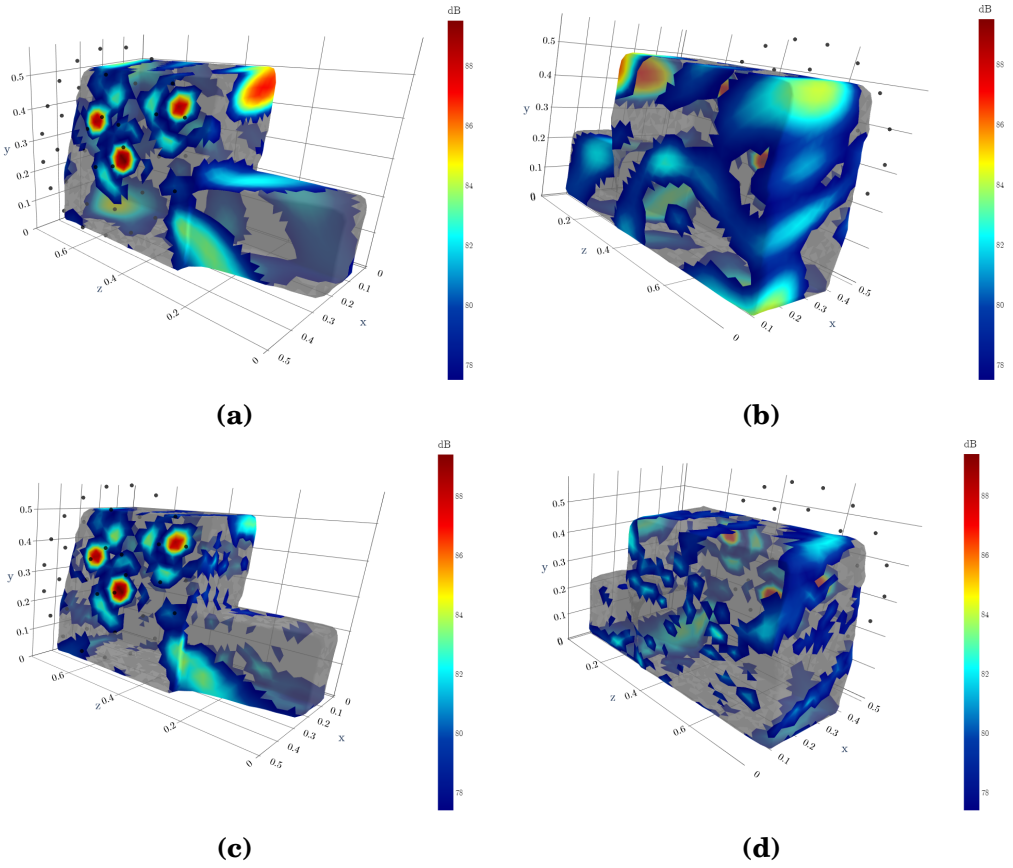

FIGURE 4.25 - *CBF on the Ecobex flush-mounted sources at $kL = 42$, within a 12 dB dynamic range; (a,b) Free-field FRFs; (c,d) ESM FRFs.*

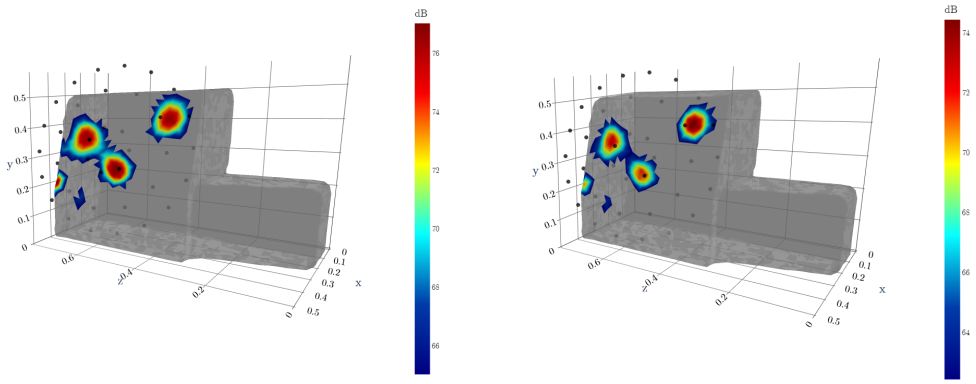

(a) **(b)**

FIGURE 4.26 - *iBF on the Ecobex flush-mounted sources at $kL = 11$, within a 16 dB dynamic range; (a) Free-field FRFs; (b) ESM FRFs.*

quite well approximated by the free-field model.

Finally from the source localization standpoint, it was shown that this study case benefits from refinements due to scattering inclusion only when CBF is used.

4.3.2 Directivity reconstruction

The synthesis of the sound field resulting from the three identified sources raises new challenge in comparison with the previous section :

- Correlation between sources lead to specific interference patterns.
- the diffracting behaviour of the mock-up may impact the directivity.

The conventional ESM approach is hardly an option here to simulate the transfer between the sources and the observation grid (i.e. the transparent grey mesh in Fig-4.23) given the large number of points in the discrete version of Γ_{obs}. Indeed, the process designed in section 2.2.2 based on the reciprocity principle was initially thought for FRF simulation between N grid points and M microphones assuming practical values for M much smaller than N. By applying it to the calculation of transfer functions between Γ and Γ_{obs}, such an assumption no longer prevail and computation times become prohibitive.

With a view to recover the sound field propagated by the three sources around the engine, The same methods used for the SRTF validation of GESM in the last section 3.4 of the previous chapter are applied here: CBF, iBF and Galerkin ESM, with the difference that this time only free field FRFs can be provided to the two first ones.

A display of the associated synthesized fields is given on Fig-4.27 to Fig-4.29, at a frequencies at which scattering effects are likely to be significant (kL ratio far greater than one).

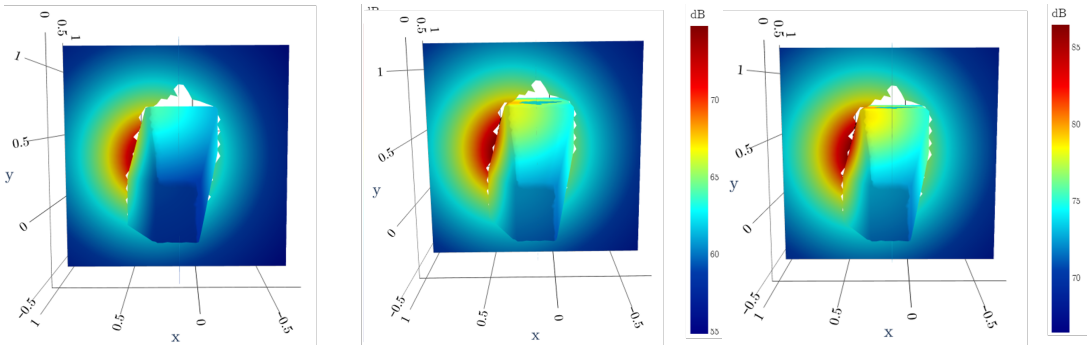

(a) **(b)** **(c)**

FIGURE 4.27 - *Acoustic pressure (amplitude) repropagated on Γ_{obs} (relative levels with a 20 dB dynamic range). Sound field propagated by sources identified with CBF featuring free field FRF; (a) $kL = 9$; (b) $kL = 21$; (c) $kL = 31$.*

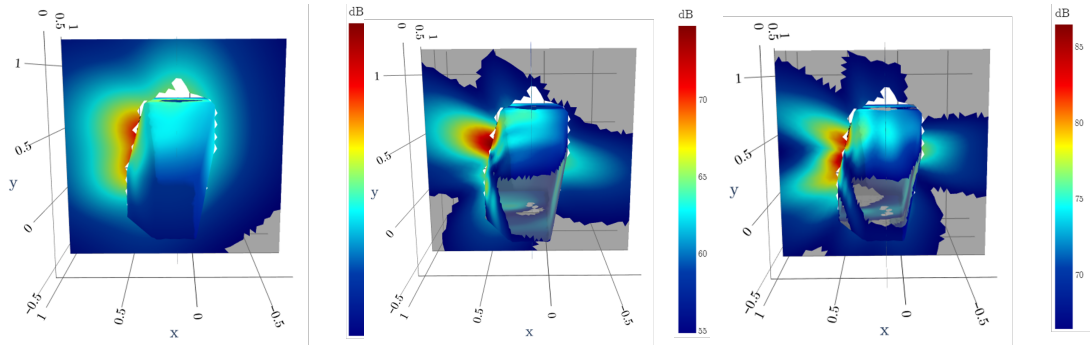

(a) **(b)** **(c)**

FIGURE 4.28 - *Acoustic pressure (amplitude) repropagated on Γ_{obs} (relative levels with a 20 dB dynamic range). Sound field propagated by sources identified with iBF featuring free field FRF; (a) $kL = 9$; (b) $kL = 21$; (c) $kL = 31$.*

Preliminary observations of these acoustic maps are enlightening. As expected CBF is unsuitable to seize the acoustic produced by the correlated sources A and C. iBF and Galerkin ESM are in accordance on the side of the face with the sources but differ on the part of Γ_{obs} with pressure levels scattered around the mock-up. At first glance it seems that the acoustic shadow zones caused by the presence of the wooden structure find its most faithful depiction with the Galerkin ESM synthesized pressure field.

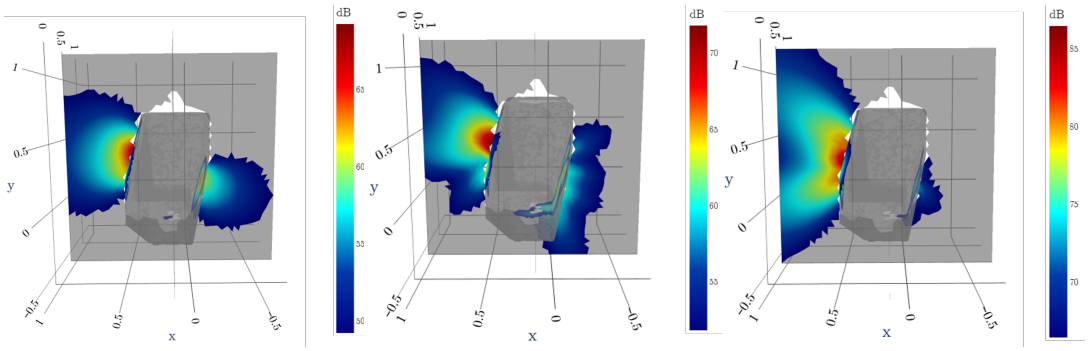

FIGURE 4.29 - *Acoustic pressure (amplitude) repropagated on Γ_{obs} (relative levels with a 20 dB dynamic range). Sound field propagated by sources identified with Galerkin ESM; (a) $kL = 9$; (b) $kL = 21$; (c) $kL = 31$.*

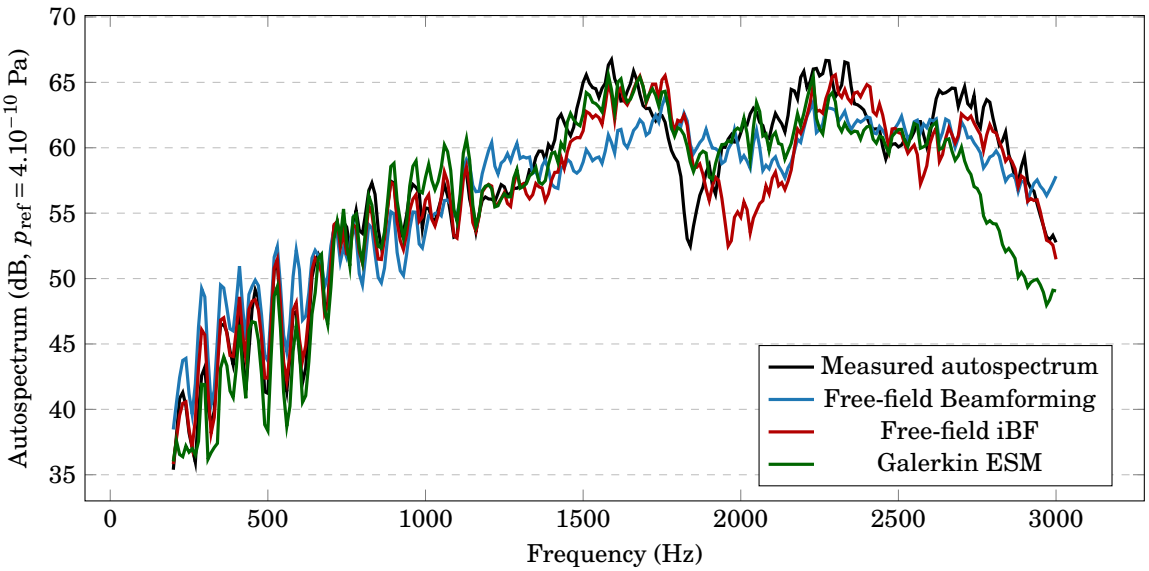

FIGURE 4.30 - *Repropagated levels at a reference microphone not included in the microphone array, within the $kL = 2.8$ to 48.6 frequency range.*

Another quantitative evaluation on the experimental case is displayed on Fig-4.30. It exposes the repropagated pressure level on reference microphone placed 12 cm in the alignment behind the array shown on Fig-4.22. For the sake of readability, the beamforming curve was post-processed by propagating only the three local maxima corresponding to the A, B and C points of the CBF map. At low ka numbers, all three methods yield a good adequacy with the measured level, with a small edge for iBF and Galerkin ESM. However, beamforming rapidly tends to be globally inappropriate as frequency rises and iBF is subject to discrepancies at specific frequency ranges compared to Galerkin ESM. With regard to Fig-4.29, this is consistent with the fact that acoustically masked areas in $\bar{\Omega}$ do differ between iBF and Galerkin ESM issued back-propagation because of the misleading free-field propagator. Lastly, this last plot gives a first empirical clue on the maximum frequency reachable with the chosen number of equivalent sources concerning our method (here approximately 1800 Hz). As for classical ESM, a sensitivity study must be conducted in further studies to define more precise guidelines on that specific issue.

4.4 Conclusion

Throughout this chapter, every refinements brought to ESM for FRF simulation were assessed on a set of application cases issued from industrial studies.

First the localisation of a positioned omnidirectional source with three planar arrays in wind tunnel was tested. Working with an already known source model subject to facility-related disturbances enabled to underline the interest of increasing the level of accuracy of the transfer matrix $\boldsymbol{H}$. To this end, ESM works out well and substantial improvement were exhibited for three-dimensional CBF both in terms of dynamic and resolution.

Then was adopted a different framework with the identification of aeroacoustic sources stemming from the impact of a low Mach number flow on a ISM based on CFD computed time signals. The aim was to investigate the comparative relevancy of four transfer functions models to get at the root of the geometry components responsible for the measured noise: monopoles or dipoles distribution on the skin of a rigid body inside a flow, with or without the coverage of scattering effects through ESM. Valuable observations could be made from the exposed results: both monopoles and dipoles provide relevant and complementary insights on the surface pressure, a specific care should be taken when using beamforming for

three-dimensional acoustic imaging with directive transfer functions. The greater degree of precision on high frequency pressure reconstruction is achieved when a dipolar ESM model was provided to an inverse method, at the cost of higher computation times that may not be worth in industrial processes as it stands.

Finally, an engine bench oriented situation was put under scrutiny to evaluate Galerkin ESM. The sound propagated by two correlated and one uncorrelated sources mounted on an mockup was recovered from a 36 microphone planar array. GESM repropagated maps provide insightful refinements on the sources directivity, especially compared state-of-the-arts methods.

CONCLUSION AND RESEARCH OUTLOOK

Conclusion

Prior investigations from the literature have queried diverse ways to improve array imaging performance of three-dimensional source distributions. The literature review on this topic outlined the main trends. Enhanced array geometries for 3D coverage is one of them, even though this is a lead often set aside because of the practical measurement constraints and the related costs from the hardware point of view. The academic community has also extensively explored beamforming and inverse problem algorithms, showing great results with planar array combination techniques or gridless approaches. Nevertheless, not much attention has been drawn on acoustic transfer functions as a vector for improvement and free-field models are still widely used.

The thesis has therefore addressed the challenge of propagation model enhancement by the mean of equivalent sources. On balance, the Equivalent Source Method proved to be at the same time a challenging and competitive method for frequency transfer function simulation. Starting with the original version of ESM assessed on an analytic FRF, several refinements were implemented all along this thesis. From the perspective of a future industrialization at MicrodB, improvements were proposed for the automation of ESM aiming at FRF simulation. Embedding diffraction, ground reflections and shear layer refraction in the FRFs, it enhances the dynamic range and prevent misleading sources usually occurring when planar arrays with poor normal resolution are used. Equivalent sources are generated randomly, and the ESM algorithm can be run to get more accurate FRFs than classical free field transfer functions. The optimal design for equivalent sources remains however the main blocking point for the full automation of ESM, even though the second and last chapters contribute to this subject : guidelines from previous research concerning the number of equivalent sources were nuanced throughout this work, and those about their best positioning were checked only.

Some links with the aeroacoustic analogy literature were also discussed. For the purpose of loading and thickness noise sources identifications in wind tunnels at low Mach numbers, convected monopoles and dipoles were included in the ESM process.

The FRF simulation approach was tested on genuine wind tunnel measurements as well as aeroacoustic datasets simulated with compressible CFD. Source maps concerning an ISM with aerodynamic flaws reveal that both monopoles and dipoles may constitute relevant and complementary insights on the surface pressure. A greater degree of precision on high frequency pressure reconstruction is achieved when a dipolar ESM model is provided to an inverse method. Therefore a specific care should be taken when using beamforming for acoustic imaging with directive transfer functions, notably to avoid the amplification of measurement of numerical noise during the inversion of locally null FRFs. When it comes to experimental data, the proper identification of an omnidirectional source on a strategic location of a car mesh was performed accurately with three-dimensional beamforming and ESM transfer functions. ESM modifications to account for refraction do not impact the overall performances of the FRF, and the conclusions drawn from the no wind beamforming maps remain.

Finally, Galerkin ESM was introduced in chapter 3 as a promising algorithm to reproduce sound fields scattered around diffracting bodies from array measurements. Inspired from both historical approaches and recent imaging references to ESM, algebraic manipulations to transcript a Neumann boundary condition as a matrix kernel inclusion was fully described, and integrated to the acoustic imaging inverse problem. A sub-process dedicated to the reordering of the kernel was also proposed to reduce the dimension of the resulting inverse problem, by maximizing the overall radiation efficiency of the equivalent sources. GESM was assessed experimentally in the last chapter, and it was demonstrated at this occasion to what extent the free field assumption becomes hazardous when it comes to repropagate pressure fields at high ka ratios. Since standard ESM is hardly an option of a sound field reconstruction purpose because of the computational cost, GESM provides an efficient framework to grasp strongly directive patterns while bypassing the FRF simulation step.

Outlook for future research

The avenues for further enhancements are numerous. Concerning the equivalent sources, their empirical case-to-case setting actually used for every ESM practical application is operational but time consuming and more consistant guidelines could be implemented. To this end, upstream research could be conducted on their optimization as an orthogonal basis for sound field reconstruction. Particularly, some links with the Wave Field Synthesis prior works on loudspeakers positioning for the propagation of arbitrary pressure fields could provide insightful indications on the best spatial distribution of equivalent sources (see for example Nicol, 1999). From the theoretical standpoint, the formalism of frames and Riesz basis offers interesting indicators to qualify equivalent sources distributions as mathematical bases.

As always with new acoustic imaging algorithms, extensive sensitivity studies could be led about Galerkin ESM. Notably, the interaction between GESM and three-dimensional array geometries did not pertain to scope of the thesis but it would be worth to sketch the method dependency to the array layout and whether it covers the entire source grid or not. From that perspective, the optimized principal surfaces showed in section 3.4.3 could provide enlightening informations on the key microphones positions with respect to the scattering geometry, and the emergence of MEMS and flexible arrays such as the MegaMicros used by Zhou *et al.* (2020) may enable their practical implementation.

As ESM mainly brings into play full matrices based on Green functions, major computational speed-ups for all the methods proposed in this thesis could be achieved through the use of Fast Multipoles Methods described for example by Coifman *et al.* (1993). Simply put, FFM would boil down to low-rank approximations of the propagation matrices by grouping sources considered close to each other from a far field observer. It could be used for the matrix/vector products involving $\boldsymbol{G}$ and $\boldsymbol{T}$ to significantly accelerate the SVD step of ESM and the QR decomposition in GESM, and the concept of a hierarchical clustering of the equivalent sources might help tackling the conditioning issues of $\boldsymbol{T}$ at low frequencies exposed in section 4.1.1.

For aeroacoustic applications, an in-depth study on a mixed monopole dipole approach would be physically relevant as the current process using one model

at a time might be oversimplified. Hajczak (2020, chapter 3-4) recently pointed out that the straight elimination of monopoles and quadrupoles from wind tunnel sound propagation at low Mach numbers could be questioned. Recently, Wang *et al.* (2022) concomitantly used loading and thickness noise sources in the ESM process and isolated their respective contribution to the far field propagated pressure. Achieving the same with array measurements and acoustic imaging would be a major milestone for aeroacoustic designs in wind tunnels.

PROCEEDINGS AND PUBLICATIONS

Two conference proceedings and one peer-reviewed article were produced as part of this thesis work:

Joannès Chambon, Thibaut Le Magueresse, Olivier Minck & Jérôme Antoni. 3D Beamforming for wind tunnel applications using ESM based transfer functions. In 8^{th} *Berlin Beamforming Conference*, 2020.

Joannès Chambon, Olivier Minck, Simon Bouley & Jérôme Antoni. Dipolar-based Equivalent Sources Method for 3D aeroacoustic source identification. In 9^{th} *Berlin Beamforming Conference*, 2022.

Joannès Chambon, Jérôme Antoni & Simon Bouley. Galerkin Equivalent Sources Method for sound field reconstruction around diffracting bodies. *Journal of the Acoustical Society of America 152*, 2022, pages 2042-2053, 10.1121/10.0014422.

APPENDIX A - DESIGN OF A SOURCE GENERATION ROUTINE

As a pre-processing step, it is clear now that a good control of equivalent source location is mandatory for ESM computation. In order to make the most of the available volume of the object without having alignments, the positions $(\boldsymbol{r}_l)_{l\leq N_s}$ of the sources define a random cloud of points inside the object surface mesh. A sorting is then processed to remove sources located in the potential gaps of the input mesh, or closer to the control points positions $\left(\boldsymbol{r}_j\right)_{j\leq N}$ than the chosen retreat distance.

Dirichlet Random sample as initial cloud of points

Every new source position is firstly defined by random barycentric coordinates with respect to all the control points:

$$\boldsymbol{r}_l = \sum_{j\leq N} w_j \boldsymbol{r}_j \quad \text{with} \quad \left(w_j\right)_{j\leq N} \quad \text{such as} \quad \sum_{j\leq N} w_j = 1. \tag{A.1}$$

For an uniformly distributed set, the random cloud array $\left(w_j\right)_{j\leq N}$ follows a flat Dirichlet distribution of order N and concentration parameter α/N, where α is a positive number defined by the user. Known as the generalization of the beta distribution, this choice is justified by the simple control it provides on the dispersion of the sources. With an expectancy and variance respectively given by

$$\forall j \leq N, \quad \mathbb{E}(w_j) = \frac{1}{N} \quad \text{and} \quad \mathrm{Var}(w_j) = \frac{1-N^2}{M(\alpha+1)}, \tag{A.2}$$

it appears that every $\boldsymbol{r}_l$ computed in this way will be in average located on the mesh barycenter, with a spacing inversely proportional to α. The Fig-A.1 illustrates this point on the cloud of points used for the rigid sphere diffraction presented in section 2.2.2.

At that stage, sources are by definition located inside the convex hull of the control points. Since the equivalent sources are supposed to be placed within the object, it remains thus to deal with more complex mesh, comporting cavities or recesses.

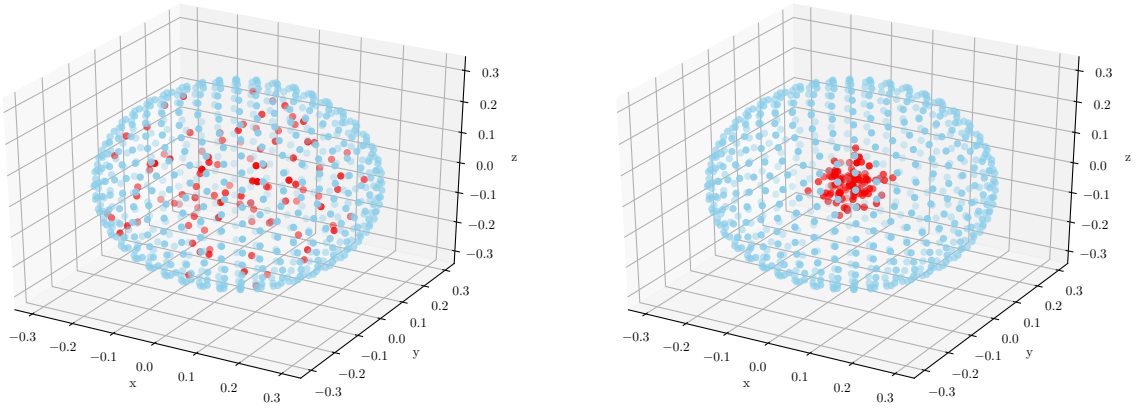

(a) $\alpha = 1$. **(b)** $\alpha = 20$.

FIGURE A.1 - *Influence of α on sources (red dots) distribution in a spherical mesh defined by control points (blue dots).*

Inclusion test for the sorting phase

Given a potential source position $\boldsymbol{r}$ belonging to the convex hull, the process to figure out wether $\boldsymbol{r}$ is inside the mesh or not is conducted in three steps:

1. *Dimension reduction* : $\boldsymbol{r}$ and the entire mesh are projected on an arbitrary plane $\mathscr{P}$ ($z = 0$ on the simple example in Fig-A.2). The $\boldsymbol{x}_{|\mathscr{X}}$ notation indicates the projection onto of $\boldsymbol{x}$ onto the plane $\mathscr{X}$.

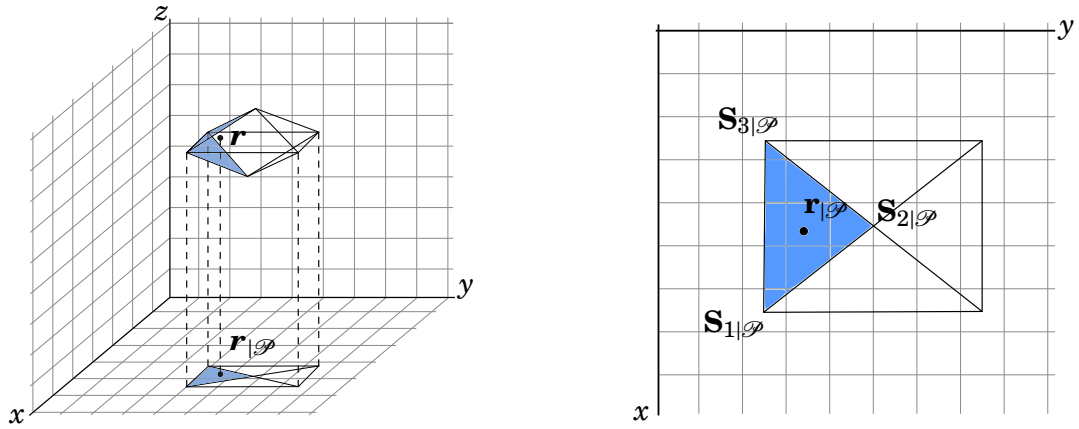

FIGURE A.2 - *Projection step. Working on a 2 dimensional projection eases the search of elements aligned with $\boldsymbol{r}$ along the normal to $\mathscr{P}$ (in blue)*

2. *Search for aligned elements*: working on the projected geometry, all the elements containing $\boldsymbol{r}_{|\mathscr{P}}$ are set aside. For that purpose, a loop on every triangular element $(\boldsymbol{S}_1, \boldsymbol{S}_2, \boldsymbol{S}_3)$ solves the 2×2 system

$$\text{Find} \quad s,t \in \mathbb{R}^+ \quad \text{such as} \quad \boldsymbol{r}_{|\mathscr{P}} = \boldsymbol{S}_{1|\mathscr{P}} + s\left(\boldsymbol{S}_{2|\mathscr{P}} - \boldsymbol{S}_{1|\mathscr{P}}\right) + t\left(\boldsymbol{S}_{3|\mathscr{P}} - \boldsymbol{S}_{1|\mathscr{P}}\right). \tag{A.3}$$

As illustrated on Fig-A.3, s and t are to be understood as the "*coordinates*" of $\boldsymbol{r}_{|\mathscr{P}}$ in the triangular element, in such a way that $s+t \leq 1$ indicates that the projected source is inside the triangle.

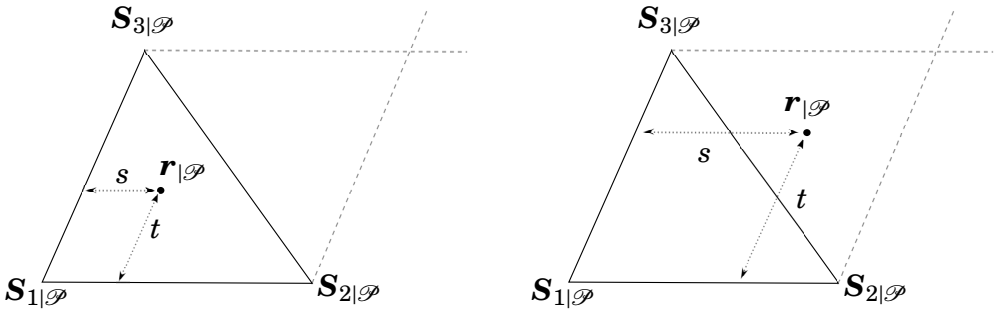

(a) $s+t \leq 1$ **(b)** $s+t \geq 1$

FIGURE A.3 - *Belonging test applied for every elements.*

3. *Intersection counter*: back to the 3D geometry, a *line crossing* method (Chen and Townsend, 1987) is finally applied. For every element aligned with $\boldsymbol{r}$ along the normal to the projection plan $\boldsymbol{n}_{\mathscr{P}}$, a ray starting from the source is casted in the direction of $\boldsymbol{n}_{\mathscr{P}}$. If

$$\frac{\boldsymbol{n}\cdot(\boldsymbol{S}_1 - \boldsymbol{r})}{\boldsymbol{n}\cdot\boldsymbol{n}_{\mathscr{P}}} \geq 0, \tag{A.4}$$

then there is an intersection between the ray and an element of the surface mesh.

The parity of this tally enables to conclude with the inclusion test: an odd number of intersections between the ray and the mesh means that the source is inside, while an even results shows that $\boldsymbol{r}$ is outside and must be removed before the ESM computation.

The whole source generation algorithm was validated on various surface meshes, yielding good results. The torus example on Fig-A.5 was relevant since its barycentre itself is actually outside the mesh and it was obvious that a lot of sources would be outside before the inclusion test.

The test on the industrial case in Fig-A.6 pointed out that a parallelization of the routine will be necessary before its inclusion in MicrodB softwares. The com-

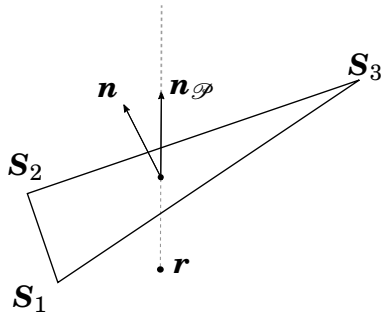

FIGURE A.4 - *Intersection between the ray and an element of the mesh*

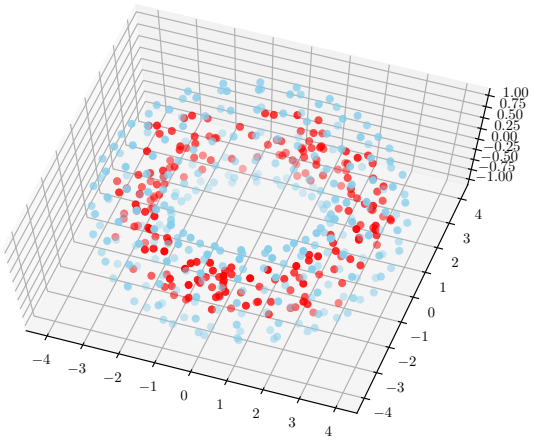

FIGURE A.5 - *Equivalent sources inside a torus, using* $\alpha = 1$.

plexity indeed reaches $O(NN_s)$ for N_s equivalent sources in a mesh of N control points.

Regarding the optimal value for α, connecting this parameter with the retreat distance is a delicate analytical problem. In first estimate, $\alpha = 1$ as a default value empirically proved to be acceptable over the examples presented in this report.

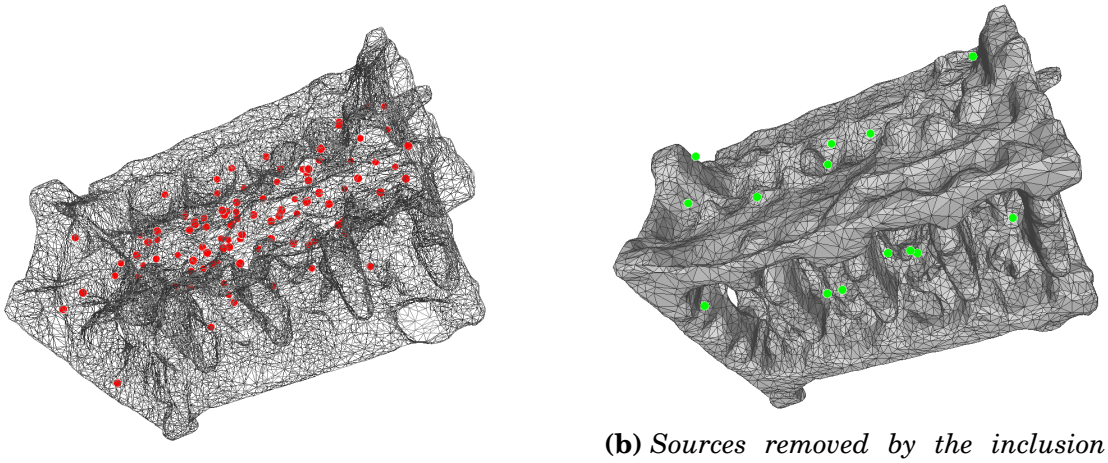

(a) *Valid sources*

(b) *Sources removed by the inclusion routine*

FIGURE A.6 - *Sources generation inside the carter of electric car engine ($N = 25715$ control points, $\alpha = 0.5$). Displayed in* MESHLAB.

References

Adam, J.-L., Menoret, A., and Ricot, D. (**2007**). "Direct aeroacoustic source identification based on lattice boltzmann simulation and beamforming technique," in *15th AIAA/CEAS Aeroacoustics Conference (30th AIAA Aeroacoustics Conference)*, doi: 10.2514/6.2009-3182.

Allen, C. S., Blake, W. K., Dougherty, R. P., Lynch, D., Soderman, P. T., and Underbrink, J. R. (**2002**). *Aeroacoustic Measurements*, first ed. (Springer Berlin, Heidelberg).

Alouges, F., Aussal, M., and Parolin, E. (**2017**). "Fast boundary element method for acoustics with the sparse cardinal sine decomposition," European Journal of Computational Mechanics **26**(4), 377–393, doi: 10.1080/17797179.2017.1306832.

Amiet, R. K. (**1978**). "Refraction of sound by a shear layer," Journal of Sound and Vibration **58**(4), 467–482, doi: 10.1016/0022-460X(78)90353-X.

Antoni, J. (**2012**). "A Bayesian approach to sound source reconstruction: Optimal basis, regularization, and focusing," Journal of the Acoustical Society of America **131**, 2873–2890, doi: 10.1121/1.3685484.

Antoni, J., Le Magueresse, T., Leclère, Q., and Simard, P. (**2019**). "Sparse acoustical holography from iterated Bayesian focusing," Journal of Sound and Vibration **446**, doi: 10.1016/j.jsv.2019.01.001.

Bader, R. (**2010**). "Reconstruction of radiating sound fields using minimum energy method," Journal of the Acoustical Society of America **127**, 300–8, doi: 10.1121/1.3271416.

Bai, M. R. (**1992**). "Application of BEM (boundary element method)-based acoustic holography to radiation analysis of sound sources with arbitrarily shaped geometries," Journal of the Acoustical Society of America **92**(1), 533–549, doi: 10.1121/1.404263.

Bai, M. R., Chen, C.-C., and Lin, J.-H. (**2011**). "On optimal retreat distance for the equivalent source method-based nearfield acoustical holography," Journal of the Acoustical Society of America **129**(3), 1407–1416, doi: 10.1121/1.3533734.

Battista, G. (**2019**). "Inverse methods for three-dimensional volumetric acoustic mapping," Ph.D. thesis, Universita Politecnica delle Marche.

Battista, G., Chiariotti, P., Martarelli, M., Castellini, P., Colangeli, C., and Janssens, K. (**2021**). "3D acoustic mapping in automotive wind tunnel: Algorithm and problem analysis on simulated data," Applied Sciences **11**(7), doi: 10.3390/app11073241.

Blumrich, R., and Helfer, M. (**2017**). "Application of wind tunnels for automotive aeroacoustic development," Science an Technology Organization .

Bonnet, M. (**1999**). *Boundary Integral Equations Methods in Solids and Fluids* (John Wiley and sons).

Bouchet, L., Loyau, T., Hamzaoui, N., and Boisson, C. (**2000**). "Calculation of acoustic radiation using equivalent-sphere methods," Journal of the Acoustical Society of America **107**(5), 2387–2397, doi: 10.1121/1.428625.

Bousabaa, S. (**2018**). "Acoustic Green's function estimation using numerical simulations and application to extern aeroacoustic beamforming," Ph.D. thesis, Sorbonne Université.

Brentner, K. S., and Farassat, F. (**2003**). "Modeling aerodynamically generated sound of helicopter rotors," Progress in Aerospace Sciences **39**(2), 83–120, doi: 10.1016/S0376-0421(02)00068-4.

Burton, A. J., and Miller, G. F. (**1971**). "The application of integral equation methods to the numerical solution of some exterior boundary-value problems," Proceedings of the Royal Society of London. Series A, Mathematical and Physical Sciences **323**(1553), 201–210, doi: 10.1098/rspa.1971.0097.

Butler, J. L. (**1970**). "Solution of Acoustical-Radiation problems by boundary collocation," Journal of the Acoustical Society of America **48**(1B), 325–336, doi: 10.1121/1.1912132.

Casalino, D. (**2002**). "Analytical and numerical methods in vortex-body aeroacoustics," Ph.D. thesis, École Centrale de Lyon.

Chandler-Wilde, S., and Langdon, S. (**2007**). "Boundary element methods for acoustics" .

Chardon, G. (**2022**). "Theoretical analysis of beamforming steering vector formulations for acoustic source localization," Journal of Sound and Vibration **517**, doi: 10.1016/j.jsv.2021.116544.

Chardon, G., and Boureau, U. (**2021**). "Gridless three-dimensional compressive beamforming with the Sliding Frank-Wolfe algorithm," Journal of the Acoustical Society of America **150**(4), 3139–3148, doi: 10.1121/10.0006790.

Chen, I.-L. (**2006**). "Using the method of fundamental solutions in conjunction with the degenerate kernel in cylindrical acoustic problems," Journal of the Chinese Institute of Engineers **29**, 445–457, doi: 10.1080/02533839.2006.9671140.

Chen, M., and Townsend, T. (**1987**). "Efficient and Consistent Algorithms for determining the Containment of points in Polygons and Polyhedra," Computer Graphics Forum doi: 10.2312/egtp.19871032.

Chiariotti, P., Martarelli, M., and Castellini, P. (**2019**). "Acoustic beamforming for noise source localization – Reviews, methodology and applications," Mechanical Systems and Signal Processing **120**, 422–448, doi: 10.1016/j.ymssp.2018.09.019.

Coifman, R., Rokhlin, V., and Wandzura, S. (**1993**). "The fast multipole method for the wave equation: A pedestrian prescription," IEEE Antennas and Propagation Magazine **35**(3), 7–12, doi: 10.1109/74.250128.

Curle, N. (**1955**). "The influence of solid boundaries upon aerodynamic sound," Proceedings of the Royal Society of London. Series A, Mathematical and Physical Sciences **231**(1187), 505–514.

Dinsenmeyer, A., Leclère, Q., and Pereira, A. (**2020**). "A probabilistic approach for cross-spectral matrix denoising: Benchmarking with some recent methods," Journal of the Acoustical Society of America **147**, 3108–3123, doi: 10.1121/10.0001098.

Dougherty, R. P. (**2002**). "Beamforming In Acoustic Testing," in *Aeroacoustic Measurements*, edited by C. S. Allen, W. K. Blake, R. P. Dougherty, D. Lynch, P. T. Soderman, J. R. Underbrink, and T. J. Mueller, Experimental Fluid Mechanics (Springer, Berlin, Heidelberg), pp. 62–97, doi: 10.1007/978-3-662-05058-3_2.

Duda, R. O., and Martens, W. L. (**1998**). "Range dependence of the response of a spherical head model," Journal of the Acoustical Society of America **104**, 3048–3058, doi: 10.1121/1.423886.

Dumbacher, S., and Brown, D. (**1997**). "Practical considerations of the inverse frequency response function (IFRF) technique as applied to noise path analysis and acoustical imaging," in *15th International Modal Analysis Conference*, pp. 1677–1685.

Dunn, M., and Tinetti, A. (**2004**). "Aeroacoustic scattering via the equivalent source method," in *10^{th} AIAA/CEAS Aeroacoustics Conference*, doi: 10.2514/6.2004-2937.

Dunn, M. H., and Tinetti, A. F. (**2008**). "Application of fast multipole methods to the NASA fast scattering code," in *14th AIAA/CEAS Aeroacoustics Conference (29th AIAA Aeroacoustics Conference)*, doi: 10.2514/6.2008-2875.

Ehrenfried, K., and Koop, L. (**2007**). "Comparison of iterative deconvolution algorithms for the mapping of acoustic sources," AIAA Journal **45**(7), 1584–1595, doi: 10.2514/1.26320.

Ernst, D., Spehr, C., and Berkefeld, T. (**2016**). "Decorrelation of Acoustic Wave Propagation through the Shear Layer in Open Jet Wind Tunnel," Journal of Sound and Vibration doi: 10.2514/6.2015-2976.

Evans, D., Hartmann, M., and Delfs, J. (**2019**). "Beamforming for point force surface sources in numerical data," Journal of Sound and Vibration **458**, 303–319, doi: 10.1016/j.jsv.2019.05.030.

Ewert, R., and Schröder, W. (**2003**). "Acoustic perturbation equations based on flow decomposition via source filtering," Journal of Computational Physics **188**(2), 365–398, doi: 10.1016/S0021-9991(03)00168-2.

Farassat, F. (**1975**). "Theory of noise generation from moving bodies with an application to helicopter rotors," Technical Report.

Fernandez-Grande, E., Xenaki, A., and Gerstoft, P. (**2017**). "A sparse equivalent source method for near-field acoustic holography," Journal of the Acoustical Society of America **141**(1), 532–542, doi: 10.1121/1.4974047.

Ffowcs Williams, J. E., and Hawkings, D. L. (**1969**). "Sound generation by turbulence and surfaces in arbitrary motion," Philosophical Transactions of the Royal Society of London. Series A, Mathematical and Physical Sciences **264**, 321–342.

Gao, J., Wu, H., and Jiang, W. (**2020**). "Dipole-based beamforming method for locating dipole sources with unknown orientations in three-dimensional domains," Journal of the Acoustical Society of America **147**(1), 125–136, doi: 10.1121/10.0000491.

Gilquin, L., Bouley, S., Le Magueresse, T., and Marteau, C. (**2019**). "Sensitivity analysis of two inverse methods: Conventional Beamforming and Bayesian focusing," Journal of Sound and Vibration **455**, doi: 10.1016/j.jsv.2019.05.002.

Golub, G. H., and Van Loan, C. F. (**1996**). *Matrix Computations (3rd Ed.)* (Johns Hopkins University Press, USA).

Haddad, K., and Hald, J. (**2008**). "3D localization of acoustic sources with a spherical array," in *Proceedings of Acoustics - CFA*, Paris, Vol. 123.

Hajczak, A. (**2020**). "Méthodes numériques d'identification des sources de bruit aérodynamique pour les trains d'atterrissage," Ph.D. thesis, Sorbonne Université.

Hald, J. (**2019**). "Denoising of cross-spectral matrices using canonical coherence," Journal of the Acoustical Society of America **146**, 399–408, doi: 10.1121/1.5116010.

Hald, J. (**2020**). "A comparison of compressive equivalent source methods for distributed sources," Journal of the Acoustical Society of America **147**, 2211–2221, doi: 10.1121/10.0001073.

Hansen, C. (**1990**). "The discrete picard condition for discrete ill-posed problems," BIT Numerical Mathematics **30**, 658–672, doi: 10.1007/BF01933214.

Haubrich, R. A. (**1968**). "Array design," Bulletin of the Seismological Society of America **58**(3), 977–991, doi: 10.1785/BSSA0580030977.

Holland, K., and Nelson, P. (**2012**). "An experimental comparison of the focused beamformer and the inverse method for the characterisation of acoustic sources in ideal and non-ideal acoustic environments," Journal of Sound and Vibration **331**(20), 4425–4437, doi: 10.1016/j.jsv.2012.05.005.

Jeong, C.-H., and Ih, J.-G. (**2009**). "Reconstruction of sound source pressures in an enclosure using the phased beam tracing method," Journal of the Acoustical Society of America **126**(1), 158–166, doi: 10.1121/1.3132502.

Jordan, P., Fitzpatrick, J., and Valière, J.-C. (**2002**). "Measurement of an aeroacoustic dipole using a linear microphone array," Journal of the Acoustical Society of America **111**, 1267–73, doi: 10.1121/1.1446052.

Kondapalli, P. S., Shippy, D. J., and Fairweather, G. (**1992**). "Analysis of acoustic scattering in fluids and solids by the method of fundamental solutions," Journal of the Acoustical Society of America **91**(4), 1844–1854, doi: 10.1121/1.403714.

Koopmann, G. H., and Fahnline, J. B. (**1991**). "A numerical solution for the general radiation problem based on the combined methods of superposition and singular-value decomposition," Journal of the Acoustical Society of America **90**, 2808–2819, doi: 10.1121/1.401878.

Koopmann, G. H., Song, L., and Fahnline, J. B. (**1989**). "A method for computing acoustic fields based on the principle of wave superposition," Journal of the Acoustical Society of America **86**, 2433–2438, doi: 10.1121/1.398450.

Lam, B., Elliott, S., Cheer, J., and Gan, W.-S. (**2015**). "Regularisation of the equivalent source method for robust numerical modelling of acoustic scattering," in *InterNoise*, InterNoise.

Le Magueresse, T. (**2016**). "Approche unifiée multidimensionelle du problème d'identification acoustique inverse," Ph.D. thesis, LAUM & LVA.

Le Magueresse, T., Antoni, J., and Minck, O. (**2018**). "Experimental applications of Bayesian Focusing in an industrial context," in *ISMA*.

Le Magueresse, T., Outrequin, A., Thivant, M., Antoni, J., and Jouvray, J.-L. (**2020**). "3D acoustical characterization of an electrical engine by Bayesian focusing," in 8^{th} *Berlin Beamforming Conference*.

Leblanc, A., Ing, R., and Lavie, A. (**2010**). "A wave superposition method based on monopole sources with unique solution for all wave numbers," Acta Acustica united with Acustica **96**, 125–130, doi: 10.3813/AAA.918263.

Leclère, Q., Aujogue, N., Dinsenmeyer, A., Antoni, J., and Julliard, E. (**2020**). "Characterization of engine jet noise in flight conditions using advanced acoustic imaging methods," in *8th Berlin Beamforming Conference*.

Leclère, Q., Laulagnet, B., and Polac, L. (**2005**). "Application of an innovative acoustic imaging technique to assess acoustic power maps of a gasoline engine," in *Forum Acusticum*, Budapest.

Leclère, Q., Pereira, A., Bailly, C., Antoni, J., and Picard, C. (**2017**). "A unified formalism for acoustic imaging based on microphone array measurements," International Journal of Aeroacoustics **16**, 431–456, doi: 10.1177/1475472X17718883.

Lee, S. (**2017**). "Review: The use of Equivalent Source Method in computational acoustics," Journal of Computational Acoustics **25**(01), doi: 10.1142/S0218396X16300012.

Lee, S., Brentner, K., and Morris, P. (**2011**). "Assessment of time-domain equivalent source method for acoustic scattering," AIAA Journal **49**, 1897–1906, doi: 10.2514/1.J050736.

Lehmann, M., Ernst, D., Schneider, M., Spehr, C., and Lummer, M. (**2022**). "Beamforming for measurements under disturbed propagation conditions using numerically calculated Green's functions," Journal of Sound and Vibration **520**, 116638, doi: 10.1016/j.jsv.2021.116638.

Lighthill, M. J. (**1952**). "On sound generated aerodynamically. I. General theory," Proceedings of the Royal Society of London. Series A, Mathematical and Physical Sciences **211**(1107), 564–587.

Lima Pereira, L. T., Merino-Martínez, R., Ragni, D., Gómez-Ariza, D., and Snellen, M. (**2021**). "Combining asynchronous microphone array measurements for enhanced acoustic imaging and volumetric source mapping," Applied Acoustics **182**, 108247, doi: 10.1016/j.apacoust.2021.108247.

Liu, Y., Quayle, A., Dowling, A., and Sijtsma, P. (**2008**). "Beamforming correction for dipole measurement using two-dimensional microphone arrays," Journal of the Acoustical Society of America **124**, 182–91, doi: 10.1121/1.2931950.

Merino-Martínez, R., Sijtsma, P., Snellen, M., Ahlefeldt, T., Antoni, J., Bähr, C., Blacodon, D., Ernst, D., Finez, A., Funke, S., Geyer, T., Haxter, S., Herold, G., Huang, X., Humphreys, M., Leclere, Q., Malgoezar, A., Michel, U., Padois, T., Pereira, A., Picard, C., Sarradj, E., Siller, H., Simons, D., and Spehr, C. (**2019**). "A review of acoustic imaging methods using phased microphone arrays," CEAS Aeronautical Journal **10**, 197–230, doi: 10.1007/s13272-019-00383-4.

Najafi-Yazdi, A., Brès, G., and Mongeau, L. (**2011**). "An acoustic analogy formulation for moving sources in uniformly moving media," Proceedings of The Royal

Society A Mathematical Physical and Engineering Sciences **467**, 144–165, doi: 10.1098/rspa.2010.0172.

Nelson, P., and Elliott, S. (**1992**). vol. 3 *Active Control of Sound* (Elsevier Science).

Nelson, P., and Yoon, S. (**2000**). "Estimation of acoustic sources strength by inverse methods: Part I, conditioning of the inverse problem," Journal of Sound and Vibration **233**(4), 639–664, doi: 10.1006/jsvi.1999.2837.

Nicol, R. (**1999**). "Restitution sonore spatialisée sur une zone étendue: Application à la téléprésence," Ph.D. thesis, Université du Maine.

Nordborg, A., Wedemann, J., and Willenbrink, L. (**2000**). "Optimum array microphone configuration," Inter-Noise.

Norton, M. P., and Karczub, D. G. (**2003**). *Fundamentals of Noise and Vibration Analysis for Engineers*, second ed. (Cambridge University Press, Cambridge).

Ochmann, M. (**1995**). "The source simulation technique for acoustic radiation problems," Acta Acustica **81**(6), 512–527.

Pan, S., Yang, J., Kaiqiang, W., Wang, Z., and Deng (**2020**). "Study on radiated noise of a panel under fluctuating surface pressure due to an Idealized Side Mirror," Applied Sciences **10**, 994, doi: 10.3390/app10030994.

Papamoschou, D., and Mayoral, S. (**2013**). "Modeling of jet noise sources and their diffraction with uniform flow," in *51st AIAA Aerospace Sciences Meeting Including the New Horizons Forum and Aerospace Exposition*, **51**, doi: 10.2514/6.2013-326.

Pavić, G. (**2005**). "An engineering technique for the computation of sound radiation by vibrating bodies using substitute sources," Acta Acustica United With Acustica **91**, 1–16.

Penrose, R. (**1955**). "A generalized inverse for matrices," Mathematical Proceedings of the Cambridge Philosophical Society **51**(3), 406–413, doi: 10.1017/S0305004100030401.

Pereira, A. (**2013**). "Acoustic imaging in enclosed spaces," Ph.D. thesis, INSA Lyon.

Pereira, A., Antoni, J., and Leclère, Q. (**2015**). "Empirical Bayesian regularization of the inverse acoustic problem," Applied Acoustics **97**, 11–29, doi: 10.1016/j.apacoust.2015.03.008.

Pierce, A. D. (**1981**). *Acoustics - An Introduction to Its Physical Principles and Applications*, third ed. (Springer (previously McGraw-Hill)).

Pignier, N., O'Reilly, C., and Boij, S. (**2016**). "Aeroacoustic study of a submerged air inlet using an IDDES/FW-H approach and sound source modelling through direct numerical beamforming," in *22nd AIAA / CEAS Aeroacoustics Conference*, doi: 10.2514/6.2016-2838.

Porteous, R., Prime, Z., Doolan, C., Moreau, D., and Valeau, V. (**2015**). "Three-dimensional beamforming of dipolar aeroacoustic sources," Journal of Sound and Vibration **355**, doi: 10.1016/j.jsv.2015.06.030.

Rafaely, B. (**2015**). *Fundamentals of Spherical Array Processing*, **8** (Springer).

Samarasinghe, P., Abhayapala, T. D., and Kellermann, W. (**2017**). "Acoustic reciprocity: An extension to spherical harmonics domain," Journal of the Acoustical Society of America **142**(4), EL337–EL343, doi: 10.1121/1.5002078.

Sarkissian, A. (**2005**). "Method of superposition applied to patch near-field acoustic holography," Journal of the Acoustical Society of America **118**(2), 671–678, doi: 10.1121/1.1945470.

Sarradj, E. (**2012**). "Three-dimensional acoustic source mapping with different beamforming steering vector formulations," Advances in Acoustics and Vibration **2012**, doi: 10.1155/2012/292695.

Sarradj, E. (**2022**). "Three-dimensional gridless source mapping using a signal subspace approach," in *9th Berlin Beamforming Conference*.

Schenck, H. A. (**1968**). "Improved integral formulation for acoustic radiation problems," Journal of The Aoustical Society of America **44**(1), 41, doi: 10.1121/1.1911085.

Schmitt, A., Lamotte, L., and Deblauwe, F. (**2010**). "Source identification inside cabin using inverse methods," in *3rd Berlin Beamforming Conference*.

Schulze, C., Sarradj, E., and Zeibig, A. (**2004**). "Characteristics of microphone arrays," in *Inter-Noise*, Institute of Noise Control Engineering, Vol. 2004, pp. 2753–2759.

Siemens (**2021**). "Simcenter STAR-CCM+, version 2021.1" .

Sijtsma, P. (**2004**). "Experimental techniques for identification and characterisation of noise sources," in *Advances in Aeronautics & Applications*, VKI Lecture Series, National Aerospace Laboratory NLR.

Sijtsma, P. (**2007**). "CLEAN based on spatial source coherence," International Journal of Aeroacoustics **6**, 357–374, doi: 10.1260/147547207783359459.

Sijtsma, P. (**2008**). "Acoustic array corrections for coherence loss due to the wind tunnel shear layer," in *2nd Berlin Beamforming Conference*, National Aerospace Laboratory.

Skudrzyk, E. (**1971**). *The Foundations of Acoustics: Basic Mathematics and Basic Acoustics* (Springer Vienna).

Suzuki, T. (**2011**). "Generalized inverse beam-forming algorithm resolving Coherent/Incoherent, distributed and multipole sources," Journal of Sound and Vibration **330**, 5835–5851, doi: 10.1016/j.jsv.2011.05.021.

Tikhonov, A. N. (**1963**). “Solution of incorrectly formulated problems and the regularization method,” Soviet Mathematics Doklady **4**, 1035–1038.

Valdivia, N., and Williams, E. (**2007**). “Study of the comparison of the methods of equivalent sources and boundary element methods for near-field acoustic holography,” Journal of the Acoustical Society of America **120**, 3694–705, doi: 10.1121/1.2359284.

Valdivia, N. P. (**2018**). “Advanced equivalent source methodologies for near-field acoustic holography,” Journal of Sound and Vibration **438**, 66–82, doi: 10.1016/j.jsv.2018.08.028.

Veronesi, W. A., and Maynard, J. D. (**1989**). “Digital holographic reconstruction of sources with arbitrarily shaped surfaces,” Journal of the Acoustical Society of America **85**(2), 588–598, doi: 10.1121/1.397583.

Wang, L., Chen, R., You, Y., Wang, Z., and Song, Q. (**2022**). “An efficient frequency-domain prediction method for aeroacoustic radiation and scattering using equivalent sources,” Journal of Sound and Vibration **534**, 117039, doi: 10.1016/j.jsv.2022.117039.

Wang, Y., Gu, Z., Li, W., and Lin, X. (**2010**). “Evaluation of aerodynamic noise generation by a generic side mirror,” **37**, doi: 10.5281/zenodo.1071039.

Welch, P. (**1967**). “The use of fast Fourier transform for the estimation of power spectra: A method based on time averaging over short, modified periodograms,” IEEE Transactions on Audio and Electroacoustics **15**(2), 70–73, doi: 10.1109/TAU.1967.1161901.

Wells, V. L., and Han, A. Y. (**1995**). “Acoustics of a moving source in a moving medium with application to propeller noise,” Journal of Sound and Vibration **184**(4), 651–663, doi: 10.1006/jsvi.1995.0339.

Williams, G. (**1999**). *Fourier Acoustics: Sound Radiation and Nearfield Acoustical Holography* (Elsevier Science).

Wilton, D. T., Mathews, I. C., and Jeans, R. A. (**1993**). “A clarification of nonexistence problems with the superposition method,” Journal of the Acoustical Society of America **94**(3), 1676–1680, doi: 10.1121/1.408140.

Xenaki, A., Fernandez-Grande, E., and Gerstoft, P. (**2016**). “Block-sparse beamforming for spatially extended sources in a Bayesian formulation,” Journal of the Acoustical Society of America **140**, 1828–1838, doi: 10.1121/1.4962325.

Zhou, Y., Valeau, V., Marchal, J., Ollivier, F., and Marchiano, R. (**2020**). “Three-dimensional identification of flow-induced noise sources with a tunnel-shaped array of MEMS microphones,” Journal of Sound and Vibration **482**, 115459, doi: 10.1016/j.jsv.2020.115459.

List of figures

1.1 Acoustic imaging schematic set-up. A set of acoustic sources $\boldsymbol{q}$ supported by a discretized three-dimensional surface Γ is identified from the microphone pressures $\boldsymbol{p}$, featuring the inversion of a propagation model $\boldsymbol{H}$. 6
1.2 MicrodB Sound Camera (117 MEMS microphones). 8
1.3 Paradigm shift between 2D (left) and 3D (right) sources support Γ. The stake arising with surfacic three-dimensional imaging lies in the changes in the transfer model for grid points on Γ that are no longer directly facing the planar array. 10
1.4 Identification of a monopole on a rigid sphere at $ka = 19$ using free field transfer functions and various imaging algorithms. Levels are relative to the source strength and plotted within a 20 dB dynamic range. 17
1.5 Acoustic pressure (real part) of a monopole (a); and a dipole with $\boldsymbol{d} = (1,0,0)$ (b) at $f = 100$ Hz. The red dot indicates the position of the sources. 19
1.6 Considering a rigid sphere of radius a, SRTF analytically provides the pressure at p_i given a monopole of volumic flow q_j while taking into account the scattered path in red instead of the free field one (dashed). 21
1.7 Acoustic pressure (amplitude) of (a) a free-field monopole; (b) a monopole scattered by a rigid sphere of radius $a = 1$ m at $ka = 2.1$. The red dot indicates the position of the sources. 22
1.8 CBF example maps obtained on simulated data at $ka = 16$; (a) Free-field transfer functions; (b) SRTF. The red dot indicates the ground truth position of the source, which was purposely placed on the opposite side from the planar array (black dots). It is clear in that case that an accurate transfer model is required to localize the source. . . 23
1.9 FRF (volumic flow amplitude) on a rear view mirror from an observer on the car window at $f = 4000$ Hz, from Evans *et al.* (2019). . . 24
1.10 FW-H schematic set up. Ω_s accounts for the source area, and Γ denotes the boundary of a rigid object. The pressure at the observer point $\boldsymbol{r}$ can be obtained from the source region only. 26
1.11 Source terms in FW-H analogy exemplified on a car (inspired by Blumrich and Helfer, 2017). 27
1.12 Acoustic pressure (real part) of a thickness noise source at $f = 100$ Hz and $\boldsymbol{M}_0 = (-0.2, 0., 0.)$. The red dot indicates the source position. . 29

2.1 Wave superposition method : The integration of volume sources inside Ω_{eq} is strictly equivalent to the Kirchhoff-Helmholtz integration on Γ and Ω for the reconstruction of $p(\mathbf{r})$ 33

2.2 ESM schematic set-up. Equivalent sources $(\tilde{q}_l)_{l\leq N_s}$ (in grey) are adjusted to counter balance the normal velocity induced by a unitary source q^{inc} at every control points on Γ. 34
2.3 Geometric values chosen for the SRTF validation. The first control point under scrutiny is located on the opposite to the microphone (in red) for the diffraction to be significant, while the second one it more similar to a free field propagation. 39
2.4 Comparison of ESM with analytical SRTF results on the (-0.25,0,0) position. 40
2.5 Comparison of ESM with analytical SRTF results on the (-0.17,0.17,0) position. 41
2.6 Acoustic pressure (amplitude) of (a) the incident field produced by a monopole (red dot); (b) the radiated field emitted by the equivalent sources; (c) the complete field, at $ka = 2.1$. 42
2.7 ESM sensitivity to the retreat distance at $ka = 2.2$ (top) and $ka = 11.2$ (bottom). In black is plotted the L^2 error on the SRTF reconstruction, in red the conditioning number of $\boldsymbol{T}$, and dashed lines were obtained with random equivalent source positions while plain lines with a scaled replica of the sphere. 44
2.8 Mean value (dark blue dot) ± the standard deviation (sky blue arrows) of the ε^v indicator. 44
2.9 Reciprocity principle applied to dipolar FRFs. The computation of a half dipole on the mesh radiating toward a microphone can be traded against the one of a dipole with opposite direction located on the array toward the surface. 46
2.10 Scattered dipole PSF at $ka = 22$, the red dot indicates the ground truth position of the source and the black ones refers to the microphone array; (a) Unfiltered; (b) Filtered with Evans *et al.* (2019) process depicted in Eq.(2.3.1). 47
2.11 Picard plot of the $-\boldsymbol{v}_n = \boldsymbol{P}\boldsymbol{\Sigma}\boldsymbol{Q}^{\mathsf{H}}\tilde{\boldsymbol{q}}$ inverse problem at $ka = 2.1$. The set-up is the same as the one of Fig-2.3. On this example, singular values starts to decrease faster than $|\boldsymbol{P}_l \cdot \boldsymbol{v}_n|$, $\boldsymbol{P}$ for $l > 120$. 48
2.12 Acoustic pressure (amplitude) of (a) the incident field produced by a monopole (red dot); (b) the radiated field emitted by the equivalent sources; (c) the complete field, over a rigid ground at $y = -5.5$ m at $ka = 1.3$. 49
2.13 Refracted acoustic path in the ESM set up. The acoustic transfer is now composed of the paths covered outside and within the flow r_{ij}^{ff} and r_{ij}^{flow}, the impact point $\mathscr{I}_{ij}$ on the shear layer being obtained thanks to a iterative integrating scheme (Allen *et al.*, 2002). 50

3.1 A set of equivalent monopolar sources with complex amplitudes $\tilde{\boldsymbol{q}}$ (blue dots) is sought after to match both the impedance condition $\boldsymbol{z}$ on the skin of the body and the pressure $\boldsymbol{p}$ measured by a microphone array at a given frequency. 56

3.2 Geometrical set-up for validation. The yellow surface is the control point support Γ, the transparent grey (plane and concentric outer sphere) is Γ_{obs} and the cloud of points around it is the microphone array. 62
3.3 Sensitivity of the GESM propagation matrix $\boldsymbol{GB}$ to the retreat distance ξ_d for the spherical geometry. 63
3.4 Directivity pattern of 10 uncorrelated monopoles on a rigid sphere at $ka = 1$ (top) and $ka = 13$ (bottom), computed through various imaging algorithms. At low frequency, both Galerkin ESM and iBF are matching with the reference (all 4 plots are overlapped). 66
3.5 Directivity pattern of 10 correlated monopoles on a rigid sphere at $ka = 1$ (top) and $ka = 13$ (bottom), computed through various imaging algorithms. At low frequency, both Galerkin ESM and iBF are matching with the reference (all 4 plots are overlapped). 68
3.6 Acoustic pressure (amplitude) on Γ_{obs} radiated by 5 uncorrelated monopoles at $k = 13$ (with a 20 dB dynamic range). (a) Analytical sound field. (b) Sound field propagated by sources identified with iBF featuring free-field FRF. (c) Sound field propagated by sources identified with iBF featuring analytical FRF. (d) Sound field propagated by sources identified with Galerkin ESM. 69
3.7 Acoustic pressure (amplitude) on Γ_{obs} radiated by 5 randomly correlated monopoles at $k = 13$ (with a 20 dB dynamic range). (a) Analytical sound field. (b) Sound field propagated by sources identified with iBF featuring free-field FRF. (c) Sound field propagated by sources identified with iBF featuring analytical FRF. (d) Sound field propagated by sources identified with Galerkin ESM. 70
3.8 Pressure amplitudes on Γ_{obs} radiated by the i^{th} column of $\boldsymbol{Q}_2\boldsymbol{\Lambda}$ ($\boldsymbol{\Lambda}$ being the identity matrix); (a) $i = 1$; (b) $i = 10$; (c) $i = 100$; (d) $i = 250$ and $ka = 8.24$. Plots are displayed within a 30 dB dynamic range, and the red dot indicates the maximum level location. 72
3.9 Pressure amplitudes on Γ_{obs} radiated by the i^{th} column of $\boldsymbol{Q}_2\boldsymbol{\Lambda}$ ($\boldsymbol{\Lambda}$ being defined by Eq.(3.3.3)); (a) $i = 1$; (b) $i = 10$; (c) $i = 100$; (d) $i = 250$ and $ka = 8.24$. Plots are displayed within a 30 dB dynamic range, and the red dot indicates the maximum level location. 73
3.10 Reconstruction indicators for 10 correlated monopoles on a rigid sphere at $ka = 1$. In black is plotted the L^2 relative error, in blue is displayed radiated power from Eq. (3.3.4). Dashed lines features $\boldsymbol{\Lambda} = \boldsymbol{I}$ while solid lines were obtained with $\boldsymbol{\Lambda}$ sampled from the radiation efficiency operator. 74

4.1 Wind tunnel experimental set-up; (a) Disposition of the three planar arrays around the car, in red is exposed the source position; (b) Omnidirectional source at the top edge of the rear-view mirror. 78
4.2 CSM amplitudes of the combined three planar arrays at $f = 1000$ Hz, ordered as top, left and right with increasing indices; (a) No wind measurements; (b) $M_0 = 0.11$ measurements. 78

4.3 Comparative plot of δ_c and the condition number $\kappa(\boldsymbol{T})$ for various $\eta = \frac{N_s}{N}$ ratios at various frequencies. 80
4.4 FRF amplitude between the 85$^{\text{th}}$ microphone of the left array (red dot) and the car mesh at $f = 1500$ Hz and $\eta = 0.25$; (a) Free field; (b) ESM. The horizontal interferences are due to the ground reflections. 81
4.5 CBF maps from no wind measurements at $f = 3000$ Hz; (a,c,e) Free-field FRF; (b,d,f) ESM monopolar FRF. 82
4.6 CBF maps from no wind measurements at $f = 1500$ Hz; (a,c,e) Free-field FRF; (b,d,f) ESM monopolar FRF. 83
4.7 CBF maps from no wind measurements at $f = 500$ Hz; (a,c) Free-field FRF; (b,d) ESM monopolar FRF. 84
4.8 CBF maps from $M_0 = 0.11$ measurements at $f = 3000$ Hz; (a,c) Free-field FRF; (b,d) ESM monopolar FRF. 85
4.9 CBF maps from $M_0 = 0.11$ measurements at $f = 1500$ Hz; (a,c) Free-field FRF; (b,d) ESM monopolar FRF. 85
4.10 CBF maps from $M_0 = 0.11$ measurements at $f = 500$ Hz; (a,c) Free-field FRF; (b,d) ESM monopolar FRF. 86
4.11 Idealized Side Mirror geometry; (a) Triangular mesh of the modified ISM with top and side flaws; (b) Simulated microphone positions for the CFD computation. The wind direction is set along the positive x axis. 87
4.12 Point Spread Function of the ISM array geometry (within a 12 dB dynamic range) on a plane for convected FRFs; (a) $f = 1000$ Hz; (b) $f = 1500$ Hz; (c) $f = 2000$ Hz; (d) $f = 300$ Hz. 88
4.13 CFD issued spectra on the array for the ISM at $M_0 = 0.11$; (a) average autospectra on the 400 microphones; (b) CSM at $kL = 10$ Hz. . . . 89
4.14 Element-wise surface pressure PSD on the ISM at $M_0 = 0.11$; (a) $kL = 14$; (b) $kL = 21$; (c) $kL = 28$; (d) $kL = 42$. 16 dB dynamic range. . 90
4.15 FRF amplitude between the 357$^{\text{th}}$ microphone (red dot) and the ISM mesh at $kL = 10$; (a) Monopolar free field; (b) Monopolar ESM. 90
4.16 (a) Dipolar ESM FRF amplitude (pressure at the microphones considering unitary sources on the nodes) between a front (blue line) and rear flaw node (green line) and the 400 microphones at $kL = 42$; (b) Location of the nodes on the ISM mesh. 91
4.17 Coherence beamforming maps at $kL = 21$, within a 12 dB dynamic range. (a) Free-field monopolar FRF; (b) free-field dipolar FRF; (c) ESM FRF; (d) dipolar ESM FRF. 92
4.18 Coherence beamforming maps at $kL = 28$, within a 12 dB dynamic range. (a) Free-field monopolar FRF; (b) free-field dipolar FRF; (c) ESM FRF; (d) dipolar ESM FRF. 93
4.19 Coherence beamforming maps at $kL = 42$, within a 12 dB dynamic range. (a) Free-field monopolar FRF; (b) free-field dipolar FRF; (c) ESM FRF; (d) dipolar ESM FRF. 94

4.20 Iterative Bayesian Focusing maps at $kL = 28$, restrained to the top part of the ISM with a 20 dB dynamic range. (a) Free-field monopolar FRF; (b) free-field dipolar FRF; (c) ESM FRF; (d) dipolar ESM FRF. 95
4.21 Iterative Bayesian Focusing maps at $kL = 42$, restrained to the top part of the ISM with a 20 dB dynamic range. (a) Free-field monopolar FRF; (b) free-field dipolar FRF; (c) ESM FRF; (d) dipolar ESM FRF. 96
4.22 Experimental set-up, from Le Magueresse *et al.* (2018). (a) Actual disposition of the array facing the source panel; (b) Disposition of the flush mounted sources. 97
4.23 Numerical set-up for Ecobex test rig. The yellow surface is the control point support Γ, the transparent grey is Γ_{obs} and the 36 black dots represent the microphone array placed at 12 cm from the mock-up. 98
4.24 CBF on the Ecobex flush-mounted sources at $kL = 11$, within an 8 dB dynamic range; (a,b) Free-field FRFs; (c,d) ESM FRFs. 99
4.25 CBF on the Ecobex flush-mounted sources at $kL = 42$, within a 12 dB dynamic range; (a,b) Free-field FRFs; (c,d) ESM FRFs. 100
4.26 iBF on the Ecobex flush-mounted sources at $kL = 11$, within a 16 dB dynamic range; (a) Free-field FRFs; (b) ESM FRFs. 101
4.27 Acoustic pressure (amplitude) repropagated on Γ_{obs} (relative levels with a 20 dB dynamic range). Sound field propagated by sources identified with CBF featuring free field FRF; (a) $kL = 9$; (b) $kL = 21$; (c) $kL = 31$. 102
4.28 Acoustic pressure (amplitude) repropagated on Γ_{obs} (relative levels with a 20 dB dynamic range). Sound field propagated by sources identified with iBF featuring free field FRF; (a) $kL = 9$; (b) $kL = 21$; (c) $kL = 31$. 102
4.29 Acoustic pressure (amplitude) repropagated on Γ_{obs} (relative levels with a 20 dB dynamic range). Sound field propagated by sources identified with Galerkin ESM; (a) $kL = 9$; (b) $kL = 21$; (c) $kL = 31$. . . 103
4.30 Repropagated levels at a reference microphone not included in the microphone array, within the $kL = 2.8$ to 48.6 frequency range. 103
A.1 Influence of α on sources (red dots) distribution in a spherical mesh defined by control points (blue dots). 113
A.2 Projection step. Working on a 2 dimensional projection eases the search of elements aligned with $\boldsymbol{r}$ along the normal to $\mathscr{P}$ (in blue) . . 113
A.3 Belonging test applied for every elements. 114
A.4 Intersection between the ray and an element of the mesh 115
A.5 Equivalent sources inside a torus, using $\alpha = 1$. 115
A.6 Sources generation inside the carter of electric car engine ($N = 25715$ control points, $\alpha = 0.5$). Displayed in MESHLAB. 116

FOLIO ADMINISTRATIF

THÈSE DE L'UNIVERSITÉ DE LYON OPÉRÉE AU SEIN DE L'INSA LYON

NOM : Chambon

DATE de SOUTENANCE : 22 mars 2023

Prénom : Joannès

TITRE : Equivalent source methods for three-dimensional acoustic imaging in complex environments

NATURE : Doctorat

Numéro d'ordre : 2023ISAL0019

Ecole doctorale : Mécanique, Énergétique, Génie civil et Acoustique

Spécialité : Acoustique

RÉSUMÉ :
Un ensemble de problématiques nouvelles en imagerie acoustique sont à considérer pour l'identification de sources en trois dimensions par antennerie. L'une d'entre elle concerne le modèle retenu pour retranscrire la propagation acoustique dans l'environnement de mesure. Ce dernier doit potentiellement être en mesure de prendre en compte des phénomènes de premier ordre de diffraction, de convection ou de directivité liée à la nature physique de sources. En pratique, le choix du modèle de propagation se résume à la construction d'une matrice de transfert entre une grille de sources potentielles et une antenne de microphone qu'il convient d'inverser pour revenir aux sources prépondérantes. Dans cette thèse, la méthode des sources équivalentes est testée en tant qu'outil simple et modulable pour la simulation de fonctions de transfert permettant une description plus précise de la scène acoustique. Des méthodes détaillées de paramétrage des sources équivalentes sont proposées et évaluées sur divers cas d'étude obtenus analytiquement, par mesure en soufflerie ou simulation dynamique des fluides. Pour finir, une approche plus prospective est mise au point dans l'objectif d'inclure les sources équivalentes dans le processus d'antennerie de manière plus cohérente que lors du calcul direct de matrices de transfert. Les sources sont ajustées en fonction des pressions microphoniques et d'une condition aux limites, puis repropagées pour représenter l'ensemble du champ rayonné. L'intérêt de cet algorithme est évalué comparativement à des techniques d'imagerie classique sur des mesures de sources corrélées montées sur une maquette de moteur.

MOTS-CLÉS : Imagerie acoustique, sources équivalentes, antennes de microphone, soufflerie acoustique, problème inverse.

Laboratoire (s) de recherche : Laboratoire Vibrations Acoustique (LVA)

Directeur de thèse : Jérôme Antoni

Président de jury : Vincent Valeau

Composition du jury : Antoni, Jérôme (directeur), Bouley, Simon (encadrant), Chiariotti, Paolo (examinateur), Snellen Mirjam (rapporteure), Thomas, Jean-Hugh (rapporteur) & Valeau, Vincent (examinateur).